GaN Schottky Diodes for THz Generation

THESE

présentée à l'Université de Lille, faculté des Sciences et Technologies
Institut d'Electronique, de Microelectronique et de Nanotechnologies (IEMN)
UMR CNRS 8520

par

Giuseppe Di Gioia

pour obtenir le titre de

Docteur de l'Université

Spécialité: Electronique, microélectronique, nanoélectronique et micro-ondes
Ecole Doctorale Sciences de l'Ingénierie et des Systèmes (ENGSYS-632)

Soutenue le 13 decembre 2021 devant le jury composé de:

Président	Guillaume DUCOURNAU	IEMN, Professeur titulaire
Rapporteur	Rachid DRIAD	Fraunhofer IAF, Ingénieur de recherche
Rapporteur	Frédéric ANIEL	Université Paris Sud, Professeur titulaire
Examinatrice	Tiphaine CERBA	III-V Lab, Ingénieur de recherche
Directeur de thèse	Mohammed ZAKNOUNE	IEMN, Directeur de recherche
Co-encadrant	Yannick ROELENS	IEMN, Maître de conférences

Abstract

Terahertz science has many areas of applications, such as astronomy, security, biomedical analysis, and wireless telecommunication. However, the application of THz technology has been hindered by the lack of suitable, reliable, compact, and cost-effective terahertz sources. Although there are numerous ways to generate power at THz frequencies, many of these sources suffer from several drawbacks and limitations, such as limited output power, the need for cryogenic temperatures to work, excessive size, complexity, and prohibitive cost. Among the current THz sources, one type of solid-state technology stands out: frequency multiplier. The current state of the art of frequency multiplier technology is represented by GaAs Schottky diode frequency multipliers. This is a well-known technology, which has been employed with success, but as the requirements for the output frequency become more and more high, it has reached a bottleneck, represented by the intrinsic physical limitations of GaAs in terms of breakdown voltage and thermal conductivity, which affect the power-handling capabilities of the frequency multiplier. GaN, thanks to its higher breakdown field and higher thermal conductivity, can yield, in theory, higher power handling capabilities for frequency multipliers, compared to GaAs. These enhanced power handling capabilities can lead to simplified designs of frequency multipliers, compared to the state of the art of GaAs frequency multipliers. In theory, eight GaAs diodes are required for a 200 GHz doubler with input power of 150 mW, while one GaN diode with similar anode area is capable of handling this input power.

In this thesis, quasi-vertical GaN Schottky diodes are fabricated and characterized, in order to investigate their parameters and performances for frequency multiplication applications. The fabrication process is carried out on three different types of GaN epitaxy: GaN on sapphire, GaN on Si, and GaN on SiC. The diodes are fabricated with air-bridge structure to reduce the parasitic components at high frequency.

Résumé

Titre: ***"Diode Schottky GaN pour la génération THz"***

La science térahertz a de nombreux domaines d'applications, tels que l'astronomie, la sécurité, l'analyse biomédicale et les télécommunications sans fil. Cependant, l'application de la technologie THz a été entravée par le manque de sources térahertz adaptées, fiables, compactes et rentables. Bien qu'il existe de nombreuses façons de générer un signal aux fréquences THz , bon nombre de ces sources souffrent de plusieurs inconvénients et limitations, tels qu'une puissance de sortie limitée, le besoin de températures cryogéniques pour fonctionner, une taille excessive, une complexité et un coût prohibitif. Parmi les sources THz actuelles, un type de technologie à semi-conducteurs se distingue : le multiplicateur de fréquence. L'état de l'art actuel de la technologie des multiplicateurs de fréquence est détenu par les multiplicateurs de fréquence à diodes GaAs Schottky. Il s'agit d'une technologie bien connue, qui a été utilisée avec succès, mais comme les exigences de fréquence de sortie deviennent de plus en plus élevées, elle est face, à présent, à un goulot d'étranglement dû aux limitations physiques intrinsèques du GaAs en termes de tension de claquage et de conductivité thermique, qui affectent la puissance de sortie du multiplicateur de fréquence. Le GaN, grâce à son champ de claquage plus élevé et à sa conductivité thermique plus élevée, peut en théorie offrir des capacités de tenu à la puissance de pompe plus élevées pour les multiplicateurs de fréquence par rapport au GaAs. Ces capacités peuvent conduire à des conceptions simplifiées de multiplicateurs de fréquence, par rapport à l'état de l'art des multiplicateurs de fréquence GaAs. En théorie, huit diodes GaAs sont nécessaires pour un doubleur de 200 GHz avec une puissance d'entrée de 150 mW, tandis qu'une diode GaN avec une surface d'anode similaire est capable de gérer cette puissance de pompe en entrée.

Dans cette thèse, des diodes GaN Schottky quasi-verticales sont fabriquées et caractérisées, afin d'étudier leurs paramètres et performances pour des applications de multiplication de fréquence. Le procédé de fabrication est réalisé sur trois types différents d'épitaxie GaN : GaN sur saphir, GaN sur Si et GaN sur SiC. Les diodes sont fabriquées avec une structure en pont d'air pour réduire les composants parasites à haute fréquence.

Acknowledgments

This work experience at IEMN would not have been possible without the unyielding and unconditional support from my family throughout my life. This work is dedicated to them and to the memory of my grandmothers.

I would like to thank my supervisor, Dr. Mohammed Zaknoune. His passion for research, his incredibly vast knowledge, and his profound expertise in semiconductor devices fabrication have been an example throughout these three years of PhD studies.

My thanks go to Dr. Yannick Roelens, for the meaningful help with the characterization of the devices. The critical discussions on the results obtained have been fundamental to give the right value to the content of this thesis.

I would like to extend my thanks to Dr. Rachid Driad of Fraunhofer-IAF and Dr. Frédéric Aniel of Université Paris Sud for having accepted to evaluate this work and to provide a report of the manuscript. I would like to also thank Dr. Tiphaine Cerba of III-V Lab and Dr. Guillaume Ducournau of IEMN for having accepted to evaluate this work.

It would have been impossible to carry out the fabrication work in the clean room without the help and guidance of the entire CMNF group. Especially François, Saliha and Yves for their help with e-beam lithography, Christophe with his vast expertise of the SEM, Marc and Annie for their help in metallization, Dmitri for his help in dry etching, and many others.
I am grateful for the opportunity to work with Vanessa, Sylvie, and Etienne for the characterization of the devices. With their help and insight, I was able to learn and efficiently employ the skills that they kindly shared with me in device characterizations. My thanks go to Dr. Xavier Wallart for his help in providing XPS spectra for the samples. I would like to thank Dr. Henry Happy, who was always ready to help with any matter concerning the doctoral school.

All the people at IEMN are responsible for having created a wonderful and international environment that made working here ever more pleasant.

I would be remiss if I failed to mention the important support of my close friends back in Italy, and the friends found here in Lille in the last three years.

Finally, the biggest thanks go to the person that changed my life the most in the last three years, my partner, Dr. Sara Mosleh. Her love, patience and kindness made my life incredibly happier than I thought was possible. This work would not have been possible without her support.

General Introduction

In the last few decades, the terahertz (THz) region of the electromagnetic spectrum has become the focus of active research in a number of multidisciplinary fields. The interest in THz science dates back almost a century. One of the main driving fields of this technology is astronomy. In fact, nowhere else in the electromagnetic spectrum, scientist can obtain so much information about chemical species of lightweight gases and molecules present in the atmosphere, in proximity of interstellar dust and star formation regions. As THz detectors improved over time, the number of applications arose as well. Research in THz technology applied to security screening and biomedical analysis and sensing witnessed increased interest in recent times, owing this to the non-ionizing character of THz waves and their ability to uniquely identify specific molecules. Another field of application emerged as society evolved. An ever-increasing interconnected society is characterized by a need for higher data rate and larger bandwidth and, in order to satisfy these demands, THz waves have been proposed as carrier frequencies. Although they pose several technological challenges, the advantages are enough to justify a massive amount of resources being poured into this research direction. It is in this context that THz Achille's heel was made evident. Owing to the niche application that THz science had in astronomy for many decades, THz detectors developed much faster than THz sources. It was in this way that the so-called "THz gap" became evident.
Although there are numerous ways to generate THz radiation, such as quantum cascade lasers (QCLs), resonant tunneling diodes (RTDs), or photonic sources such as uni-travelling-carrier photodiodes (UTC-PDs) they all have their own limitations. They are limited in output power or limited by their size, some of them require cryogenic cooling, and others are characterized by a high level of complexity or by a prohibitive cost. Nonetheless, among electronic solid-state sources for THz , frequency multipliers have gained an important place. Improvements in technological fabrication and design made it possible for this type of technology to overcome the 1 THz milestone and, subsequently, to gain several advantages compared to other types of THz sources. The state of the art of this technology is represented by frequency multipliers relying on the non-linearity of Schottky diodes; more specifically, the current technological standard consists in gallium arsenide ($GaAs$) Schottky diode frequency multipliers.
GaAs Schottky diode frequency multipliers have been employed with success in the last few decades. However, as the requirements for output power and efficiency continue to increase, the limitations of this technology and, in particular, the limitations of GaAs, became evident, limitations that go from GaAs breakdown voltage, limited scalability of devices because of inferior power handling capabilities, to design limitations, since the multiplier circuit has assumed more and more complex

architectures in order to overcome GaAs physical limitations. Therefore, in order to reach the next technological step of the frequency multiplier technology, a candidate must be found to replace GaAs.
Gallium nitride (*GaN*) has been proposed as the candidate to replace GaAs, because it is characterized by a higher electric breakdown field and higher thermal conductivity compared to GaAs. This, in turn, means enhancing the power handling capabilities of Schottky diodes, leading to simplified designs of frequency multipliers and allowing the use of more efficient configurations compared to the current GaAs frequency multipliers state of the art. Nevertheless, the use of GaN Schottky diode in frequency multipliers presents several challenges, such as a lower electron mobility compared to GaAs, and a higher series resistance in Schottky diodes, which could undermine high frequency operations and, ultimately, its conversion efficiency. Furthermore, the use of GaN Schottky diodes poses another challenge, in that there is a lack of a systematic investigation of their properties and performances.
The work presented in this thesis addresses the fabrication and characterization of quasi-vertical GaN Schottky diodes for frequency multiplier applications. The first chapter presents an introduction to THz science and applications, followed by a review of the state of the art on various types of THz sources. The current state of the art of GaAs frequency multipliers is detailed as well as an introduction to GaN and why it has been considered as a candidate to replace GaAs in Schottky diodes for frequency multiplication. The second chapter describes the fabrication process developed and employed for the fabrication of Schottky diodes. The technological challenges represented by GaN fabrication technology compared to other III-V materials are addressed, as well as the inherent problematic of GaN hetero-epitaxy. The fabrication process is then detailed, along with the strategies employed to improve the state of the surface of GaN before Schottky contact metallization. The third chapter presents the Schottky diode theory, and the characterization methods employed in order to investigate the fabricated GaN Schottky diodes. Then, the protocol used for the characterizations of GaN Schottky diodes is described, and the result obtained are presented. The conclusions summarize the work done and presents an outlook on future work and a perspective on this technology.

Contents

Abstract . . . . **i**

Résumé . . . . **iii**

Acknowledgments . . . . **v**

General Introduction . . . . **vii**

1 Context & State of the art **1**
1.1 Introduction 1
1.2 THz Applications 2
1.2.1 Astronomy 2
1.2.2 Wireless Telecommunications 4
1.2.3 Security 6
1.2.4 Biomedical Analysis 7
1.3 THz Sources 8
1.3.1 UTC-PDs 9
1.3.2 RTD 9
1.3.3 QCL 10
1.3.4 Frequency Multipliers 11
1.4 GaAs Multipliers 12
1.4.1 State of the art 12
1.4.2 Physical limitations 13
1.4.3 Design limitations 14
1.5 Gallium Nitride 15
1.5.1 Structural and Physical Properties 15
1.5.2 Applications 16
1.5.3 Why GaN? 18
1.6 GaN Multipliers 18

2 Fabrication Process **21**
2.1 General considerations 21
2.1.1 Differences between GaN and GaAs processes 21
2.1.2 GaN epitaxial technology 22
2.2 Process Outline 24
2.2.1 Mesa Definition 26
2.2.2 Ohmic Contact 27
2.2.3 Schottky Contact 32
2.2.4 Isolation 34
2.2.5 Air-Bridge 35

2.3 Surface Chemical Treatments . . . 41
2.3.1 XPS Analysis . . . 43
2.3.2 AFM Scans . . . 45
2.4 Thermal Annealing . . . 46
2.4.1 Schottky Contact AFM Scans . . . 47

3 Schottky Diode Characterization . . . 51
3.1 MS Contacts Theory . . . 51
3.1.1 Ideal Metal-Semiconductor Contacts . . . 51
3.1.2 Current Mechanism in Schottky Diodes . . . 53
3.1.3 Non-Ideal Characteristics of Schottky Diodes . . . 56
3.2 DC Characterizations . . . 60
3.2.1 TE Fit . . . 60
3.2.2 Norde's Method . . . 62
3.2.3 Cheung's Method . . . 64
3.2.4 Comparison of methods . . . 66
3.3 IV-T Characterizations . . . 67
3.4 CV Characterizations . . . 69
3.5 RF Characteristics . . . 70
3.5.1 De-embedding . . . 71
3.5.2 Junction Capacitance . . . 71
3.6 Results and Discussion . . . 74
3.7 Discussion on current conditions . . . 75
3.7.1 Richardson constant . . . 83
3.8 Breakdown voltage . . . 84
3.9 Capacitance-voltage behavior . . . 88
3.10 Small-signal RF Measurements . . . 91

4 Conclusions and Future Outlook . . . 97
4.1 Conclusions . . . 97
4.2 Future outlook . . . 98

Bibliography . . . 101

List of Figures . . . 115

List of Tables . . . 117

List of Symbols . . . 119

Publications . . . 123

Chapter 1

Context & State of the art

1.1 Introduction

The terahertz (THz) region of the electromagnetic spectrum can be considered as the last frontier, the final unexplored area.

Throughout human history, men exploited all the range of frequencies of the electromagnetic radiation to improve life and technologies: first humans relied on the radiation from the Sun and on torches. The ancient Greek and the Roman made use of candles. The more recent history saw the occurrence of gas lightning (1772) and incandescent light bulbs (1897). At the turn of the 19th and 20th century, a number of innovations and discoveries explored areas of the electromagnetic spectrum other than visible light: radio (1886-1895), X-rays (1895), UV radiation (1901), and radar (1936).

Despite great scientific interest during almost all the 20th century, the THz region of the electromagnetic spectrum remained unexplored, apart from some niche applications, due to the fact that its nature presents a challenge for both electronic and photonic technologies [1].

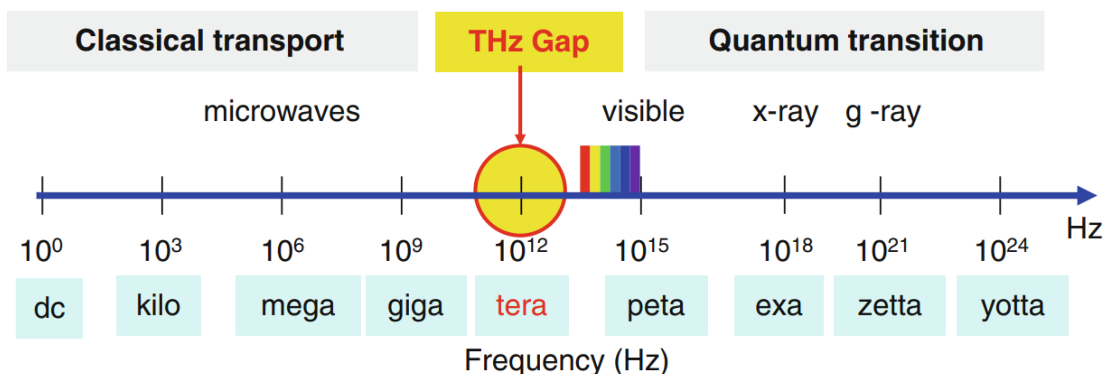

Figure 1.1: The electromagnetic spectrum

It is recognized that the THz frequencies range starts at the transition between millimeter and sub-millimeter wave, i.e. 0.3 THz and spreads up to 10 THz. In the electromagnetic spectrum (Fig. 1.1), radiation at 1 THz has a period of 1 ps, a

wavelength of 300 µm, a wavenumber of 33 cm^{-1}, a photon energy of 4.1 meV, and an equivalent temperature of 47.6 K [2].

Numerous recent breakthroughs, as well as recent technological advancements, have moved THz science in the center focus of many researchers, by virtue of its wide variety of applications: sensing molecules, security, imaging, space science and non-destructive testing, medical applications, very high data rate wireless communications. However, to grow massively, these applications require low cost, compact, portable, reliable and non-cryogenic THz sources and, especially, high power level sources. This lack is the reason why the THz frequency band is often referred to as the "THz gap". Today, many technologies are in competition towards low cost and mass-market applications where THz sources are already a vital element.

1.2 THz Applications

As mentioned above, the lack of suitable THz sources has been the greatest obstacle to develop this science. Since the late 60s and 70s tremendous effort has been done in order to bridge the THz gap. Recent technological innovations in photonic and nanotechnology have made possible to show the true potential of THz science. As of today, THz radiation has applications in a plethora of multidisciplinary subjects, such as space science, sensing and wireless communications. We will now proceed to review these application and explain what makes THz radiation unique and innovative in these areas.

1.2.1 Astronomy

Historically, the main area of application of THz science has been astronomy [3]. In fact, the THz band of the electromagnetic spectrum is a treasure trove of information about chemical species. This have allowed astronomers, Earth and space scientists to measure, collect and catalog thermal emission lines for a wide variety of light weight molecules. Approximately one-half of the total luminosity and 98% of all the photons emitted since the Big Bang fall into the sub-millimeter and far-IR bands (Fig. 1.2).

Stars are known to be formed within dense molecular and dust cloud regions of

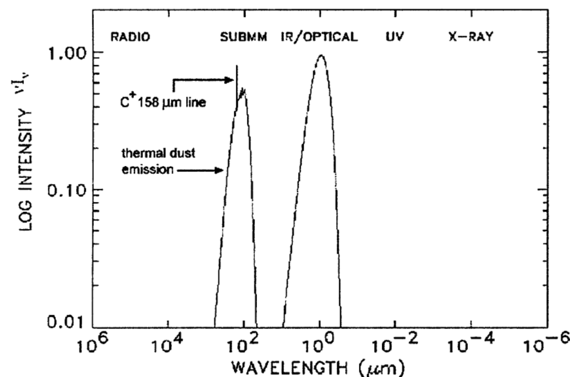

Figure 1.2: Spectrum of the Milky Way galaxy showing that at least one-half of the luminous power is emitted at sub-millimeter wavelengths [4]

the galaxy which collapse at a certain point, releasing its outer shells back to the interstellar medium. The abundance of atomic species in the interstellar medium thus provides fundamental information on the nature of the star formation activity in a given region. In addition, a fundamental step in the star-formation process is the gas cooling mechanism: when the cloud collapse due to the gravitational forces to form a star, it rids itself of the heat generated by the compression under gravity. This cooling is characterized by molecular transitions in the sub-millimeter band [5]. Specifically, the thermally excited atoms and molecules radiate (or absorb) band signals corresponding to quantum state transitions associated with specific rotational and vibrational modes. Moreover, for temperatures between 10 K and 100 K, gas and dust clouds emit continuum blackbody energy, which has its peak in the THz frequency range. Moreover, optical energy from very distant galaxies is red-shifted down into the THz band, and when detected, yields information on the state and composition of the early universe.

All the information available thanks to THz radiation justified the often expensive realization of high-altitude observatories, aircraft platforms and orbital satellites, since water and oxygen molecules in our own atmosphere prevent THz energy from being propagated at great distances under standard temperature and pressure conditions, making our atmosphere extremely opaque to THz radiation [6]. Of notable importance among astrophysics instruments are the Submillimeter Wave Astronomy Satellite (SWAS) [7], ESA Herschel space observatory [8], NASA Submillimeter Probe of the Evolution of Cosmic Structure (SPECS) [9], the SPace InfraRed Interferometric Telescope (SPIRIT).

The same instruments used for the study of interstellar and intergalactic space, can be used to monitor Earth's atmosphere: the study and monitoring of quantity, distribution and reaction rates of water, oxygen, chlorine and nitrogen to cite a few, is of fundamental importance for the supervision and examination of processes that are of relevance to human society such as global warming, ozone destruction, total radiation balance and pollution monitoring. May key species have thermal emission lines in the sub-millimeter band (Fig. 1.3).

The other major application of THz sensors for space science is the observation of the atmosphere of planets and small celestial bodies (moons, asteroids and comets). The comprehension of the atmospheric conditions of these bodies allows us to correct and refine the model of our own atmosphere, the atmospheres of inner planets such as Venus and Mars, outer planets such as Jupiter and Saturn and their moons (e.g. Europa and Titan), as well as gaining important knowledge about the formation and evolution of the solar system. Among all the various probes sent to a great number of celestial bodies in our system, of highly importance is the Rosetta mission (ESA) [10], a spacecraft launched in order to intercept and orbit Comet 67P/ChuryumovGerasimenko (67P/C-G), designed to complete the most detailed study of a comet ever attempted. One of the 11 science instruments onboard the Rosetta orbiter was a millimeter/sub-millimeter wave spectroscopic instrument named Microwave Instrument for the Rosetta Orbiter (MIRO), with the purpose of measuring the nucleus surface and near-surface temperatures and the composition of volatile gases in the comet.

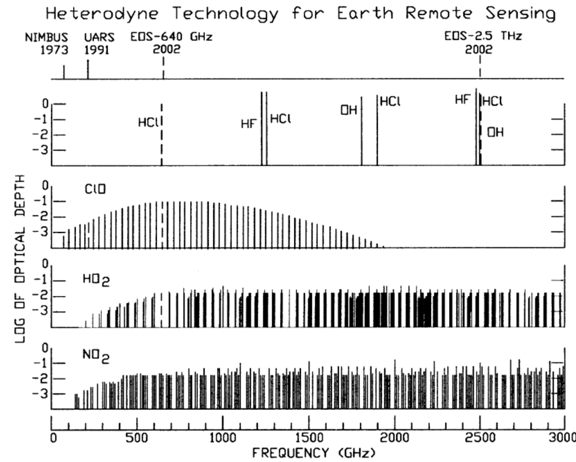

Figure 1.3: Spectra of some important molecules in the Earth's upper atmosphere and measurements being addressed by NASA heterodyne instruments. The peak power or minimum frequency for many emission lines occurs in the terahertz region [3]

1.2.2 Wireless Telecommunications

There is no doubt that, in this day and age, our society is intrinsically dependent on telecommunications. Since the advent of the Internet and the first mobile phones, we witnessed an unprecedented transformation of our lifestyle: how we communicate with each other, how we work, how we learn, how we consume multimedia. This has been made possible also thanks to all the technological advancements in devices and in telecommunications. Since the latter half of the 1990s, internet traffic has been steadily increasing worldwide, a traffic which was for the most part consumed via wired networks. Recently however, with the introduction of new mobile devices and new multimedia services working in wireless environments, the trend gradually shifted to wireless networks. Both the number of users and the amount of data consumed rose dramatically. As a direct consequence of this, great effort has been put into the development of wireless communication networks capable of satisfying the increasing demand of an increasingly interconnected society. Therefore, the data capacity of wireless communications grew much faster than wired networks [11].

To satisfy the needs of an increasingly interconnected society, it is of extreme importance a high data rate and a large bandwidth. According to Edholm's law of bandwidth [12], the demand of bandwidth in wireless communications has doubled every 18 months over the last 25 years.
In many current wireless network systems operating at microwaves, data capacity has been improved by increasing spectral efficiency. However, achieving faster rates ($\geq 10\,\text{Gbit/s}$) is very challenging due to a fundamental limitation of current technologies: narrow bandwidth. Diverse solutions are being proposed to overcome this limit, all relying on the principle of increasing the spectral efficiency. Nonetheless, the main other proposed solution for next generation wireless networks is increasing the carrier frequency itself, through the use of THz waves [13].

What was once though to be out of reach, due to the lack of suitable sources and detectors, could become a reality in the near future thanks to the massive research

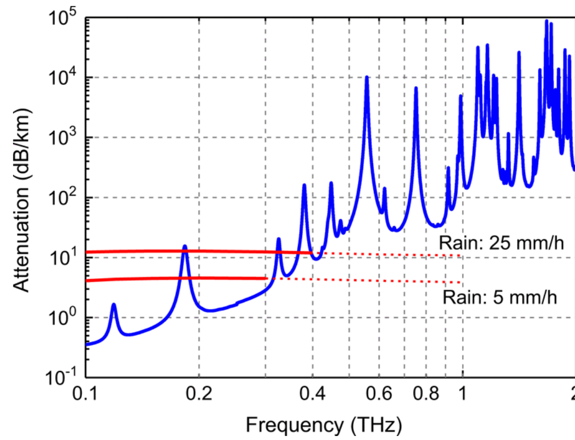

Figure 1.4: Atmospheric attenuation computed at sea-level altitude, water content of 7.5 g/m^3, and atmospheric temperature of 20 °C [11].

that has been undergone in the last few years to fill this lack. Frequencies above 275–300 GHz are still free both in Europe and the USA, which suggests that they could be assigned to new services relying on T-ray communications.
Several configurations could be envisaged [14] for THz links, e.g. as very high data rate indoor links or as direct bridge with optical fibers.

However, all the possible future scenarios would have to deal with the intrinsically short path of length and line of sight communication. The attenuation in the atmosphere at frequencies above 100 GHz is much larger than that in the microwave band, and the large attenuation also degrades the signal-to-noise ration (SNR), which influences the data capacity as well. It would be difficult to use THz waves as a carrier frequency due to the inevitable loss that can be caused by weather conditions, such as rain (Fig. 1.4). Still, this may not be a problem for indoor applications (for a 300 GHz signal the attenuation would be around 0.1 dB for a 10 m long indoor link). Nevertheless, the advantages of using THz waves as a carrier frequency are more than enough to push a great number of research projects in this direction [15]:

- The aforementioned higher bandwidth capacity compared to microwave systems;
- THz communications can support ultrahigh bandwidth spread spectrum systems, which can enable secure communication giving protection against channel jamming attacks [15];
- Under certain atmospheric conditions, THz waves are characterized by lower attenuation compared to IR. As a consequence, under certain conditions, THz links can be a viable solution for situations where IR-based networks would fail;
- THz communications can provide an answer to the first and last mile problem (the first and last mile problem refers to establishing broadbanded, multi-user local wireless connections to high speed networks);
- As said before, the THz frequency range is largely unregulated.

1.2.3 Security

Recent technological improvements in THz sources and detectors have shed a new light on a number of applications that were already theorized in the past, but were not pursued strongly due to the limitations of the technology. Now, historically, the main application for THz radiation has always been spectroscopy, whether for chemical species in a laboratory or for space science. Nevertheless, due to the number of phenomenological advantages that this part of the electromagnetic spectrum offers compared to the others, several sensing and imaging applications that in the past were only theory may become reality in a few years [16].

The ability to detect guns, knives, improvised explosive devices (IEDs), and, moreover, to detect chemical and biological agents is seen as an important tool for security and defense. While there are already plenty of instruments that operate at the millimeter wavebands, THz waves could offer some advantages [17, 18]:

- THz radiation is transmitted through most non-metallic and non-polar mediums, such as paper, plastic, cardboard, clothing, shoes, backpacks, etc., thus enabling the ability to see through any concealing barrier of this kind (although it is completely blocked by metal or polar molecules, such as water);
- Many chemical and biological agents of interest for security applications (such as explosives) have characteristic THz spectra that can be used to "fingerprint" and thus identify these materials even when they are concealed inside a packet or under clothing;
- The shorter wavelength of THz radiation compared to microwaves yields higher resolution of the images. Moreover, thanks to pulsed THz techniques, there is the possibility of 3D imaging;
- THz radiation poses either no or minimal risk to a suspect being scanned or to an operator using a THz system (the low energy of THz radiation would be harmlessly dissipated as heat in the first 100 µm of skin tissue).

In essence, THz systems, thanks to the inherent better spatial resolution and high specificity, have the potential to overcome a well-developed technology like millimeter wave (MMW) imaging (which operates at a frequency of roughly 30 GHz). As plastic explosive, fertilizer bombs and chemical and biological agents are progressively more used in war or in terrorism, the search for a system which can easily and readily identify these threats becomes much more important. Many explosives (e.g. C-4, HMX, RDX, TNT) and also illegal drugs (e.g. methamphetamine) have already their spectra been identified in the THz range, and in the literature there are a number of proof-of-principle measurements reported [19, 20]. This is of high importance, since there is no "fingerprint" counterpart for explosive in the MMW range [18]. A THz image of a person would show the outline of clothing and the reflection of object beneath, but the person's skin would appear dark (Fig. 1.5).

The detection of explosives is also of particular interest for the elimination of landmines. It is estimated that more than 100 million mines still remain active and undetected in many parts of the world [22], as leftovers from past conflicts. These mines claim more than 30000 lives or injuries each year. Existing anti-landmines technologies are characterized by a high number of false positives, due to the pres-

Figure 1.5: Active and passive images: on the left, 94-GHz passive image: metal knife inside newspaper; on the right, 640 GHz active image: toy gun under cotton shirt [21]

ence of other objects in the area. The employment of THz systems for the detection of landmines should yield a higher efficiency [23].

In light of all these advantages, this application poses some challenges, the main one being atmospheric attenuation [21], which can greatly impact the performances of an hypothetical THz security system depending on weather conditions (rain, fog, etc.). Some also ponders if the advantages of the use of THz radiation can really outweight the disadvantages due to the technological limitations, as compared to existing methods of security screening at lower frequencies [24].

1.2.4 Biomedical Analysis

The same technological advancements in THz science that allowed to expand the applications of THz radiations from its niche in space science, have also opened up in the last 20 years a new area of application in biology and medicine.

Because of its low energy (1–12 meV), THz radiation is non-ionizing, i.e., it can be used for sensing and imaging purposes without the risk of destroying the sample. Moreover, since energies of 10^{-21}J are consistent with discrete molecular vibrational and rotational modes, there is much spectroscopic interest [25].

Because THz waves interact with vibrations and rotations of molecules, they can be used to identify specific molecules based on their spectral features. Although there are plenty of imaging techniques and tools for biological molecules or medical purposes, THz spectroscopy research in this field is intended as a complement to other electromagnetic spectroscopy methods [22].

THz wave spectra of small molecules can be obtained if the samples are solid-state or dissolved in non-polar liquids.
THz radiation is completely absorbed by polar molecules, such as water. This makes virtually impossible penetration through biological tissues of any substantial thickness. However, this property makes possible to obtain high contrast between substances with different degrees of water absorption.
The most reliable method of application for submillimeter-wave spectroscopy involve the comparison of reflection or absorption signatures when the sample undergoes some form of chemical or physical change. One kind of molecule that can be characterized by THz wave are proteins. Proteins are one of the most impor-

tant functional material in human biology. Its function and activity is determined not only by its molecular structure but also by the shape and configuration of the molecule. When a protein is formed, it folds into a unique shape that determines its function. Through THz wave spectroscopy, one can investigate the dynamic of the vibration of a protein molecule after it was excited.

Other interesting applications in this sector are measurement of avidin-biotin binding and DNA hybridization [26, 27]. Avidin-biotin binding is of extreme importance in the biotechnological industry since it is used for binding molecules to surfaces in selective chromatography, drug delivery or fluorescent tagging. The binding process produce a change in the index of refraction of the surface film that can be translated in a change in reflection of a THz beam, this method posing as an easier alternative to existing techniques. A similar change occurs when DNA is hybridized. Because of the advantages of THz radiation, this is a powerful method for label-free determination of the change of state of many molecules relevant to biological processes.

1.3 THz Sources

For most of the 20$^{\text{th}}$ century, terahertz technology was limited to a niche of applications regarding astronomy, space science and spectroscopy. These scientific sectors were the main fuel for the research and development of THz sources, sensors and systems. Year after year, the THz region of the electromagnetic spectrum went from being one of the least utilized electromagnetic bands to a broader science are that encompass many multidisciplinary applications, as illustrated before.

This was due to the technological improvements and breakthroughs made in the last few decades that have made possible the availability of THz sources, detectors and systems to a greater number of laboratories in the world and at a lower cost.

However, while for most of the THz instruments, giant leaps and improvements have been made, the same cannot be said for THz sources. This has been historically the main problem in the development of almost all the actual real-life application for THz science. Recent developments have made improvements in terms of availability of valid sources for use in scientific, civilian, industrial or military applications.

There are numerous ways to generate power at THz frequencies. Many type of sources, both electronic and photonic, were developed over the years, each with their own limitation. Some of them are inherently limited to a certain kind of application, many are limited in terms of output power or require cryogenic temperatures to work, and others are limited by their size, excessive cost or complexity [28].

Fig. 1.6 shows a number of THz sources as a function of frequency. Above 10 THz is the domain of gas lasers, quantum cascade lasers (QCL) and other optical techniques. Between 1 THz and 10 THz we find mainly solid-state sources, like frequency multipliers, and photonic sources, such as uni-traveling-carrier photodiodes.

Below 1 THz we have other electronic sources like HEMT, HBT, Gunn diodes and resonant tunneling diodes (RTD).

We will proceed now to analyze a few of the main methods and devices to generate THz radiation.

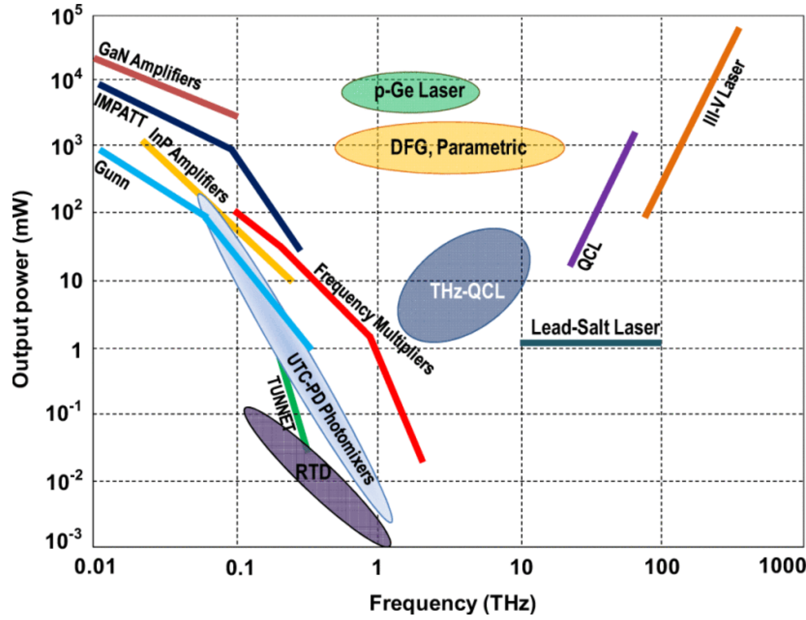

Figure 1.6: THz sources as a function of frequency [28]

1.3.1 UTC-PDs

A simple photonic generation method for THz waves relies on the photomixing principle. Photomixers are nonlinear photoconductors with very short lifetime and are primarily fabricated using low-temperature-grown GaAs. Among the various types of photodiode technologies used for THz photomixing, uni-travelling-carrier photodiodes (UTC-PD) exhibited the highest output power at frequencies ranging from 100 GHz to 1 THz [29]. A big advantage of using photonic sources for THz waves generation is that optical fiber cables can be used to distribute THz signals over long distances with very low loss. UTC-PDs can be a valuable alternative to more expensive and/or bulky sources for THz , finding good applications in situation where large tunability is demanded, like spectroscopy of many species or telecommunication with a high bit-rate [30], although their generated powers are lower than those from other sources. The only other sources able to cover a similar band in the THz region are frequency multipliers.

The current state of the art is a coherent THz link at 200 GHz, with an output power of 3 µW using a photocurrent of 1 mA, and 1.5 µW using a photocurrent of 0.7 mA [31].

1.3.2 RTD

Resonant Tunneling Diodes (RTD) have the highest oscillation frequency among electronic devices for THz generation. A typical RTD oscillator is integrated with a planar slot resonator. The RTD is located at the center of a slot in a metal film. This slot forms a standing wave of the electromagnetic field as a resonator and also acts as an antenna by radiating output power at the same time. The RTD is normally composed of two heterobarriers and a quantum well. In the current-voltage characteristics, a current peak exists at which the resonance level in the quantum well is close to the conduction band edge of the emitter. With increasing voltage

above the current peak, the IV curve exhibits a negative differential conductance region.

The electron transport through RTD barriers is taking place via capture/escape processes to/from the resonant states in the quantum well (QW) [32]. Therefore it is usually assumed that the tunnel lifetime (τ) of electrons on the resonant states in the QW determines the relaxation processes inside RTDs and imposes a fundamental limit on the operating frequencies of the diodes. As a consequence, RTDs for high-frequency applications are made with thin barriers [33] to minimize τ and to speed up the transport and relaxation processes as much as possible. The achievable minimal barrier thickness is limited due to technological reasons. A barrier thickness of 1 nm is close to the limit achievable in practice [34]. Another optimization approach is the use of weakly doped or undoped spacer layers on the collector side of an RTD to reduce the RTD capacitance [35].

The current state of the art is represented by RTD characterized by oscillations up to 1.92 THz with an output power of approximately 0.4 µW [36].

1.3.3 QCL

Terahertz quantum cascade lasers (QCLs) are a class of unipolar semiconductor lasers that use intersubbands transitions between electronic states of a quantum well superlattice that is engineered to produce the desired wavelength of emitted radiation. The band diagram of a typical QCL design can be seen in Fig. 1.7 showing the process of electron recycling and photon emission: electrons from the injector are made tunneling by an electric field in the quantum wells active region where, for currents higher than a threshold current to achieve population inversion like in a standard laser, they are induced to transit in a lower level by stimulated emission and then tunneling in the energetically lower injector to restart the mechanism.

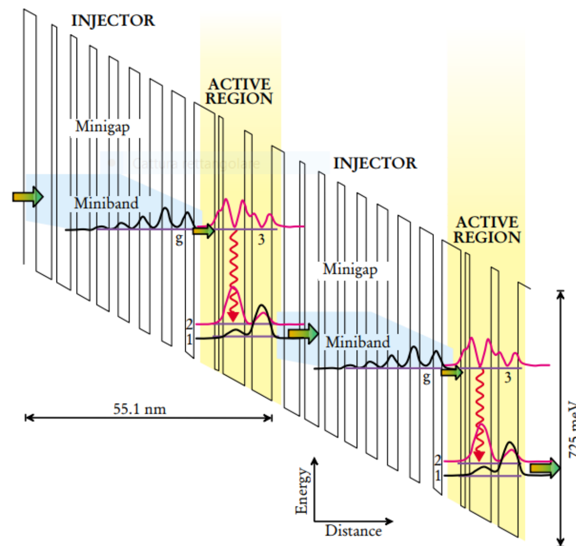

Figure 1.7: Band diagram of a QCL stage, from [37]

The first QCL was demonstrated at 75 THz at Bell Labs in 1994 [38]. Since then, QCLs have become the dominant mid-infrared semiconductor laser sources, with

spectral coverage typically from 12 THz to 100 THz. The first QCL working in the terahertz band (4.4 THz) was reported in 2001 [39].

Terahertz QCL's size is measured in millimeters, and the package size is primarily limited by cooling requirements. The best high temperature lasers make use of a so-called "metal-metal" waveguide, where the terahertz mode is tightly confined on a sub-wavelength dimension between metal contacts placed immediately above and below the thick epitaxial active region. Such waveguides are fabricated using a process of metallic wafer bonding and substrate removal, followed by standard micro-litographic processing [40]. Metal-metal waveguide QCLs are preferred as THz sources because they are the only type of QCLs that can operate in CW mode over 77 K [41]. Terahertz QCL have been demonstrated as local oscillators by pumping hot-electron bolometer mixers at various frequencies [42] and they have been actively used in terahertz imaging applications [43]. However, they suffer from poor beam quality, low coupling efficiency and narrow bandwidth. They are also difficult to phase lock and need cryogenic temperatures.

1.3.4 Frequency Multipliers

Among electronic sources for THz radiation, frequency multipliers occupy a special place.
Frequency multipliers are nonlinear devices which convert an input sinusoidal signal into a specific output harmonic, while suppressing undesired ones. They require a matching network at the input and at the output, in order to optimize power transfer from the input signal to the desired harmonic at the output and filter all unwanted harmonics. The conversion principle relies on a non-linear device.

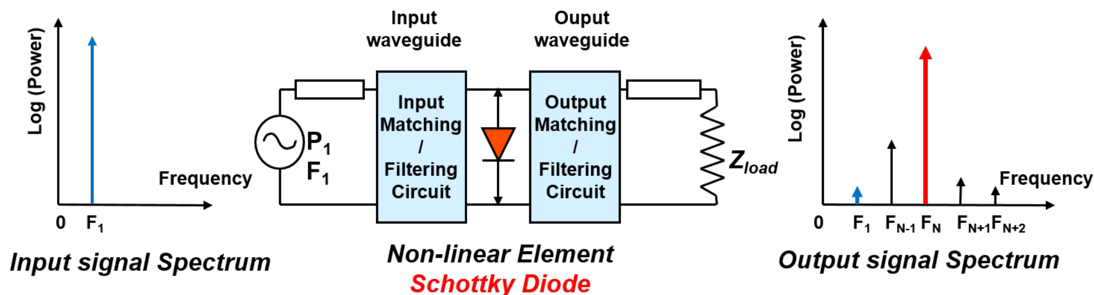

Figure 1.8: A schematic view of a frequency multiplier

Historically, frequency multipliers used whisker-contacted Schottky diodes. These instruments were fundamental in the development of heterodyne receivers for radio astronomy and planetary science [44]. Although this technology was mature and well-known, this generation of frequency multipliers had great difficulties to overcome the 1 THz milestone. At submillimeter-wavelengths, whisker diodes outperformed planar Schottky diodes in terms of lower parasitic capacitance and lower series resistance. However, at millimeter-wavelengths, planar Schottky diodes started to give better performances due to technological improvements and design considerations.

The improvements in planar Schottky diodes technology allowed to shift from discrete semiconductor chips mounted on hybrid circuits (whose inherent technological

limitations affected directly efficiency and output power) to monolithic microwave integrated circuits (MMIC) fabricated on thin semiconductors [28]. Planar Schottky diodes turned out to be the most popular device for building frequency multipliers working above 150 GHz, because of the simplicity in controlling the technology [45].

At this point, the main limitation of a frequency multiplier were related to the power handling capabilities and the self-heating of the diodes induced by RF power dissipation. The introduction of multi anode frequency multipliers permitted to push performances by improving these aspects. Arrays of diodes, made possible with planar diode technology, allows to increase the area and the number of diodes, while parallel diodes configurations grant the liberty to design balanced topologies that have the goal of power division, thus reducing the thermal stress per diode [46]. From the substrate point of view, the use of high thermal conductivity substrates can improve thermal management, but this impact the fabrication process.

The most typical configuration are doublers and triplers. Doublers have the advantage of balanced design, which produce very low spurious harmonic output whitout the need for any filtering [47, 48]. Triplers instead, are harder to build because they need filters at the input and output, as well as careful tuning of the circuit at the second harmonic [28].

Among all the materials used to fabricate Schottky diodes, GaAs is the preferential choice, because of the fact that this technology has reached its full maturity.

1.4 GaAs Frequency Multipliers

Gallium Arsenide (GaAs) has been the material of choice for the fabrication of Schottky diodes for frequency multipliers. Frequency multipliers based on GaAs Schottky diodes have advantages of wideband, high efficiency and stabilized continuous wave output compared to the other types of technology described until now.

1.4.1 State of the art

One notable example of GaAs frequency multiplier is given by the Heterodyne Instrument for the Far Infrared (HIFI), one of three instruments of the Herschel Space Observatory launched by the European Space Agency in May 2009. It is a very high resolution spectrometer covering a frequency range from 480 GHz to 1900 GHz with very high spatial resolution and receiver sensitivities, used to probe astronomical objects via their rotational molecular lines [8].
Due to the high frequency requirements, a total of 14 local oscillators were necessary. The objective was to deliver about 2 µW of output power over 10% of fractional bandwidth. Starting from a module delivering 100–150 mW at room temperature, the frequency was multiplied three to four times using a $\times 2 \times 2 \times 2 \times 2$ scheme for the 1.4–1.6 THz channel or a $\times 2 \times 3 \times 3$ scheme for the 1.6–1.9 THz channels. The frequency multipliers were also passively cooled at 120 K to increase the output power of the highest frequency local oscillator chains. This improvement was possible because as the device is cooled, the GaAs mobility improves thus improving the performance of each diode, the ohmic losses associated with the waveguides

and the matching circuits decrease due to lower phonon scattering and as the drive power increases, the efficiency of the last stage increases significantly since, at room temperature, the last stage is often under-pumped.

The current state of the art in the literature is 3 µW at 1.9 THz [49], 15–20 µW at 1.5–1.6 THz [50, 51], and 100 µW at 1.2 THz [52], powers that improve dramatically when cooled around 120 K [53]. It was also demonstrated a 2.48–2.75 THz solid-state source that produces power levels of several microwatts at room temperature [54].

1.4.2 Physical limitations

Theoretically, it is possible for a varactor frequency multiplier (a frequency multiplier which use a Schottky diode reactive nonlinearity as active element) to convert all the input power to a higher harmonic (i.e., pure reactance). In practice, it is impossible to achieve the theoretical efficiency due to all the various circuit losses. For instance, the series resistance R_S slowly increases with frequency, impacting the efficiency which, in turn, can be very low.

The maximum voltage amplitude that can be produced across the diode capacitance also limits the power handling of the multipliers, and it is influenced by three effects [28, 55]. The first is the breakdown voltage, which is the threshold above which excessive leakage current occurs. The breakdown voltage determines the maximum nonlinearity that may be developed by the junction. At low frequencies, efficiencies are generally limited by the breakdown voltage. As the frequency increases, a second effect starts to be relevant: the mobility of the carriers in the diode. Since the number of carriers within the junction is limited, there is a maximum value of the current. If one tries to drive higher currents, this will result in a very large resistance, effectively clipping the current at this saturated value. The saturation current greatly limits the voltage amplitude at high frequencies. As the electric field in a GaAs sample is increased, the velocity and thus the current reaches a peak, then begins to decline due to electrons gaining enough energy from the field to scatter in the upper low-mobility regions. This acts as a current limit in the undepleted region of the diode. The efficiency is affected by this mechanism because it decreases the ability of the charge of the depletion region to modulate the capacitance and generate the nonlinearity. Moreover, as the frequency increases and goes into the THz region, time constants associated with the transfer must be taken into account.

Last but not least, for a given junction capacitance, the voltage amplitude is limited by the input power. At low frequency, as sufficiently satisfying voltage amplitude may be reached by reducing the diode capacitance, but at higher frequencies, a point is reached where the diode cannot be scaled anymore, and the input power is still too small. At this limit, the diode cannot any longer work in varactor mode because the optimum bias point changes from reverse bias to forward bias. In this bias region, for low input power, the efficiency can be significantly larger compared to a varactor diode, but the absolute efficiency is never large because the nonlinearity is due to a voltage variable resistance rather than a reactance.

1.4.3 Design limitations

As we have seen up until now, frequency multipliers have been the preferential choice as for solid-state electronic source of THz radiation for the lower part of the so called THz gap. GaAs is the current standard material used for the fabrication of Schottky diodes for this application, but has inherent physical limitation when one tries to increase the frequency operation. However, what cannot be reached through physical optimization of the diode alone, can be attained through improvements in the design of the frequency multiplier circuit.

One such strategy is the use of array of diodes, made possible with planar diode technology. The series array allows to increase both the area and the number of diodes, while parallel arrays yield balanced topologies and power division, thus reducing the thermal stress per diode [46].
Thus, multi anode frequency multiplier technology can overcome certain physical limitation of the material used for the diode but it is not free from constraints. First of all, only a finite number of diodes can fit on a device due to technological constraints. Then, the thickness of the substrate, which acts as a heat sink, cannot be increased beyond the point where RF performances are significantly degraded, limiting directly the total RF power that can be coupled to the circuit. Using a high thermal conductivity substrate can improve thermal management but at the expense of a more complex fabrication process. Lastly, frequency multipliers with several pair of diodes are more difficult to balance compared to those with a single pair, limiting the conversion efficiency of the multiplier for a given input power per anode [45].

Another way to increase the output power is to power combine at the circuit level. Several independent devices are integrated in a single waveguide circuit using couplers and/or Y-junctions. Yet, these topologies suffer from some drawbacks at THz frequencies. The use of a Y-junction tends to be electrically long, and produces excess loss at these frequencies. It also limits the possibility to power combine numerous devices efficiently on the same circuit, due to the technological constraints that such strategy introduces in the fabrication process. Aligning multiple small chips inside the waveguide at THz frequencies is challenging, and any misalignment affects the design. One way to overcome these drawbacks would be the "on-chip" approach, i.e., performing power combining directly on the chip. Still, considering that the input and output waveguides are perpendicular to the waveguide channel where the diodes are located, it becomes clear that this is very difficult to fabricate with traditional fabrication techniques.

GaAs frequency multipliers are ultimately a well-known technology, which has been employed with success, but as the requirements for the output frequency from a solid-state electronic THz source become more and more high, it is clear that other paths must be investigated, apart from physical or design optimization.
It is because of this consideration that, in the recent years, groups around the world have been investigating alternatives to the Schottky diode itself as active element of the frequency multiplier and also on an alternative material to GaAs, one that could offer better power handling and yield an improved overall thermal conductivity. One such candidate is Gallium Nitride (GaN).

1.5 Gallium Nitride

In this section, we will proceed to illustrate the basic properties of Gallium Nitride (GaN), the existing applications and the reason why in the scientific literature it is indicated as the ideal candidate for substituting GaAs in the fabrication of Schottky diode for frequency multipliers and why it is believed that with this technology, the next technological step can be achieved.

1.5.1 Structural and Physical Properties

GaN belongs to the family of III-V nitrides. This class of materials can have a wurtzite, zincblende and rocksalt crystal structure. The thermodynamically stable structure for GaN is wurtzite. The wurtzite structure has a hexagonal unit cell characterized by two lattice constants, a and c, with respective values of 3.189 Å and 5.185 Å (Fig. 1.9). The band structure of wurtzite GaN can be seen in Fig. 1.10, and a short summary of some of bulk GaN properties is reported in Table 1.1.

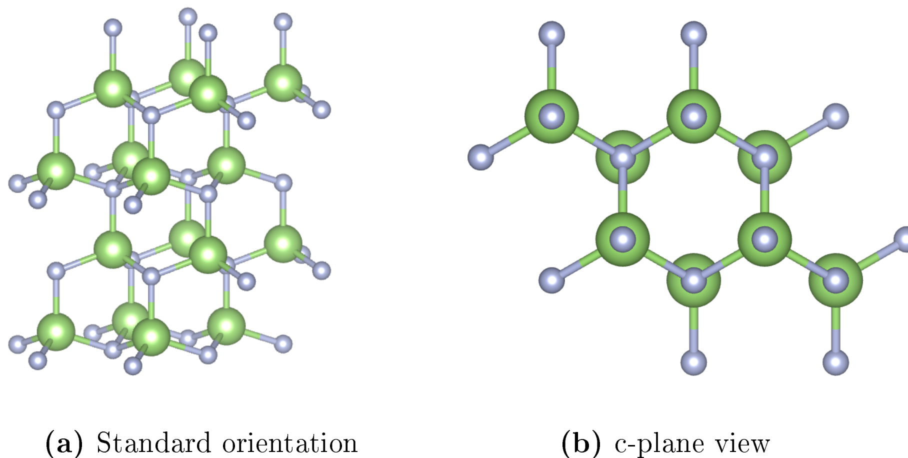

(a) Standard orientation **(b)** c-plane view

Figure 1.9: Crystal lattice of wurtzite GaN

GaN is a wide-bandgap material due to its direct bandgap of 3.4 eV, which is larger than that of Si (1.12 eV) and GaAs (1.42 eV). In the literature there are several reported values for the breakdown field of GaN. This can be associated to the fact that the epitaxy of GaN is not a completely well-developed technology. Consequently, the exact value of the breakdown field may change because of different epitaxial techniques used, i.e. different substrates and growing methods. The epitaxy of GaN is still far from being a mature technology, compared to that of Si or GaAs [56–58].

This same drawback is believed to be responsible for the large background n-type carrier concentrations. In the early years of research in GaN technology, this together with the difficulties in obtaining p-type doping and challenging fabrication process proved to be a bottleneck for progress. There is disagreement in the literature regarding many physical properties of GaN due to the fact that measurements were made on samples of highly varying quality. In some cases a consensus was developed, while in other cases there are still contrasting values due to the lack of measurements or due to the quality of material.

Property	Value
Lattice constant (a)	3.189 Å
Lattice constant (c)	5.185 Å
Density	$6.095\,g/cm^3$
Melting point	∼2500 °C
Thermal conductivity	1.3–2.2 W/(cm K)
Thermal expansion coeff.	along $a = 5.59 \cdot 10^{-6}\,K^{-1}$
	along $c = 7.75 \cdot 10^{-6}\,K^{-1}$
Static dielectric constant	8.9
Bandgap	3.4 eV
Electron effective mass	0.20
Hole effective mass	0.59

Table 1.1: Bulk GaN properties [59, 60]

Technological improvements in the last 30 years can be traced back to the renewed popularity of GaN after the first evidences of blue light emission [61]. After that, epitaxy improved at the point of obtaining background electron concentrations as low as $4 \cdot 10^{16}\,cm^{-3}$. Successful development of a growth technology for obtaining p-type GaN has led to pn junction LEDs in the violet, blue, green and yellow bands of the visible spectrum.

Since it was synthesized for the first time by Johnson et al. [63] in 1928, extensive information about GaN indicated it as an extremely stable compound that also exhibits significant hardness. This chemical stability combined with its hardness has made GaN an attractive material for protective coatings. Moreover, due to its high bandgap, GaN is also an excellent candidate for harsh environment electronics, i.e. in high temperature and caustic environments [64–67]. The same chemical stability that renders GaN an ideal material for device operation in harsh environments, poses however a technological challenge: conventional wet etching techniques used in semiconductor processing are not very effective with GaN device fabrication. It is for this reason that for fabricating GaN electronic devices one should use dry etching techniques.

1.5.2 Applications

Historically, the first blue LEDs were fabricated with SiC or II-VI compounds such as zinc oxide (ZnO) [68]. However, SiC LEDs were not very efficient because of silicon carbide's indirect bandgap and the devices based on II-VI compunds suffered from very short lifetimes for commercial applications. In 1993, Nakamura et al. [69] realized high brightness blue GaN-based LEDs that were 100 times brighter than the previous blue SiC LEDs. Some GaN-based LED applications are back-lighting

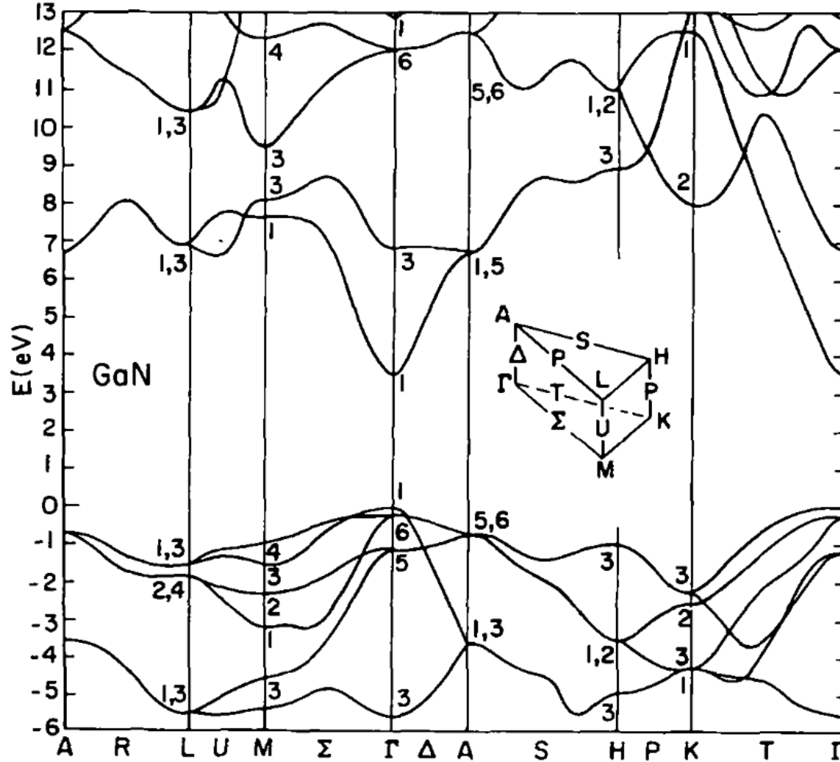

Figure 1.10: Wurtzite GaN band structure calculated with an empirical pseudopotential method in [62].

(telephones), white light (flashlights, car lights), general lighting and medical (sensors).

Addition of Indium (In) to GaN narrows the bandgap, while adding Aluminum (Al) to GaN results in a widening of the bandgap. All these ternary alloys possess wurtzite structure which is the most thermodynamically stable at ambient conditions. By varying the presence of Al and/or In in these alloys, it is possible to obtain the entire UV and visible light spectrum within the III-Nitride family. This availability of heterostructures is the main advantage of III-Nitride materials over other wide bandgap semiconductors. For the AlGaN/GaN heterostructures, the sheet charge is a result of the large spontaneous and piezoelectric polarization-induced field and large conduction band offset. This built-in field induces a two-dimensional electron gas (2DEG) that is linearly proportional to the Al-mole fraction across typical Al contents of $< 30\%$. A sheet electron density above $1 \cdot 10^{13}\,\mathrm{cm}^{-2}$ can be realized, representing an improvement of 5-10X with respect to typical GaAs or InP pHEMTs. The associated mobility at this high current density is typically in the range of 1300–2000 $\mathrm{cm}^2\,\mathrm{V}^{-1}\,\mathrm{s}^{-1}$ [70].

Another field of application for GaN can be found in laser diodes (LDs). Infrared AlGaAs-based and red AlInGaP-based laser diodes can be found in today's CD and DVD systems. To increase the storage capacity on a CD, the pit size must be made smaller. A shorter wavelength LD is required to focus onto the smaller pit size. The current generation of DVD systems uses LD with an emission wavelength of 650 nm. The increasing availability GaN-based blue-violet LDs with

an emission wavelength of 405 nm have allowed the definition of a new standard, first commercialized by Sony, who established the Blu-ray Disc consortium. GaN-based blue LDs are also used for laser-induced fluorescence method (LIF) employing endogenous and exogenous fluorophores. LIF is applied for clinical diagnosis in dermatology, gynecology urology, lung tumors as well as for early dentin caries. This method uses excitation radiation with a wavelength around 400 nm that could only be applied using tunable dye lasers or titanium lasers. Development of GaN-based LDs provides the possibility to design portable, compact diagnostic devices [71].

1.5.3 Why GaN?

Frequency multipliers have the potential to become a compact, low-cost portable, reliable, tunable, broadband and, above all, high-power source in the so-called "THz gap".

As illustrated before, the main physical limitations of GaAs frequency multipliers in terms of breakdown voltage, thermal conductivity which, in turn, affect the design (limited numbers of anodes in an array for frequency multiplication), fatally cripples this technology. Ideally, the next generation of Schottky frequency multipliers is expected to deliver an output power one order of magnitude higher than the current reference [72].

All of these considerations bring to a logical conclusion: in order for this particular technology to progress further, a candidate must be found exhibiting higher electric breakdown field and higher thermal conductivity with respect to GaAs [73].

Gallium nitride can have a breakdown voltage which can exceed $3.5\,\mathrm{MV\,cm^{-1}}$ [58]. Its intrinsic carrier concentration at room temperature is $2.8 \cdot 10^{-10}\,\mathrm{cm^{-3}}$, compared to $2.1 \cdot 10^{6}\,\mathrm{cm^{-3}}$ for GaAs. This concentration allows sustaining very high temperatures, without being affected by thermally generated carriers. Both the high breakdown field and low intrinsic carrier concentration are crucial attributes for the enhancement of power handling capability of GaN Schottky diodes. These enhanced power handling capabilities of GaN diodes can lead to simplified designs of frequency multipliers, allowing the use of simplified configurations, compared to the state of the art of GaAs frequency multipliers. Theoretical studies suggest that eight GaAs diodes are required for a 200 GHz doubler with input power of 150 mW, while one GaN diode with similar anode area is capable of handling this input power [74].

Table 1.2 lists some of GaN properties compared to other common semiconductors.

1.6 GaN Frequency Multipliers State of the art

Although obtaining terahertz GaN Schottky diodes remains a major technological challenge, in recent years, a number of works demonstrated the capabilities of GaN Schottky diode frequency multipliers. Some initial works on homo-epitaxial GaN were reported in 2015 [78]. C. Jin et al, using a novel fabrication process with E-Beam technology, realized and characterized a GaN Schottky diode with cut-off frequency around 200 GHz at zero bias, and 1.2 THz at -8 V [79]. A frequency

	GaN	**GaAs**	**Si**	**AlN**	**6H-SiC**
Bandgap (eV)	3.4	1.4	1.1	6.2	2.9
@300 °C	(direct)	(indirect)	(direct)	(direct)	(indirect)
Mobility ($cm^2/(V\,s)$)	1000	8500	1400	135	600
Saturation velocity (10^7 cm/s)	2.5	2	1	1.4	2
Breakdown field (10^6 V/cm)	~ 3.5	0.4	0.3	/	4
Thermal conductivity (W/cm)	1.5	0.5	1.5	2	5

Table 1.2: Properties of GaN and other common semiconductors [58, 60, 75–77]

tripler with a peak output of 2.1 mW at 103.5 GHz, using only four GaN Schottky diodes in series, was demonstrated in 2016 [80], as well as a GaN planar Schottky diode with cutoff frequency of 902 GHz [81].

More recently, some new work on GaN on SiC diodes was published: Liang et al. [82] reported a Schottky diode with cutoff frequency of 459 GHz and a subsequent frequency doubler able to generate over 200 mW of output power with an efficiency between 9.5% and 11.8% from 177–183 GHz.

Chapter 2

Fabrication Process

2.1 General considerations

2.1.1 Differences between GaN and GaAs processes

The material properties of GaN pose an intrinsic technological challenge: unlike GaAs, which can be easily wet etched, thus permitting a high degree of flexibility in the design and execution of the technological fabrication, only molten salts such as KOH or NaOH at relatively high temperatures ($\sim 250\,°C$) can etch GaN at acceptable rates. Moreover, the application of this kind of wet etching faces difficulties in handling this mixtures and the inability to find durable masks that will hold the etching.

Dry etch of GaN is further complicated by its inherent inert chemical nature and strong bond energies (typical of most of the group-III nitrides). GaN has a bond energy of 8.92 eV/atom, as compared to GaAs which has a bond energy of 6.52 eV/atom [83].

Consequently, a significant amount of effort has been poured in the development of dry etch processing. Initially, this development was focused on mesa structure definition, where high etch rates, anisotropic profiles, smooth sidewalls and similar etch rates for different materials were required [84–86]. However, as interest in high power devices increased, these requirements expanded to include also smooth surface morphology, low plasma-induced damage and selective etching [87–89].

The two dominant techniques widely used in group-III nitrides technology, and also used in the fabrication process detailed in this chapter, are the Reactive Ion Etching (RIE) and Inductively Coupled Plasma (ICP) etching.

The entire process detailed in this chapter was carried out at the Institute of Electronics, Microelectronics and Nanotechnology (IEMN-CNRS). The instruments used are an Oxford Plasmalab 80 plus RIE and an Oxford Plasmalab 100 ICP. Moreover, an Oxford Plasmalab 80 plus PECVD platform was used for SiO_2 deposition. All lithographic steps were performed with a RAITH EBPG5000Plus electron beam lithography tool. SEM pictures of the various lithographic steps were taken with a scanning electron microscope (ZEISS Ultra55 and Supra55vp).

2.1.2 GaN epitaxial technology

The main objective of this work is to realize GaN Schottky diodes which will be used in varactor mode in a frequency multiplier circuit for THz generation.
This will represent the next technological step, surpassing the current state of the art which is given by GaAs Schottky diode frequency multipliers

In this specific optic, one of the main challenges is the epitaxial quality of the material. GaAs underwent a long period of research, where intensive efforts have been undertaken to overcome the problems characteristics of its growth process, which resulted in the improvement of the techniques used for the epitaxial growth and bulk crystal growth (i.e. liquid encapsulated Czochralski and vertical gradient freeze) [90, 91]. As a consequence, GaAs epitaxy is a well-known technology, almost at par with silicon epitaxy (the most well known material growth process). GaN, however, did not benefit of enough popularity to justify a great effort in improving and optimizing its growth process until just recently [69].

Gallium nitride wafers can be grown by non-molten techniques, such as *metallorganic chemical vapor deposition* (MOCVD) and *halide vapor-phase epitaxy* (HVPE). HVPE has the highest growth rate, but the dislocation density is usually high ($\sim 10^9$cm^{-3}); MOCVD can yield wafers with the highest purity among the three cited methods, but with a significantly slow growth rate; the growth rate of MBE finds its place between the two other methods because the beam fluxes and the growth conditions can be precisely controlled [92] and thus can be used to produce super-lattice structures.

Any of this growth process is typically carried out on a foreign substrate, because bulk GaN crystal are not readily available, and their fabrication has an extremely high cost. Moreover, the overall low performances of homoepitaxial GaN films limit the use of this type of material. One of the primary criteria in the choice of a suitable substrate for GaN growth is the lattice constant mismatch. In practice, a great number of properties and parameters other than the lattice constants must be taken into consideration, such as the material's crystal structure, surface finish, composition, reactivity, chemical, thermal, and electrical properties, as these greatly influence the properties of the grown epitaxial layer [56]. Heteroepitaxy is not devoid of problems. Some of such problems are misfit and threading dislocations, whose densities on substrates such as sapphire and silicon carbide are typically between 10^8 and 10^{10} cm^{-2}, compared to densities of practically zero for silicon homoepitaxy, or 10^2 and 10^4 cm^{-2} for GaAs homoepitaxy [93]. Other common defects include inversion domain boundaries and stacking faults [94], which may create non-radiative recombination centers, introduce energy states into the band gap or reduce minority carrier lifetimes. It must be also noted that impurities diffuse more rapidly along threading dislocations thank in bulk material, causing non-uniform impurity distribution, which may degrade the performances of certain devices [95]. Moreover, owing to the high piezoelectric constants of GaN, threading dislocations may be surrounded by local strain which can cause submicronic scale variations in the electrical potential and electric field, with respect to that of the bulk material [96]. All of the aforementioned defects are typically non-uniform in their distribution along the epitaxial film, and it follows that the electrical properties of the devices made from such material may be non-uniform as well.

Maruskas and Tietjen's pioneering study of HVPE GaN epitaxy in 1969 employed sapphire (Al_2O_3) as substrate [97]. As of today, it remains the most commonly used substrate for GaN epitaxy. It is characterized by a large lattice constant mismatch with GaN ($\sim 15\%$) which leads to a high dislocation density ($10^{10}\,\mathrm{cm^{-2}}$) [93]. Because of these high defect densities, the charge carrier mobility is reduced, as well as the thermal conductivity [98] and the minority carrier lifetime [99, 100]; this brings to an eventual degradation of device performance. One well-known problem relative to heteroepitaxial growth of GaN on sapphire is the mismatch in thermal expansion coefficients: sapphire's coefficient is greater than that of GaN, therefore producing biaxial compressive stress as the system is cooled down from the deposition temperature. Thus, if the deposited film is very thick, this stress can cause cracks in both the film and the substrate [101]. Sapphire is poor in dissipating heat compared to other substrates, because of its low thermal conductivity (about $0.25\,\mathrm{W\,cm^{-1}\,K}$ at $100\,°\mathrm{C}$).

Silicon (Si) became a very attractive substrate for GaN-based devices because of its favorable physical properties, high quality and low cost. Being the basis of modern technology, silicon wafers have very low price and are available in large size due to its mature development and large-scale fabrication. Moreover, silicon is favorable for GaN epitaxial growth conditions due to its good thermal stability. However, by comparison with the two other most employed substrate (i.e. sapphire and silicon carbide), the GaN epitaxial layers grown on silicon substrate present the poorest quality due to the large lattice constant mismatch and the high thermal expansion coefficient difference. Nonetheless, the usage of Si as substrate for GaN epitaxial growth remains high and good progress has been made in reducing the defect density [56]. Both zincblende and wurtzite GaN has been grown on silicon by MBE [102, 103], MOCVD [104, 105] or HVPE [106].

Silicon carbide (frequently the 6H-SiC polytype) is, by far, the substrate for GaN epitaxy that offers several advantages with respect to sapphire, such as a smaller lattice constant mismatch (3.1%) and a higher thermal conductivity ($3.8\,\mathrm{W\,cm^{-1}\,K}$) [94]. Another advantage compared to other substrates is the possibility to envision simplified device architecture because, unlike sapphire for instance, SiC substrate can be made conductive, thus allowing the use of backside contacts. However, GaN growth directly on SiC is problematic, due to the poor wetting between these materials [107]. This is the reason why most of the manufacturers of GaN on SiC use a so-called "buffer layer", typically a layer of AlN or $Al_xGa_{1-x}N$; the downside of this approach is an increase in resistance between the device and the substrate.

Among the three substrates analyzed so far, SiC has the smallest lattice constant mismatch, but it is still sufficient to cause the formation of a large density of defects. Typically the surface roughness of SiC is an order of magnitude higher than that for sapphire [56], since it is very difficult to prepare smooth SiC surfaces. This roughness adds on the sources of defects for epitaxial GaN films. The screw dislocation density in SiC is 10^3–$10^4\,\mathrm{cm^{-2}}$ [108], and these defects can spread into the epitaxial layer, hence causing a degradation in device performance. At room temperature, furthermore, the films of GaN and the buffer layers of AlN are usually subjected to biaxial tension because the thermal expansion coefficient of SiC is lower compared to that of AlN or GaN. Lastly, the cost of SiC relatively high when compared to other substrate materials.

2.2 Process Outline

The fabrication process was developed and applied to several hetero-epitaxies of the three types: GaN on sapphire, GaN on silicon, and GaN on silicon carbide (6H polytype).

On each epitaxy, the same fabrication process was applied. Among these, one of each type was chosen to be presented in this work based on the performances of the fabricated Schottky diodes. A cross-view of the three epitaxial structure can be seen in Fig. 2.1. All epitaxies used in this project share a common structure: starting from the top, we have a n^- layer with low doping for that will be the semiconductor in the Schottky contact. Then we have a n^+ layer with high doping in order to achieve low contact resistance with the ohmic contact. After that we have a high resistive buffer layer, which will allow the isolation of the diode and in the end we have the substrate.

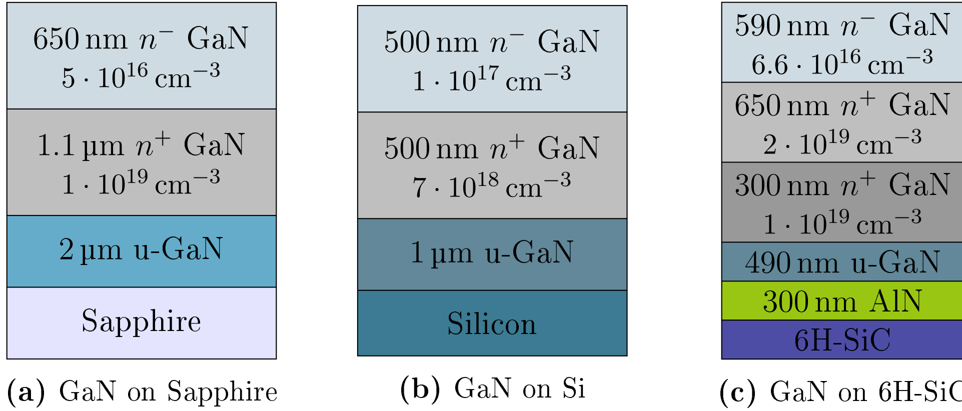

(a) GaN on Sapphire **(b)** GaN on Si **(c)** GaN on 6H-SiC

Figure 2.1: Schematic cross-view of the three epitaxies used

A simplified overview of the fabrication process flow employed in this work for all the epitaxies can be seen in Fig. 2.2. Each step will be explained in detail in the next sections.

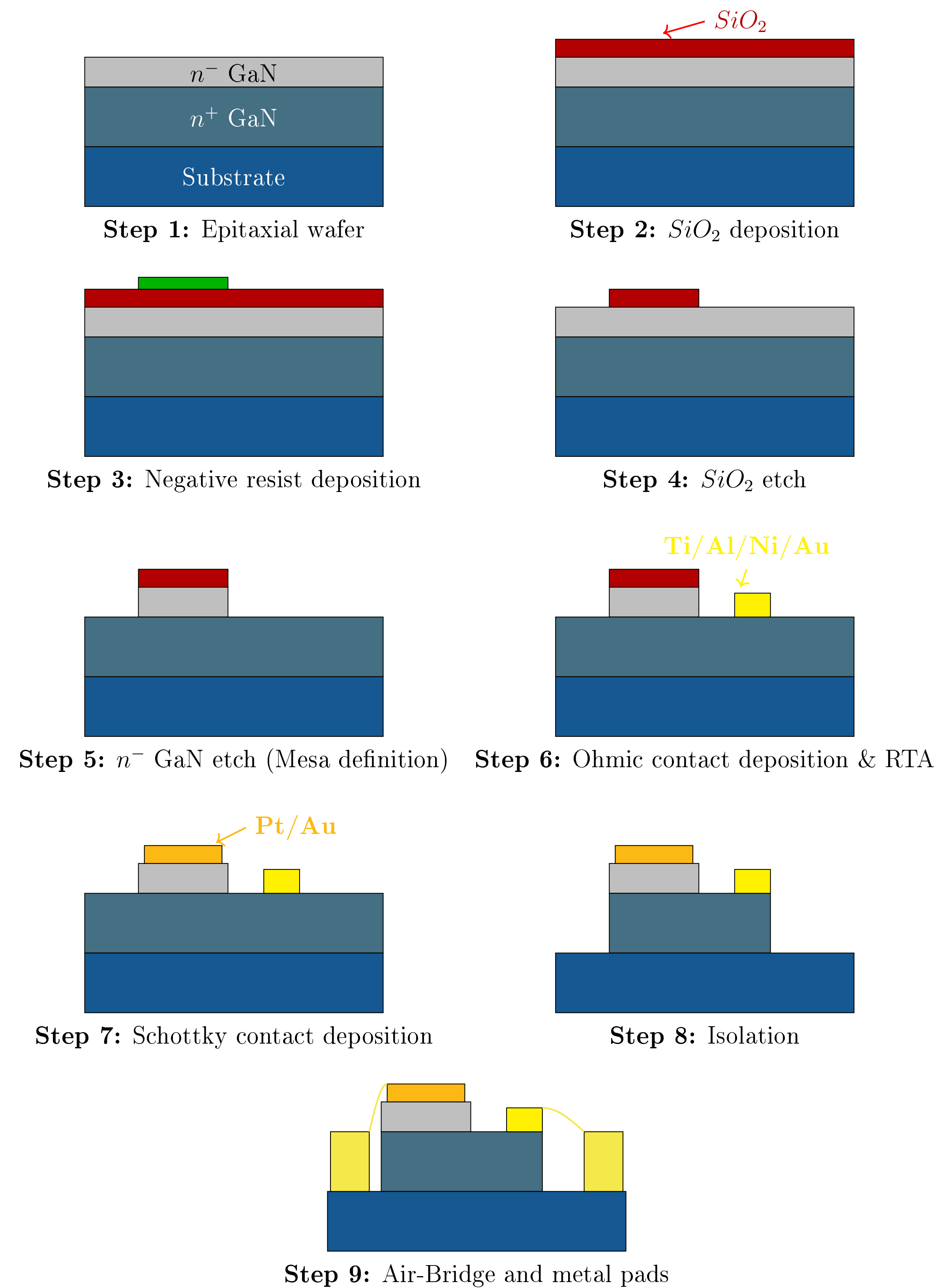

Figure 2.2: Process flow of the fabrication of Schottky diodes with air-bridge technology used in this work

2.2.1 Mesa Definition

First of all, the sample is cleaned and degreased extensively. Then, a SiO_2 layer of 250 nm is deposited through Plasma-Enhanced Chemical Vapor Deposition (PECVD). A negative resist (AZ NLOF 2020) is spincoated onto the sample and then exposed and developed (Fig. 2.3).

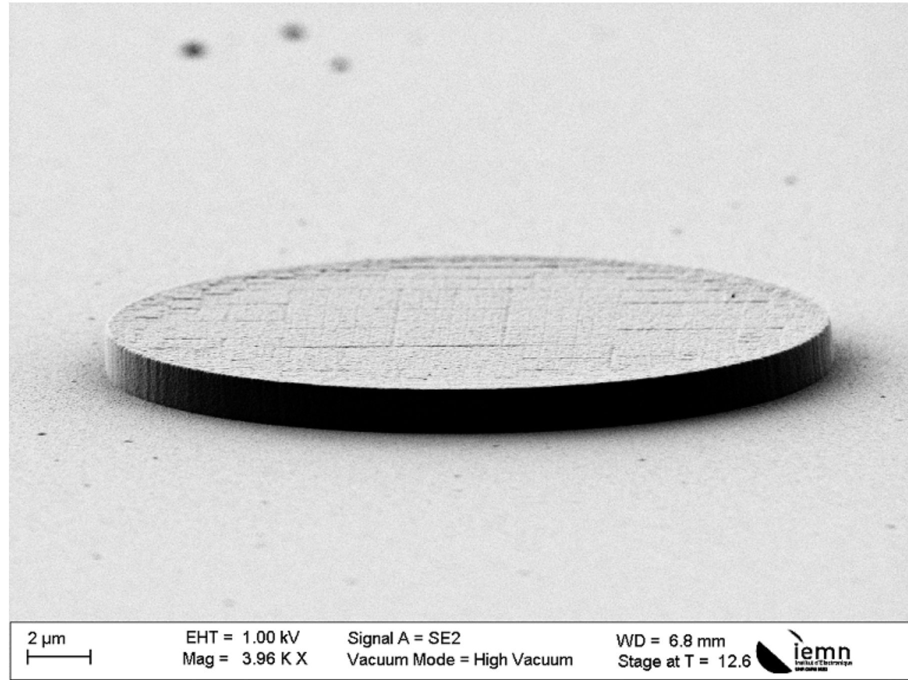

Figure 2.3: NLOF development results

The negative resist pattern is then transferred to the SiO_2 layer through reactive ion etching (RIE) using SF_6 plasma (Fig 2.4a). The remaining resist is subsequently cleaned by O_2 plasma (Fig 2.4b).

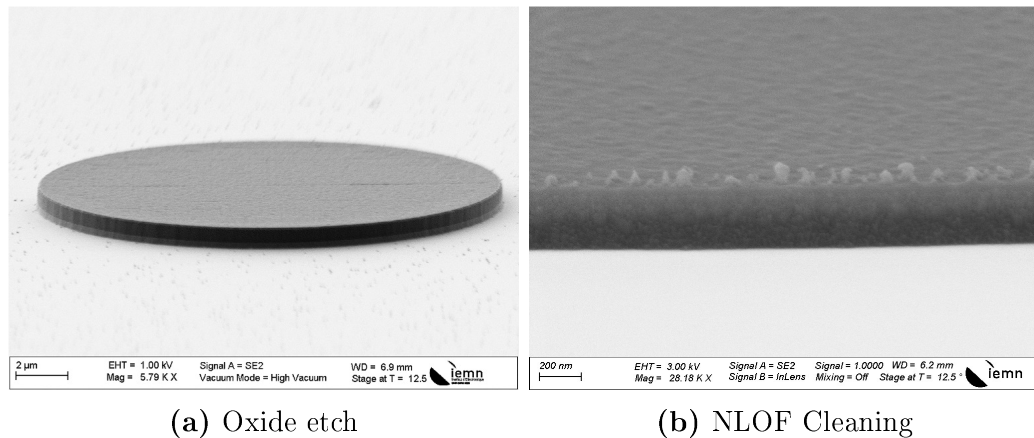

(a) Oxide etch **(b)** NLOF Cleaning

Figure 2.4: SEM pictures of RIE results. In Fig. 2.4a, the NLOF mask was transferred to the SiO_2. In Fig. 2.4b, the remaining NLOF was removed, and in this zoom of the profile it is possible to view some resist residue on the border

The negative resist mask is effectively transferred to the silicon oxide layer. The etching of the n^- GaN layer is achieved through ICP dry etch. ICP systems have the advantage of higher plasma density as compared to RIE systems (2 to 4 orders of magnitude higher), consequently improving, in the case of GaN and other III-group nitrides, the III-N bond breaking efficiency and the sputter desorption of etch sub-products formed on the surface [58]. Moreover, plasma-induced damage on the material surface is more easily controlled thanks to the effective decoupling of ion energy and ion density.

A Cl_2/Ar gas mixture is employed, yielding anisotropic etch of the n^- GaN layer, down to the n^+ layer, where the Ohmic contact will be deposited in the immediately successive process step. The results of the n^- GaN etch can be seen in Fig 2.5.

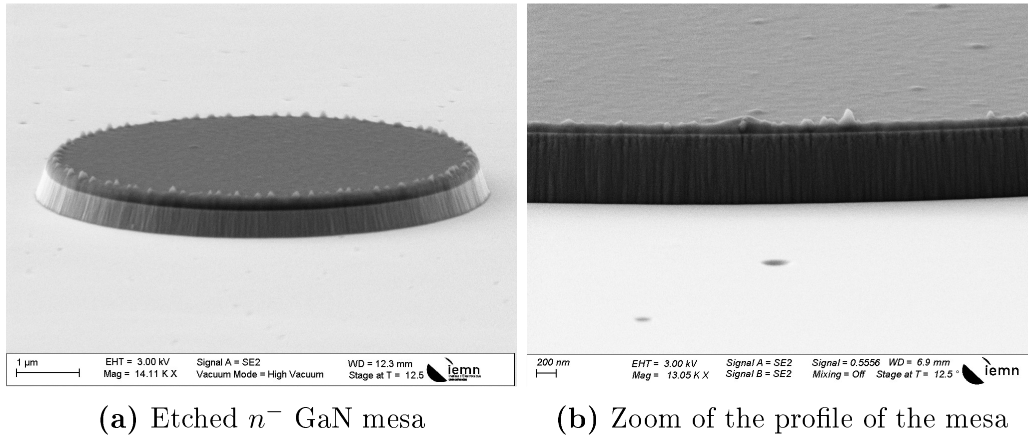

(a) Etched n^- GaN mesa **(b)** Zoom of the profile of the mesa

Figure 2.5: n^- GaN mesa after dry etching

2.2.2 Ohmic Contact

As stated before, the requirement for good ohmic contacts is the lowest possible contact resistance. Typically, the two types of ohmic contacts considered for Schottky diodes are tunnel contacts and thermionic contact, respectively contacts where the dominant carrier transport is tunneling and thermionic emission. However, it is widely believed that for the formation of optimal ohmic contacts to n-GaN, a special transport mechanism is needed, e.g., tunneling. The tunneling is made possible only if n-GaN is heavily doped with a significant conduction band bending near the metal-semiconductor interface. This in turn leads to the semiconductor region at the interface to become very thin allowing an electron flow via tunneling. The result is a significantly low resistivity of the contact. From this brief theoretical analysis, it becomes clear that by using moderately doped semiconductors the objective of achieving low contact resistivity becomes a full-fledged technological challenge.

The majority of ohmic contacts to n-GaN developed until now include at least two low work-function metals: Al and Ti. Among the contacts found in the literature are Al-only, Ti-only, a Ti/Al bilayer and multilayers such as Ti/Al/Ni/Au [109, 110], Ti/Al/Ti/Au [111], Ti/Al/Pd/Au [112], Ti/Al/Pt/Au [113, 114], Ti/Al/Mo/Au [115] and V/Al/Pt/Au [116].

Ohmic contacts realized exclusively with just Ti or just Al are not reliable for high-power and high temperature applications because of their propensity for oxidation. These contacts are not really controllable and reproducible for high-temperature operation [117]. Moreover, the low melting point of Al (600 °C) can be found problematic for thermal stability of contacts such as Al-only or Ti/Al bilayer.

The first layer of a good ohmic contact must have preferably a small work function. This serve a "barrier" purpose because it avoids diffusion onto the n-GaN surface of metals that have larger work functions. Titanium is a very highly reactive refractory metal. It reacts with the nitrogen atoms on the n-GaN surface, yielding a semiconductor surface which is highly doped, due to the vacancies of nitrogen now present that act as n-type dopant [118] with bandgap energy levels very close to the conduction band edge of n-GaN.

The next layer should ideally enhance solid phase chemical reactions between the nitrogen atoms and the metal atoms and, at the same time, produce thin, low work function and robust alloys. Al is a good choice as long as it does not create, upon alloying, a thick, wide bandgap compound, or out-diffuse to the contacts surface to form highly insulating oxides, causing significant deterioration of contact performances [119].

The propensity for oxidation of this 2-layer system may be solved with a cap layer composed of refractory and/or transition metals. Moreover, by accurately choosing the metals, the free energy of the metal system can be reduced, forming more intermetallic alloys, yielding a more stable metal system. A Au layer protects the Ti/Al system from oxidation and a intermediate layer (made of one of the following metals: Ti, Ni, Pd, Pt) prevents diffusion of Au to the Al layer, as well as out-diffusion of Al.

In general, the decision of the multilayer metals does not establish right away chemical equilibrium with the n-GaN. Thus, rapid thermal annealing (RTA) is employed to achieve the solid-state interfacial reaction (metal inter-diffusion). The composition and resistance of final product will depend on the RTA temperature, RTA time, the rate of increment of the temperature between room temperature and annealing temperature, and the relative thickness of the metals employed.

The surface treatment of n-GaN prior to ohmic contact metallization is of crucial importance. Typically carried out by plasma etching (RIE) or wet etching, has several beneficial functions: removing the surface oxide and/or hydroxide layers (if present), creating N-terminated GaN surface, yields a rough GaN surface, essential for strong metal adhesion, it creates a metal-semiconductor interface with a barrier height lower than the Schottky barrier height and it produces high concentration of nitrogen vacancies in the GaN subsurface.

A Ti (25 nm) / Al (200 nm) / Ni (40 nm) / Au (100 nm) multilayer is used in this process. Prior to metallization, the interested surface was treated with a buffered HF solution and with plasma etching. Then rapid thermal annealing was performed at 850 °C for 30 s in a N_2 ambient. An example of the resulting contact can be seen in Fig 2.6.

In order to evaluate the parameters of the fabricated Ohmic contacts, the Transfer Length Method was used. With this, the contact resistance (R_c, Ω·mm), the specific

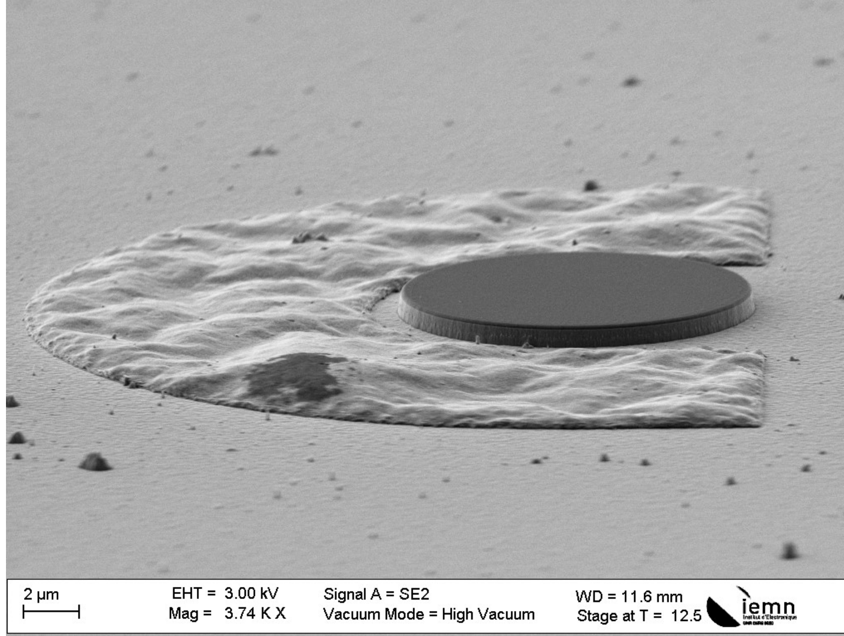

Figure 2.6: Example of Ti/Al/Ni/Au Ohmic contact after RTA at 850 °C for 30 s

contact resistance (ρ_c, $\Omega{\cdot}\text{cm}^2$) and the sheet resistance of the semiconductor (R_{sh}, $\Omega/\square$) can be extracted.
The resistance between two Ohmic contacts of width W formed on a semiconductor layer, separeted by a space d_i, can be written as

$$R_{m,i} = \frac{R_{sh} d_i}{W} + 2R_c \tag{2.1}$$

where R_c and R_{sh} are correlated through ρ_c

$$R_c = \frac{\sqrt{R_{sh}\rho_c}}{W} \coth\left(\frac{l}{l_t}\right) \tag{2.2}$$

l_t is the transfer length which corresponds to the distance where most of the current transfers from the semiconductor layer to the metal and vice-versa. Since $l \gg l_t$, $\coth(l/l_t) = 1$, thus l_t is given by

$$l_t = \sqrt{\frac{\rho_c}{R_{sh}}} \tag{2.3}$$

A series of Ohmic contacts with different spacings d_i (Fig 2.7) forms a set of resistances. Measuring a large number of resistances allows to minimize the measurement uncertainty. The resulting line obtained by fitting the data points will yield R_{sh}/W as its slope, $2R_c$ as the y-axis intercept and $2l_t$ as the x-axis intercept.

The TLM method can be applied also in the case of circular contacts (Fig. 2.8). Compared to the rectangular contacts, the circular TLM pattern has the advantage of restricting the current flow vertical to the contact edge and, therefore, avoiding

the current crowding problem. Moreover, this method does not require mesa etching (as opposed to the rectangular pattern).

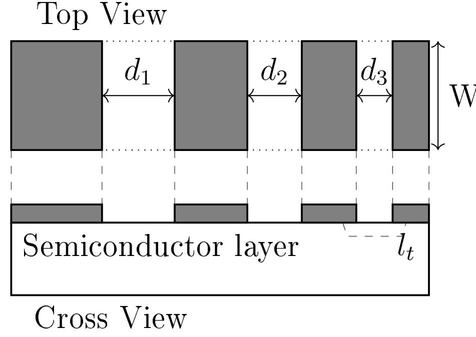

Figure 2.7: TLM pattern structure

The resistance between two Ohmic contacts of circular TLM patterns depends on the space d_i as follows:

$$R_{m,i} = \frac{R_{sh} 2\pi R_{in}}{d_i + 2l_t} C \tag{2.4}$$

where C is a correction factor of the circular geometry and is given by

$$C = \frac{R_{in}}{d_i} \ln\left(1 + \frac{d_i}{R_{in}}\right) \tag{2.5}$$

With this correction factor, a fitted line from measured $R_{m,i}(d_i)$ provides, as in the rectangular TLM pattern, $2R_C$ as the intercept on the y-axis, $2l_t$ as the intercept on the x-axis, and $R_{sh}/2\pi R_{in}$ as the slope.

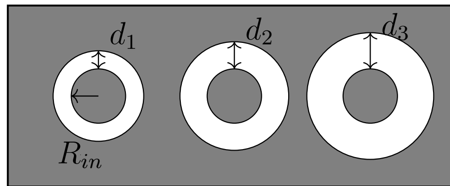

Figure 2.8: Circular TLM pattern structure

Fig. 2.9 shows results obtained from 4-points measurements on circular TLM patterns for the Ohmic contact fabricated on the GaN on sapphire sample. The four values of ρ_c presented in Fig. 2.9 go from $4.7 \cdot 10^{-6}\,\Omega\,\text{cm}^2$ down to $9.37 \cdot 10^{-6}\,\Omega\,\text{cm}^2$. The extracted resistivity from the other 2 example sets do not deviate substantially but results in a different value. This happens because the TLM method is sensitive to needle contact resistance. In order to assure the linear dependence of resistance on gap distance, ohmic contacts with very large area must be employed so that the resistance between two adjacent contacts can be much smaller. The complete results for the sets presentend in the example can be visioned in Table 2.1.

In Table 2.2 , there are typical results for the specific contact resistance of the ohmic contact fabricated on the three epitaxies used in this work, along with some values of different ohmic contacts on n-GaN present in the literature.

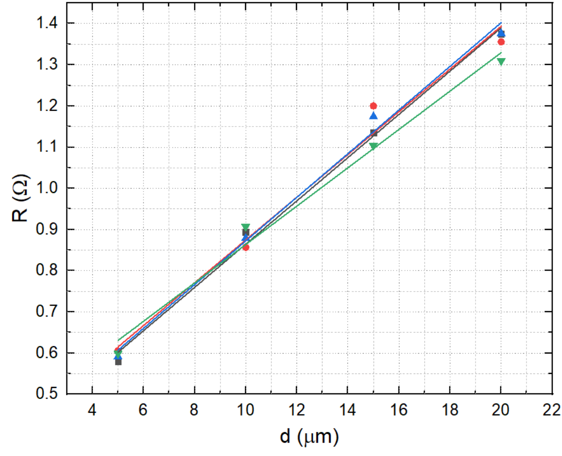

Figure 2.9: Results of circular TLM measurements

	R_C (Ω mm)	R_{sh} ($\Omega/\square$)	l_t (µm)	ρ_c (Ω cm^2)
1	0.174	51.8	3.364	$5.86 \cdot 10^{-6}$
2	0.160	54.7	2.932	$4.7 \cdot 10^{-6}$
3	0.165	54.1	3.045	$5.01 \cdot 10^{-6}$
4	0.206	45.4	4.543	$9.37 \cdot 10^{-6}$

Table 2.1: TLM results of Fig. 2.9

Metal	**Thickness** (nm)	**RTA T** (°C)	**Time** (s)	ρ_c (Ω·cm^2)	**Ref.**
Ti/Al/Ni/Au	25/200/40/100	850	30	$4.3 \cdot 10^{-6}$	Sapphire
Ti/Al/Ni/Au	25/200/40/100	850	30	$9.11 \cdot 10^{-6}$	Si
Ti/Al/Ni/Au	25/200/40/100	850	30	$4 \cdot 10^{-7}$	SiC
Ti/Al	300/700	600	NA	NA	[120]
Ti/Al	20/100	900	30	$8 \cdot 10^{-6}$	[121]
Ti/Al	NA	600	60	$5 - 8 \cdot 10^{-5}$	[122]
Ti/Al/Re/Au	15/60/20/50	750	60	$1.3 \cdot 10^{-6}$	[123]
Ti/Al/Ti/Au	20/100/40/100	750 − 900	60	$3 \cdot 10^{-5}$	[124]

Table 2.2: Specific contact resistance of different Ohmic contacts on n-GaN in the literature. The underlined values refers to Ohmic contacts of this work

2.2.3 Schottky Contact

The fabrication of Schottky contacts is the most critical part of the process. The theoretical Schottky-Mott barrier height is defined as:

$$q\phi_{SM} = q\phi_M - \chi_S \tag{2.6}$$

where q is the elementary charge and χ_S is the electron affinity of the semiconductor, which, in the case of GaN, is 4.11 eV.
The ionic component of bond in nitrides is quite substantial, and thus the Fermi level at the nitride surface and metal-nitride interface is believed to be unpinned [117]. Given this considerations, the barrier height should only depend on the work function of the metal [125, 126]. Therefore, in order to form a proper Schottky contact on GaN, the metal of choice must have a high work function ϕ_M. Frequently used metals include Ni ($\phi_M = 5.15$ eV), Pt ($\phi_M = 5.65$ eV), Pd($\phi_M = 5.12$ eV) and Au ($\phi_M = 5.1$ eV). However, experimental results (Table 2.3) hardly corroborate this argument.

This is because the barrier height, and, more generally, the intimate metal-semiconductor interface, is often influenced by non-idealities. There are numerous transport mechanisms, such as thermionic field emission, tunneling, generation-recombination (non-radiative recombination current) that are responsible for high reverse leakage current. All of the aforementioned mechanisms depend on the state of the metal-semiconductor interface, i.e., from the presence of traps, interface states, dislocation defects and are also sensitive to heavy doping. As stated before,

Metal	**Thickness** (nm)	**Barrier Height** (eV)	**Ideality factor**	**Ref.**
Pt/Au	80/120	$0.79 - 0.96$	$1.80 - 1.16$	[127]
Pt/Au	30/100	1.05	1.01	[128]
Pt/Ti/Au	80/120	$0.79 - 0.96$	$1.80 - 1.16$	[128]
Pd/Au	30/30	$0.23 - 0.97$	$3.5 - 1.9$	[129]
Pd/Mo	30/30	0.78	1.4	[130]
Rh/Au	25/25	$0.62 - 0.84$	$1.12 - 1.73$	[131]
Ni/Au	10/330	0.88	1.18	[132]
Ni/Pt/Au	10/30/300	1.09	1.12	[132]
Ni/Pd/Au	10/30/300	0.78	1.14	[132]
Ni/Mo/Au	10/30/300	0.54	1.02	[132]
Ag	150	0.7	1.57	[133]
Ni	$100 - 150$	1.15	1.17	[134]

Table 2.3: Short survey of some of the Schottky contact on n-GaN present in the literature

the strong ionic component of bonds in GaN should suggests an unpinned Fermi level at the interface. However, GaN surface is characterized by active chemisorption, which promotes the formation of surface native oxides and hydroxides [135, 136], which alter the barrier height and increase leakage at high reverse bias. Therefore, one of the main issues in GaN Schottky diode technology is the comprehension of GaN surface and the removal of unwanted elements from it prior to Schottky contact deposition, by means of wet chemical etching or even dry etching.

A Pt (50 nm) / Au (400 nm) was deposited through e-beam evaporation, to serve as Schottky contact for the diodes fabricated with this process. Before metallization, the samples were treated with a BOE solution to remove the remaining SiO_2 layer and uncover the n^- GaN surface. In the evaporator chamber, the samples were also treated with argon etching. The Schottky contact fabrication was then completed with standard lift-off technique. The resulting contact can be seen in Fig 2.10 and, in a more detailed profile look, in Fig. 2.11.

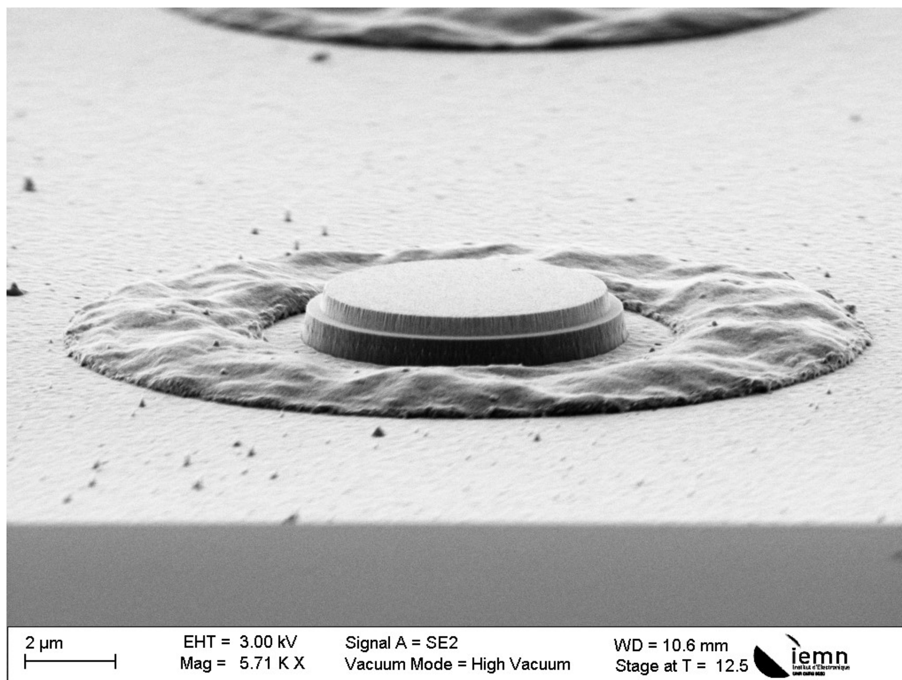

Figure 2.10: Schottky contact

Different surface wet chemical treatments were tested and studied on all three epitaxies used in this work, as well as different annealing temperatures for the Schottky contact. All of this will be discussed in Section 2.3 and Section 2.4

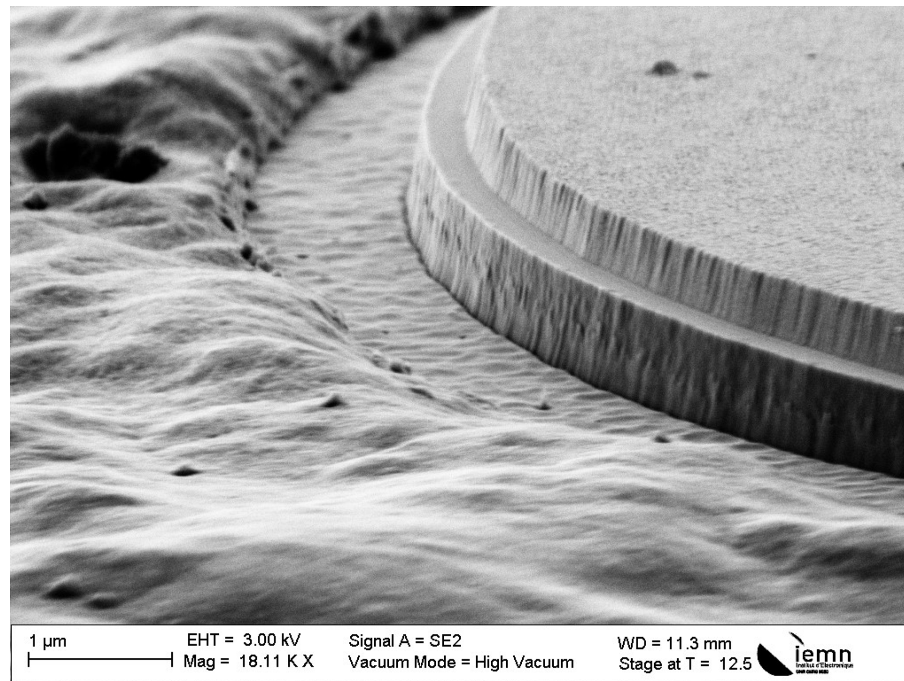

Figure 2.11: Schottky diode mesa

2.2.4 Isolation

The mask used in this work allows the fabrication of two families of diodes: the first is composed of diodes with diameters ranging from 1400 µm down to 28 µm, used for first-level electrical characterization and physical optimization; the second is composed of diodes with diameter ranging from 40 µm down to 0.6 µm, in different configurations (single, series, anti-parallel series, etc.). These smaller diodes are contacted by means of an air-bridge. Air-bridges are of notable importance for high-frequency characterization, due to the decreased presence of parasitic components.

The diodes are isolated by means of Cl_2/Ar based ICP dry etching, using a bilayer of negative resist as mask. One of the motivation for using a resist bilayer is the protection of the device fabricated up to this point in the process, leaving the rest of the surface of the sample exposed for dry etching. The n^+ GaN is etched down to the resistive buffer. The sample before isolation etching can be seen in Fig 2.12a, while the sample after etching can be seen in Fig 2.12b. Fig 2.12c offers a more detailed look of the etch profile: starting from the top there is the bilayer of negative resist, with the top layer being bigger then the bottom layer in order to provide the best vertical profile possible for the isolation mesa; then there is (in light gray) the n^+ GaN layer and, in dark gray, the resistive buffer layer.

The use of dry etch involves the risk of damaging the surface, although any eventual damage of this kind and at this step of the process is inconsequential, because the Schottky diode was protected during the etch process by the resist bilayer, and because any kind of surface damage induced by the dry etch for isolation is transferred to the RF resistive buffer layer (and not on an active layer).

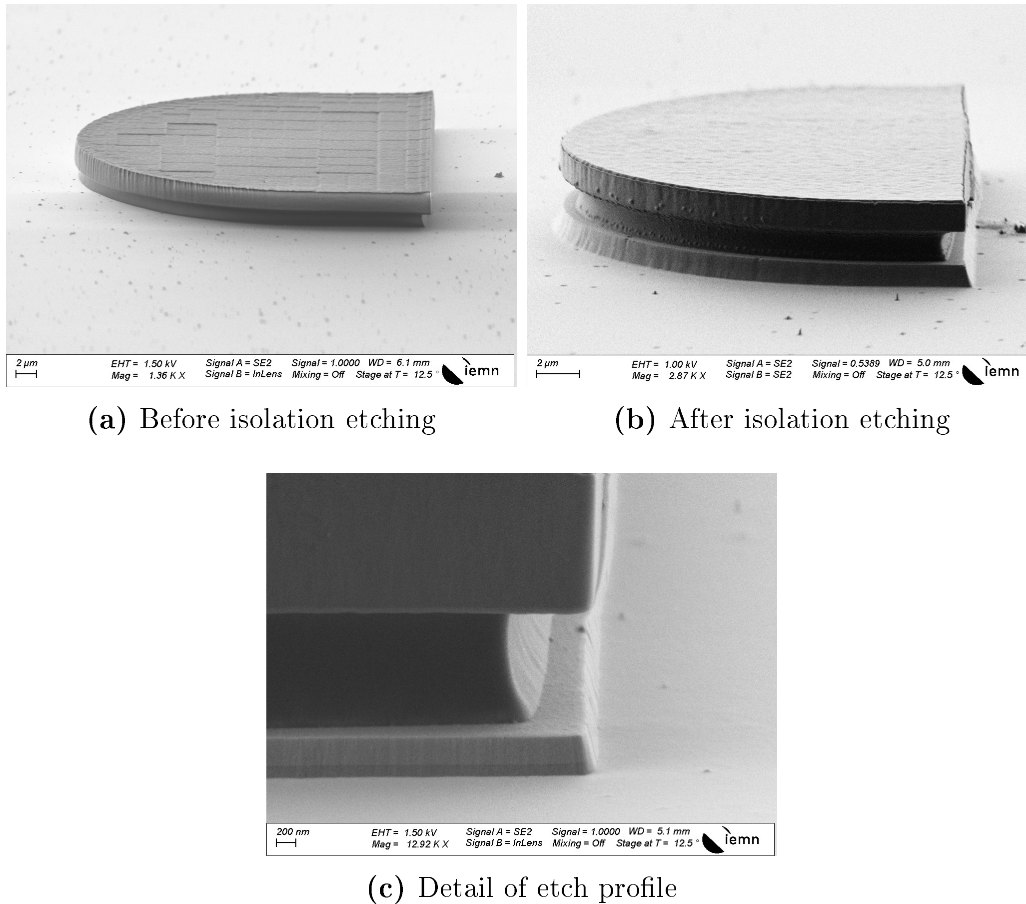

(a) Before isolation etching **(b)** After isolation etching

(c) Detail of etch profile

Figure 2.12: SEM pictures of ICP dry etching for isolation

2.2.5 Air-Bridge

The last two lithographic steps regard the realization of the air-bridge structure. First, vias for the metal pads and the bridge contacts to Schottky and Ohmic contacts are opened with positive resist. Then, a thermal treatment is operated to enact a "reflow" of the resist. The objective is to smooth the edge of the resist pattern around the diode structure (Fig 2.13). This is a fundamental step, because it will act as a physical sustain for the metal bridge finger. Keeping in mind that the type of thermal treatment is closely related to the type of resist chosen, particular attention must be dedicated to avoid two typical problems: a single-step, fast treatment will cover the Schottky contact surface, thus impeding the connection with the bridge finger (as opposed to the outcome of a slower treatment, visible in Fig. 2.13b); lastly, depending on the thermal process chosen, the edge termination of the reflowed resist toward the metal pad can be cause of trouble. If the angle is too sharp, a crack will form between the bridge finger and the metal pad immediately after lift-off, causing the structure to break.

In the last lithographic step, a bilayer of positive resist is used to define the bridge structure. Given that this step is done directly after the reflow step, some considerations must be made. The bilayer is a standard choice for metal deposition and subsequent lift-off. However, the two resists must be chosen by keeping in mind that their exposure and their development must leave the resist used for the reflow step intact, or, at least, in the best conditions possible. Thus, the resists were chosen

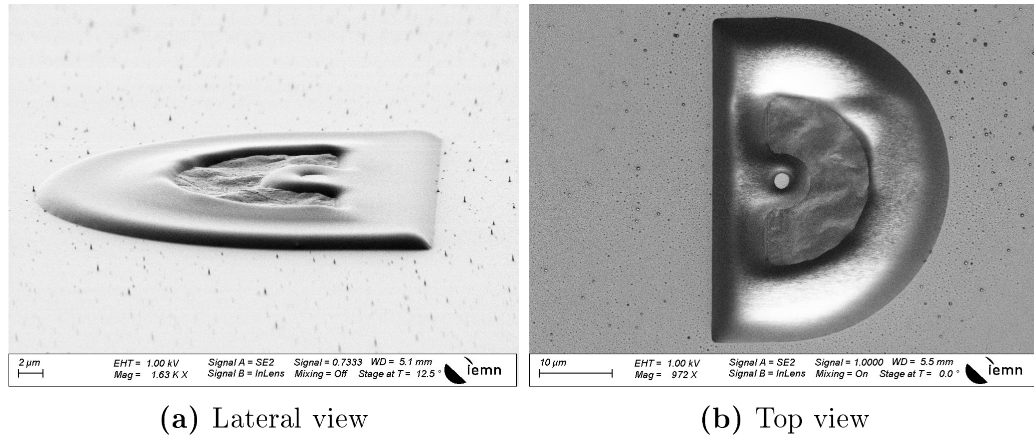

(a) Lateral view **(b)** Top view

Figure 2.13: Resist reflow

on the basis of their sensitivity with respect to the dose used for exposure and the sensitivity of their developers. A typical result after the final development can be seen in Fig. 2.14.

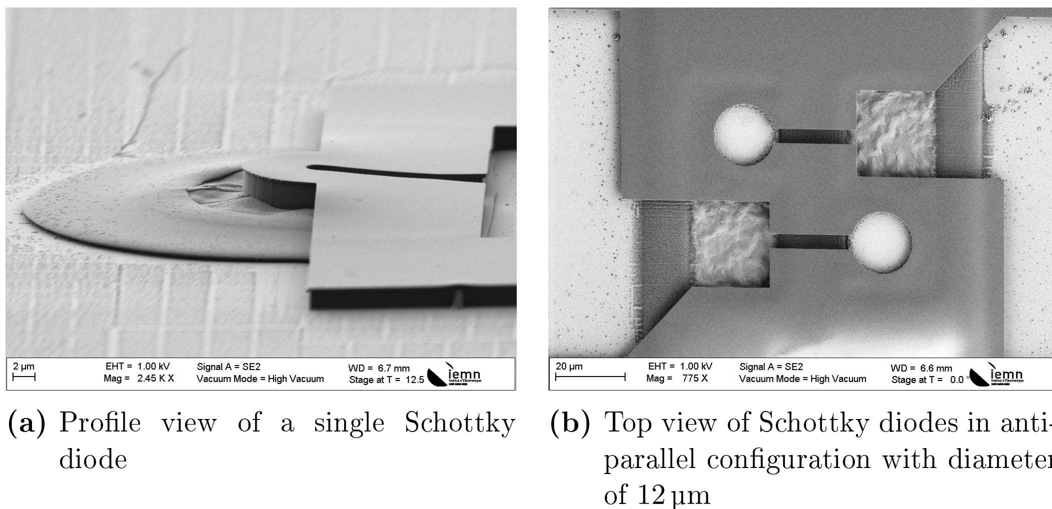

(a) Profile view of a single Schottky diode

(b) Top view of Schottky diodes in anti-parallel configuration with diameter of 12 µm

Figure 2.14: SEM images of Schottky diodes after the development of the final lithographic step, just before air-bridge metallization

Finally, a Ti (200 nm) / Au (600 nm) metal contact is evaporated onto the sample. The process is then completed with standard lift-off technique. Some examples of the final results are illustrated in Fig 2.15 and in Fig 2.16.

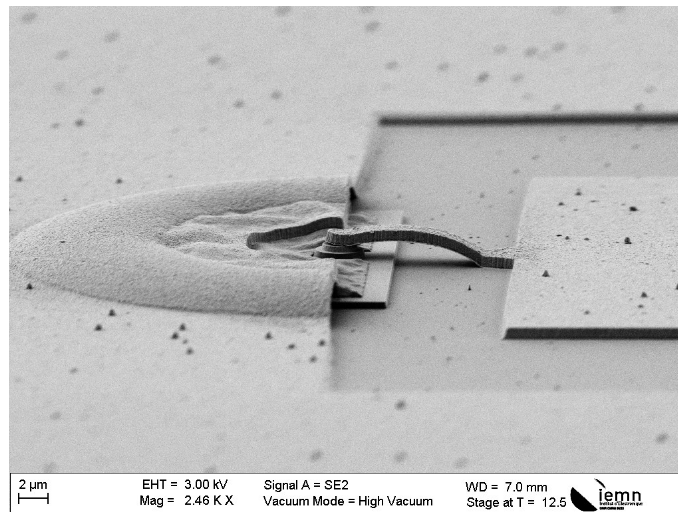

(a) GaN Schottky diode with diameter of 2 µm

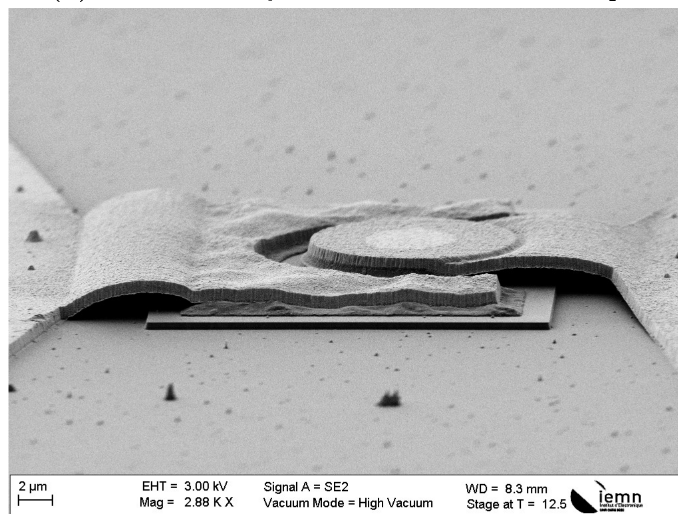

(b) GaN Schottky diode with diameter of 8 µm

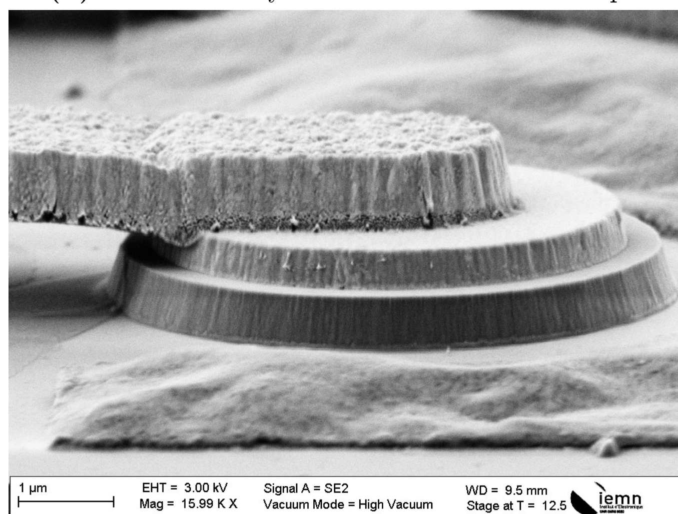

(c) Detailed look of a Schottky contact

Figure 2.15: Profile SEM pictures of Schottky diodes with air-bridge

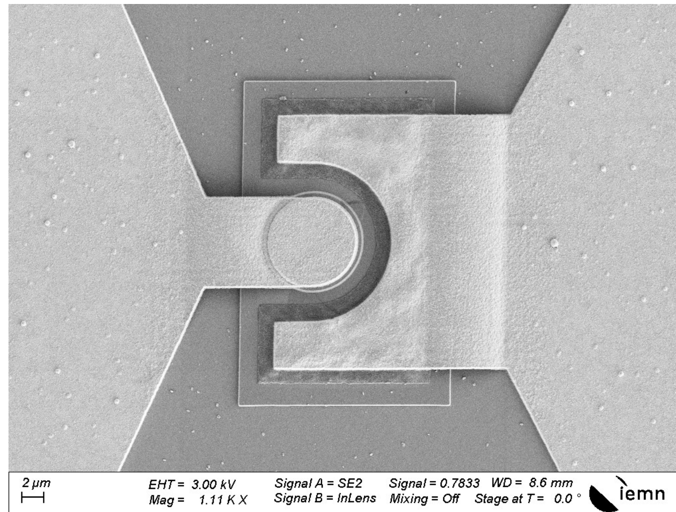

(a) GaN Schottky diode with diameter of 8 µm

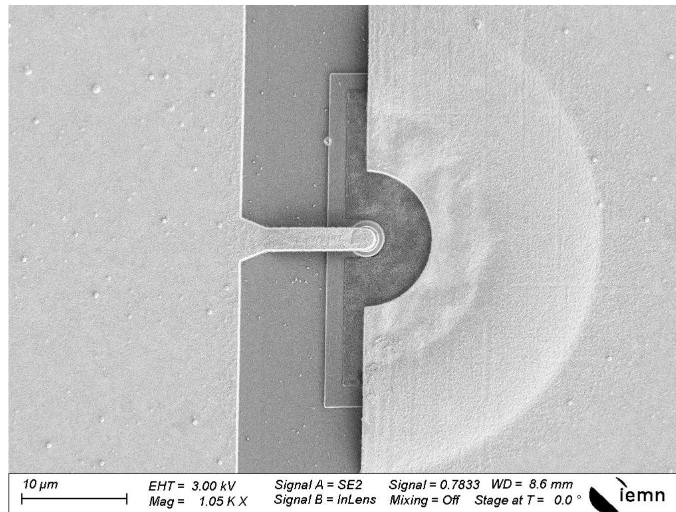

(b) GaN Schottky diode with diameter of 2.4 µm

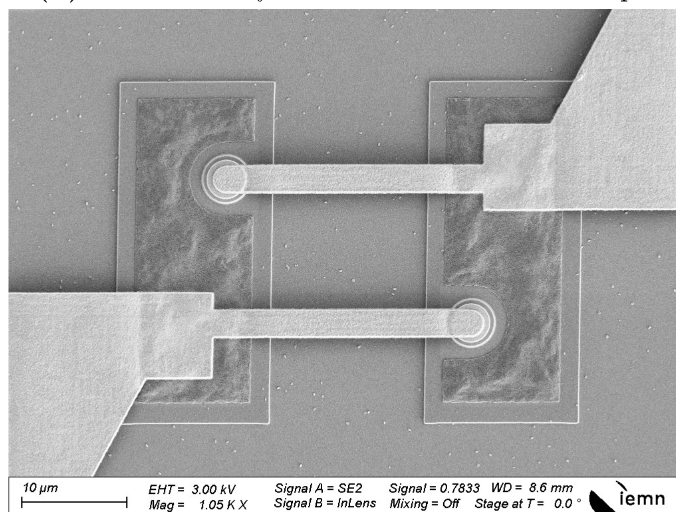

(c) GaN Schottky diodes in anti-parallel configuration with diameter of 3.6 µm

Figure 2.16: Top view SEM pictures of Schottky diodes with air-bridge

In this work, Schottky diodes with air-bridge structure were fabricated with the process just described on GaN on Si and GaN on SiC. The air-bridge fabrication is a standard technique used in III-V devices fabrications. However, given the peculiar differences of the two substrates used in this work, it was necessary to overcome some challenges.

GaN on Si

For Schottky diodes fabricated on GaN on Si, the technological challenge regarded the exposure and development of the resist bilayer used in the last lithographic step. The two resists were chosen with respect to the selectivity of their developers toward the positive resist used for the reflow step. However, in the case of this substrate, this sensitivity was completely "lost". In fact, after the development of the last resist, it was found out that the reflow resist underwent an ulterior develop, causing cracks or complete develop, as it can be seen in Fig. 2.17.

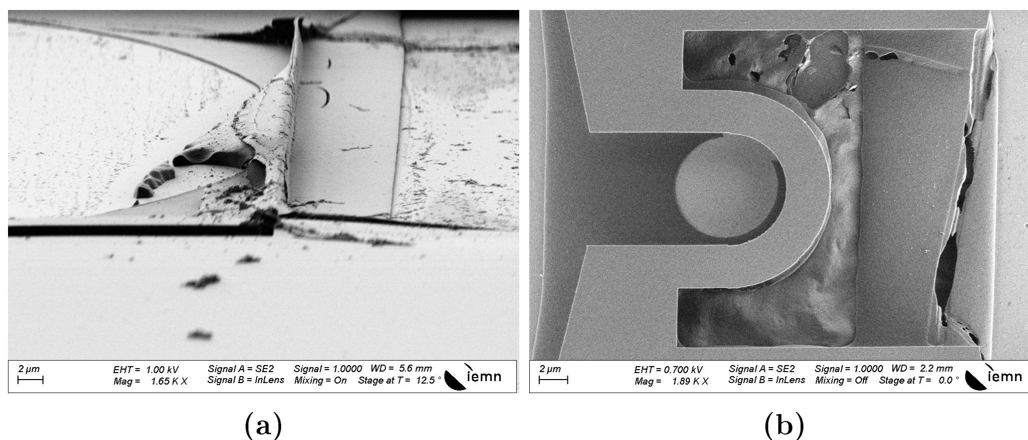

Figure 2.17: Over-development of the reflow resist on GaN on Si process. In the profile view shown in **(a)**, the reflow resist got completely develop by the secondary exposure, while in the top view shown in **(b)** the reflow resist presented severe cracks after the develop of the last lithographic step

The cause of this behavior might be attributed to the silicon substrate, in that it probably caused a reflection of secondary electrons, during the exposure of the last lithographic step, that caused an ulterior exposure of the reflow resist. This problem was solved by using a different resist for the reflow step.

GaN on SiC

The SiC substrate used in this work had the peculiarity of being resistive. As such, a 5 nm layer of *Ge* was deposited at each lithographic step of the process just before exposure to reduce misalignment caused by charging effects during the exposure. This layer was then removed each time before resist develop. The only exception to this procedure was the last lithographic step, in that the deposition and subsequent removal of the *Ge* layer caused stress in the resists, resulting in severe cracks after the develop of the first layer.

The sensitivity between the reflow resist and the two resists used in the final bilayer was unchanged. However, the final yield of the air-bridge was considerably smaller compared to the diodes fabricated on GaN on Si. Because of the higher height of the isolation mesa (compared to GaN on Si substrate), the angle between the termination of the bridge finger and the metal pad was too sharp, causing the structure to crack, as shown in Fig. 2.18a. This resulting structural weakness caused, in some cases, the air-bridge finger to be bent after lift-off, thus impeding connection with the Schottky contact (Fig. 2.18b).

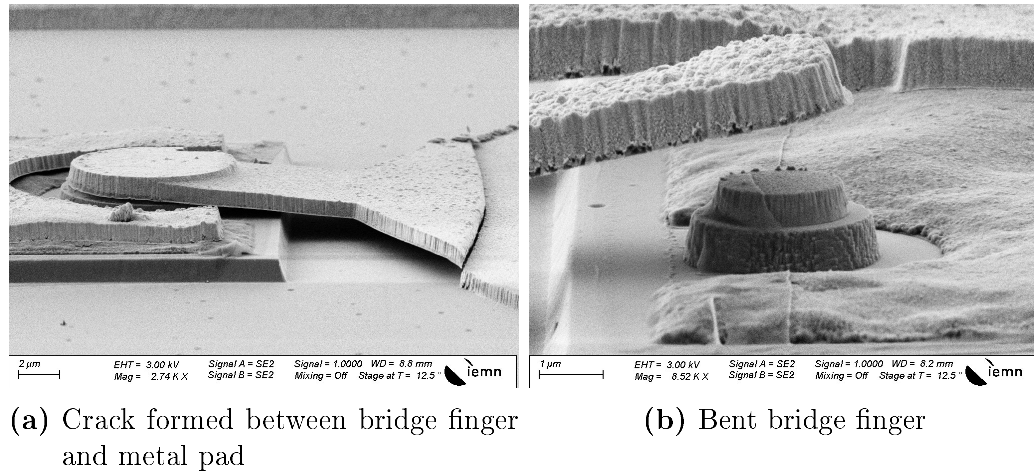

(a) Crack formed between bridge finger and metal pad

(b) Bent bridge finger

Figure 2.18: Technological problems encountered during the fabrication of Schottky diodes on GaN on SiC

The problem just described can be solved by optimizing the reflow resist to the epitaxial structure.

2.3 Surface Chemical Treatments

The semiconductor-metal interface of GaN Schottky diodes is influenced by non-idealities that hinder the electrical performances of the final device. Surface treatment prior to Schottky contact metallization can have a positive influence on epitaxial defects, chemical contaminants, metal contact resistance and stability and overall quality of the device.

One of the challenges that are faced in GaN technology is that there is no standard method for surface preparation before metallization. These methods differ from laboratory to laboratory. Moreover, one other discriminant is the fact that the epitaxial and heteroepitaxial GaN used in each work present in the literature are characterized by differences in growth method, morphology, thickness and doping, which can bring to different results when applying the same surface cleaning method.

Wet and dry etch methods are widely used in surface preparation in order to remove contaminants on GaN prior to metallization. Dry etch is known for introducing damage to the surface, which may bring to a deterioration of the electrical characteristics of the final product [137].

In general, in semiconductor technology, a typical surface cleaning procedure can be divided in three main steps [138]:

- degrease to remove gross contaminants
- removal of particle contaminations
- removal of surface oxides in order to provide an atomically clean surface

In practice, understanding the correspondence between surface composition and structure and the successful application of the cleaning step in the process can be challenging. The definition of "clean" differs depending on the epitaxy (method of growth, substrate, etc.) and may differ depending on the required condition of "success", in the framework of the process in which this step is employed.

Smith et al. [138] used AES to compare HCl and HF-based solutions in methanol and water, to remove contaminants on the GaN surfaces, with the additional use of UV/O_3 treatment. A contamination-free surface was obtained by thermal desorption at temperatures up to 800 °C. From their results, comparing $HCl : DI$ and $HF : DI$, it was found that HF-based solution was more effective in removing C and O contaminants on the surfaces; moreover, after treatment with HCl-based solution they observed the presence of Cl on the surface and UV/O_3 increased the surface oxide while decreasing C contaminants.

King et al [139] showed that UV/O_3 treatment was found to be effective in removing C and simultaneously increasing O on the surface. It was further observed that increasing ozone concentration further reduced C on the surface though it was not completely removed. Successive observations of the UV/O_3 exposed surface showed an increase in the rate of oxidation of GaN surface. The use of HCl, NH_4OH and HF solutions were found to remove the oxides effectively. The lowest C/N ratio was produced by a 1:1 $HCl : DI$ solution, with the only disadvantage of Cl addition to the surface. HF-based cleaning solutions were found to increase the O/N ratio with

no detection of F on the surface. Thermal desorption of the surface at 700–800 °C yielded stoichiometric GaN surface.

Lee et al. [140] investigated several methods of cleaning GaN that included different wet chemical procedures, as well as in situ cleaning at elevated temperatures. The wet chemical methods consisted of acetone, methanol, HF or HCl and UV/O_3 treatments. Thermal cleaning was done in N_2 and H_2/N_2 plasma and it was found effective for removing O contaminants. It was observed that UV/O_3 treatment increased O contamination while decreasing C contamination. Treatment in HCl further reduced the O concentration and the C content to almost the same level as of the as-grown sample, but also left Cl contamination on the surface.

Diale et al. [141] tested a HCl treatment versus a $(NH_4)_2S$ treatment before Schottky diode fabrication by means of comparing the electrical characteristics of the two resulting samples. It was found that the forward characteristics of the $(NH_4)_2S$ treated sample is "near ideal", and that the HCl treated samples behavior is more close to a MIS diode due to the oxide layer remaining on the surface after treatment. As a consequence, the series resistance of the HCl samples is generally higher than that of the $(NH_4)_2S$ samples, which also yielded less oxide and a lower barrier height.

From this short review is it clear that there is a great spread among surface treatments of GaN surface before metallization. This is itself a serious technological challenge: the heterogeneity of results spans from the different growth methods of GaN, the physical state of the resulting epitaxy (thickness of active layer, doping, morphology) and the kind of substrate used. Moreover, if the expanse of reagent concentrations, temperatures of reaction and time of exposure employed in the literature is taken into account, the challenge is served.

Thus, the unique way forward would be accurate testing of as much parameters as possible, in a rigorous scientific framework. But this strategy can prove to be highly time-consuming. Hence, another approach can be put into action: first of all, it is important to establish a correlation between the chemical procedures employed and their effect on the final electrical characteristics of the diodes. Investigating the effects of the treatments on surface morphology and contamination is important in order to build a complete picture but it is secondary with respect to the electrical behavior of the diode. This is something that in the literature is not always clear. Secondly, from the short literature review cited above, one can summarize some peculiar effects of each treatment that transcend the eventual differences between GaN epitaxies. For instance, it is clear that HCl removes O and C contaminants but leaves the surface with Cl contamination, while HF is very effective in removing oxide and C contaminants. KOH can effectively remove C on the surface, but under certain condition, it may be able to etch GaN. Therefore, when time is limited, an educated guess can be made in choosing a limited number of chemical surface treatments, concentrations and time of exposure.

The process described in the previous sections was applied to GaN on three substrates: sapphire, silicon and silicon carbide. Hence, the same three chemical treatments were applied to each substrate:

- HCl (37%) for 2 min;

- *HF* (1%) for 30 s;
- *KOH* at 80 °C for 1 min.

The effect of said treatments was characterized in terms of electrical characterizations, AFM scans and XPS analysis.

2.3.1 XPS Analysis

Amid the relevant XPS studies in the literature, King et al. [139] investigated, among several methods, the combination of UV/O3 oxidation and exposure to acids and based such as *HCl*, *HF* and *BHF*. Their XPS analysis showed that the oxygen surface coverage was inversely proportional to the amount of *Cl* detected on the surface, and similar behavior between carbon and oxygen.

Moldovan et al. [142] studied the effects of *KOH* treatment on the surface of n-GaN. From XPS analysis, the *KOH* treatment resulted effective in an increase of the *N* surface content and a decrease of the *Ga* surface content. Moreover, a decrease in the *C* surface contamination was noted. The binding energy of the O_{1s} peaks remained unchanged.

Rickert et al [143] demonstrated that, after *KOH* treatment, the Ga_{3d} peak lies approximately 0.3 eV toward lower binding energy, which corresponds to a shift of the surface Fermi level closer to the valence band maximum [144]. A shift of this type could result in an increased contact resistance. The same effect was produced with *HCl* treatment, Ultimately, they concluded that the *KOH* treatment decreases the Ga/N ratio, because of the removal of *Ga* from the surface due to formation and dissolution of *Ga*-based hydroxide [145]; the *HCl* treatment tends to increase the Ga/N ratio due to the removal of *N*-based species from the surface.

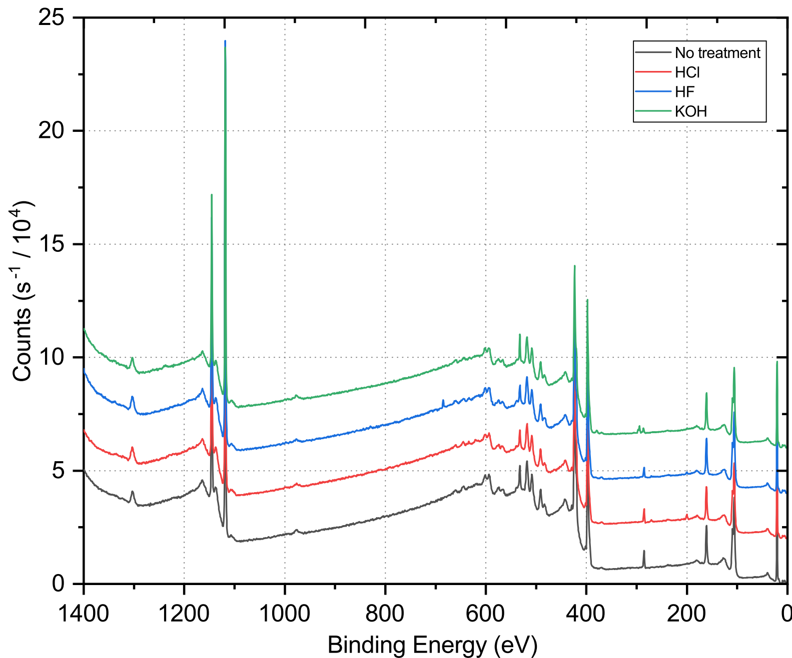

Figure 2.19: XPS survey spectra for GaN on SiC samples

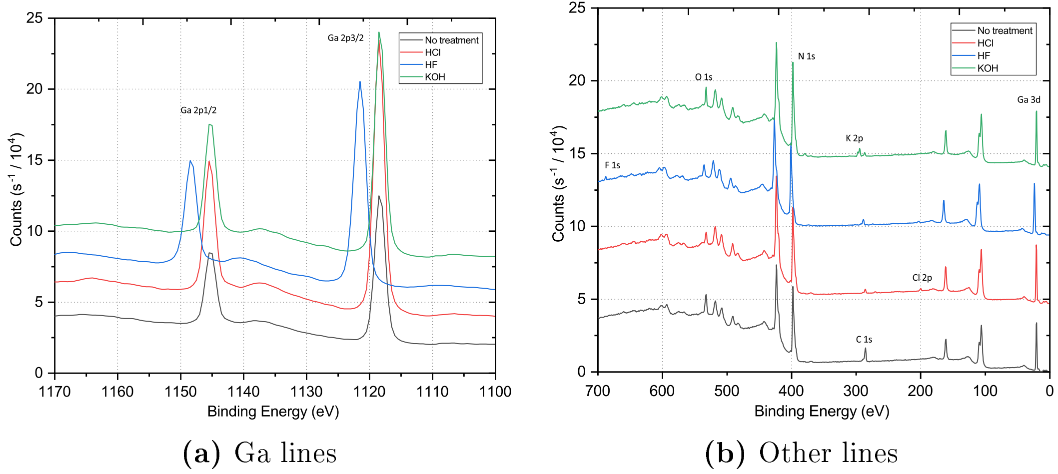

(a) Ga lines **(b)** Other lines

Figure 2.20: XPS survey spectra for Ga, N and other lines for GaN on SiC samples

XPS survey spectra were acquired for all samples covering the 0–1400 eV binding energy range. As example, Fig. 2.20 shows the XPS survey spectra for GaN on SiC samples. All the spectra were dominated by *N* and *Ga* peaks (Fig. 2.19 and Fig. 2.20a), with minor differences and a binding energy shift for the HF-treated GaN on SiC sample, that however was observed for all the peaks of the spectrum, thus probably a result of charging effects, meaning that the surface was more resistive.

Sample	N_{1s}/Ga_{3d}	C_{1s}/Ga_{3d}	O_{1s}/Ga_{3d}
GaN/SiC : No	0.868	0.429	0.261
GaN/SiC : HCl	0.839	0.093	0.130
GaN/SiC : HF	0.897	0.151	0.144
GaN/SiC : KOH	1.040	0.081	0.180
GaN/Si : No	0.789	0.255	0.173
GaN/Si : HCl	0.860	0.224	0.140
GaN/Si : HF	0.868	0.165	0.136
GaN/Si : KOH	0.932	0.064	0.157
GaN/Al_2O_3 : No	0.786	0.094	0.407
GaN/Al_2O_3 : HCl	0.815	0.070	0.282
GaN/Al_2O_3 : HF	0.788	0.089	0.303
GaN/Al_2O_3 : KOH	1.317	0.062	0.174

Table 2.4: Quantitative analysis of elemental intensities

By performing a quantitative analysis (Table 2.4), some distinct trends are revealed. First of all, the fact that the N_{1s}/Ga_{3d} ratio does not give a value of 1 is probably due

to errors in the sensitivity factors but may also be due to some surface composition variations from the 1 : 1 stoichiometry. Still, by comparing the relative values it can be seen that KOH treatment increase the N_{1s}/Ga_{3d} ratio. Then, it can be seen from the C_{1s}/Ga_{3d} and O_{1s}/Ga_{3d} ratios that HCl and HF treatments are effective in decreasing the C and O content present on the surface, but leave, respectively, Cl and F contamination (Fig. 2.20b). This is true for all three epitaxies. KOH treatment instead left a K_{2p} contamination but effectively decreased the carbon contamination and, at the same time, increased the oxygen content.

2.3.2 AFM Scans

AFM images were taken from randomly selected areas (5 µm × 5 µm) for all three epitaxies and for each surface chemical treatment. For instance, the AFM scans for the GaN on SiC samples can be seen in Fig. 2.21.

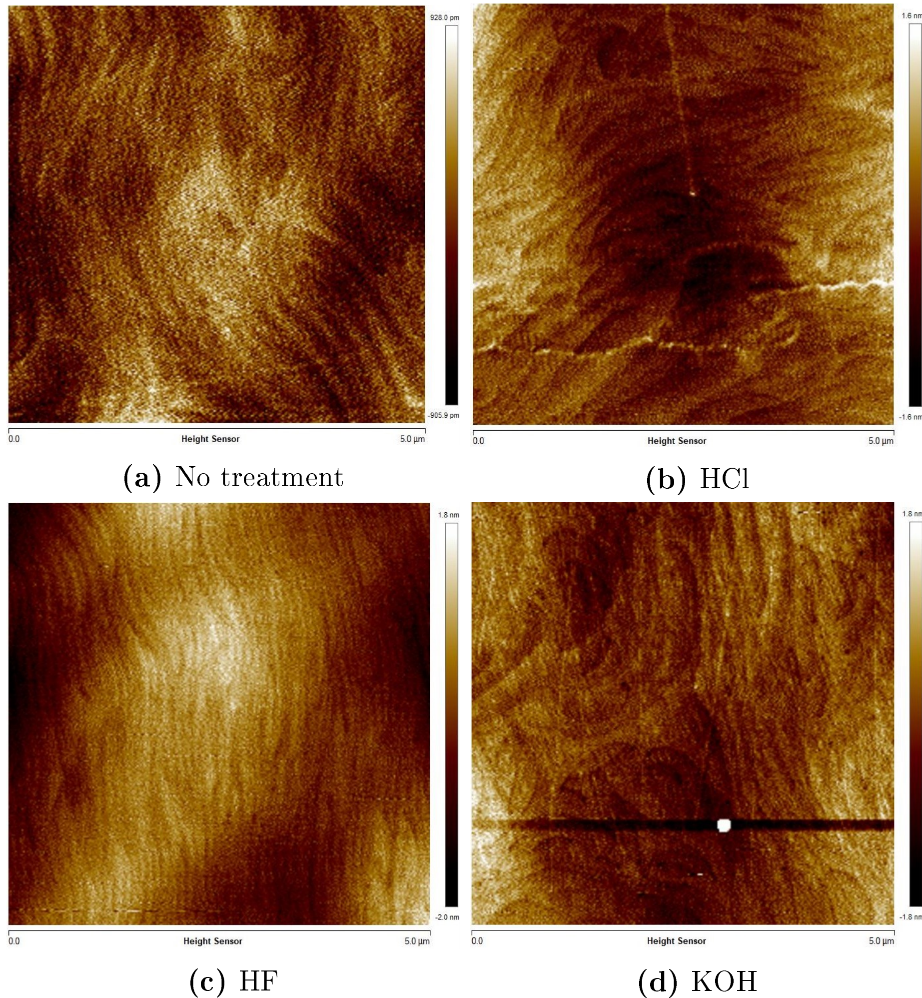

(a) No treatment

(b) HCl

(c) HF

(d) KOH

Figure 2.21: AFM images from randomly selected 5 µm×5 µm areas of GaN on SiC samples for each of the surface treatments performed

The surface roughness of the chemically treated samples was evaluated by AFM to check if any relevant modification of the surface morphology can be related to the different electrical behavior of the Schottky diodes. The root mean squared surface roughness of each sample is reported in Table 2.5.

	No treatment	HCl	HF	KOH
Al_2O_3	0.373	1.810	3.423	0.362
Si	0.749	0.674	0.603	0.496
SiC	0.266	0.470	0.595	0.404

Table 2.5: Root mean squared (rms) surface roughness (in nm) calculated from the AFM scans on all samples)

It must be stated that the AFM scans were performed on all the samples prior to Schottky diode fabrication process. Therefore, the measurements of surface roughness do not include any probable surface morphology modification that the sample surface might undergo during process. By comparing the data of Table 2.5, it can be seen that the same type of treatment applied to the three epitaxies had different results in terms of surface morphology modification. The untreated GaN on SiC sample was fairly smooth, with an rms surface roughness of 0.266 nm, while all surface chemical treatments increased the rms surface roughness, with HF being the treatment that yielded the highest rms surface roughness (0.595 nm). The untreated GaN on Si sample was the worst (in terms of surface roughness) among the three epitaxies, which is probably due to the fact that GaN on Si heteroepitaxy is characterized by the highest lattice constant mismatch; however, it must also be said that these three epitaxies have profound differences in terms of active layer thickness, intermediate layers thickness and composition, and origin (Fig. 2.1). The chemical surface treatments slightly decreased the surface roughness of the untreated GaN on Si sample.

2.4 Thermal Annealing

The scattering among reported value of Schottky barrier height of Pt-GaN Schottky diode can be partly attributed to the presence or absence of a thermal annealing treatment. Pt is widely employed since it is an ideal choice to form a Schottky barrier with GaN because of its high work function (ϕ_M =5.65 eV). Moreover, it is chosen also because of its resistance to oxidation and corrosion. However, the behavior of Pt-GaN Schottky contacts may change due to the thermal annealing employed. Moreover, this heterogeneity is characteristics of other metal contacts to GaN. This depends from the non-idealities present at the metal/semiconductor interface, the spread of GaN epitaxial layers employed and the fabrication process. In fact, in a real metal/semiconductor interface, metal is deposited on an as-grown semiconductor surface, either fully cleaned and with reasonably smooth surface, or either fully cleaned and with a rough surface. Chemical treatment prior to metallization on a smooth semiconductor surface can be beneficial for the removal of oxides and hydroxides from the semiconductor surface. If the semiconductor surface is rough or moderately rough (perhaps after RIE prior to Schottky contact metallization), after metal deposition there can be some disturbances in the semiconductor surface lattice structure [146]. As a consequence, stress is generated producing a disordered layer in the semiconductor surface immediately close to the metal. Rapid thermal

annealing (RTA) could have a beneficial effect.

As the metal/semiconductor system cools down from the RTA temperature, the lattice structure tends to reorder itself by trying to provide the largest energy gain by cohesion. The metal atoms interact with the loosely bound semiconductor atoms, and this favors structural rearrangements, resulting in possible alloys or solid solutions in the proximity of the metal/semiconductor interface. When the structural reorganization is accomplished, each metal atom is now as close as possible to the nearest semiconductor atom or atoms, and these are bonded tightly. Consequently, the contact is robust and a change in barrier height is produced. This physical process is strongly dependent on the characteristics of the metal, the metal combination employed, the metal thickness, the metal deposition process, the RTA time, RTA temperature, the rate of increase of the temperature in the RTA process and, of course, from the cleanliness of the semiconductor surface.

Wang et al. [147] studied the thermal annealing effects on a 180 nm thick Pt Schottky contact on a 1.2 µm GaN epilayer. They analyzed annealing temperatures of 500 °C, 600 °C, 700 °C, 800 °C, for 30 min in a N_2 atmosphere. Their findings indicate that there is a slight increase in barrier height at 500 °C, while it decreases greatly with annealing temperatures of 600 °C and above. The increase in barrier height can be correlated with a reduction of non-stoichiometric defects at the interface [148, 149], while the decrease above 600 °C is attributed to a general degradation of the contact, associated to a general increase of the contact roughness, and a sensible degradation of the Schottky diode characteristics [150].

In this work, all three epitaxies used underwent a thermal annealing study. The samples of GaN on sapphire and GaN on Si were annealed at temperatures of 200 °C, 300 °C, 400 °C, and 500 °C, for 5 min, in a N_2 atmosphere. The temperature was increased from room temperature up to the annealing temperature with a rate of 10 °C/s. For the samples of GaN on SiC a different strategy was employed based on the results obtained with the other two epitaxies: the annealing at 200 °C was discarded, given the negligible difference in results with the non-annealed samples obtained precedently, and the samples were annealed at 300 °C, 400 °C, and 500 °C, in the same atmosphere and with the same rate of increase as described before. Moreover, an ulterior sample was annealed at 400 °C, always in N_2 atmosphere, but this time the temperature was increased with a rate of 5 °C/s.

The results were characterized in terms of electrical characterizations (Chapter 3.6) and morphological change (through AFM scans).

2.4.1 Schottky Contact AFM Scans

AFM images were taken from randomly selected areas (5 µm × 5 µm) from Schottky contacts fabricated on GaN on SiC. The contacts analyzed were the as-deposited contact and the contacts annealed at 300 °C, 400 °C, and 500 °C. The AFM scans for the Schottky contacts can be seen in Fig. 2.22 (2D images) and Fig. 2.23 (3D images).

The resulting root mean squared surface roughness resulted to be 20.2 nm for the as-deposited sample, 2.2 nm for the sample annealed at 300 °C, 1.3 nm for the sample annealed at 400 °C, and 0.8 nm for the sample annealed at 500 °C. The sensible

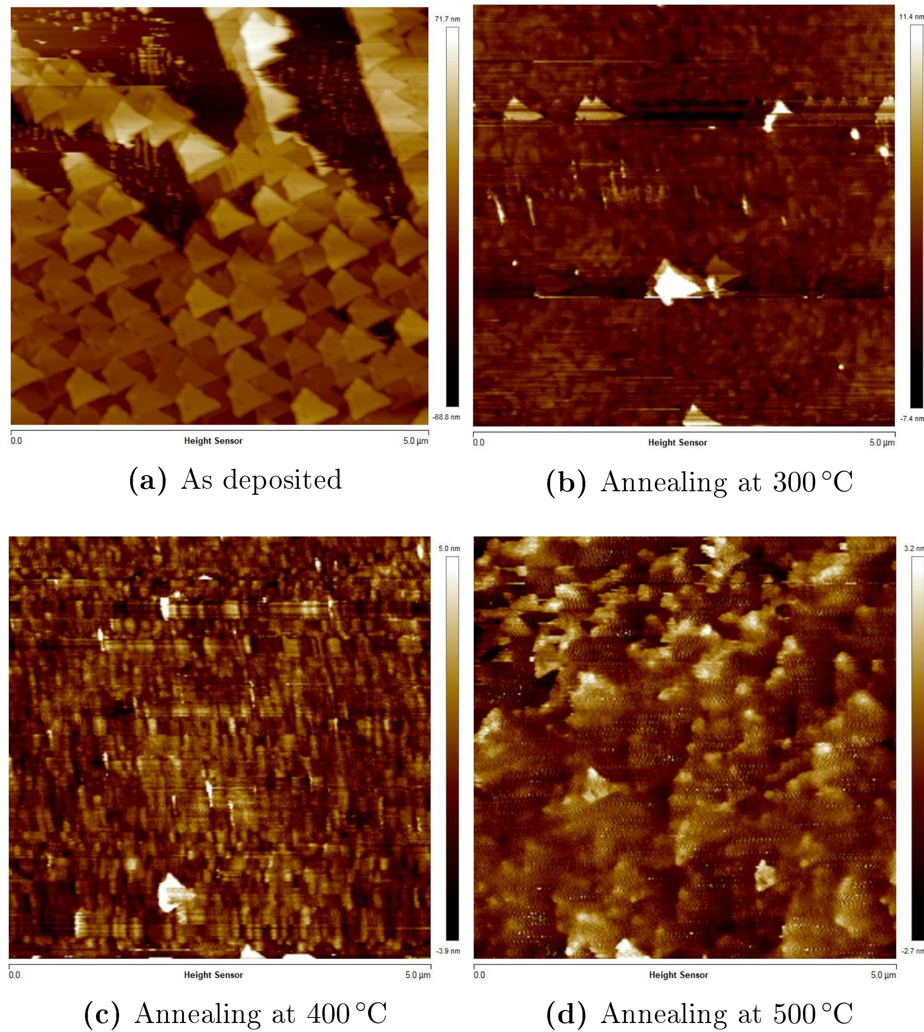

(a) As deposited

(b) Annealing at 300 °C

(c) Annealing at 400 °C

(d) Annealing at 500 °C

Figure 2.22: AFM images from randomly selected 5 µm×5 µm areas of Schottky contacts on GaN on SiC samples for different thermal annealing conditions

improvement of the annealed contact compared to the as-deposited contact yielded a higher breakdown voltage (Section 3.8) and improved Schottky diode parameters (Section 3.7). In the case of GaN on SiC Schottky diodes, no degradation of the Schottky diode performances was observed on the diodes annealed at 500 °C, as opposed to the degradation observed on the Schottky diodes fabricated on GaN on sapphire and GaN on Si. However, the extracted Schottky diode parameters were characterized by a high degree of heterogeneity.

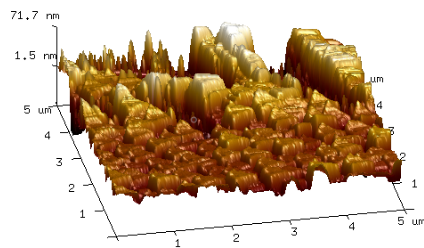

(a) As deposited

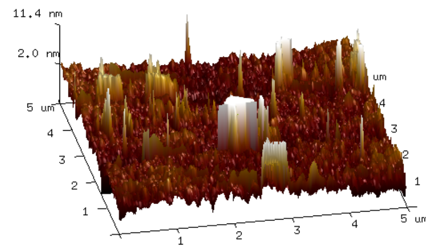

(b) Annealing at 300 °C

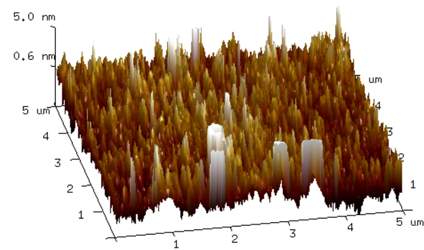

(c) Annealing at 400 °C

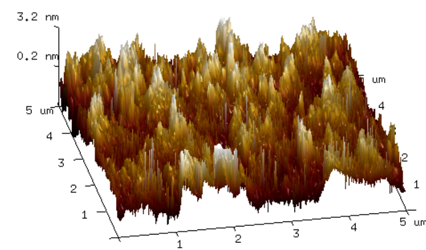

(d) Annealing at 500 °C

Figure 2.23: 3D AFM images from randomly selected 5 µm×5 µm areas of Schottky contacts on GaN on SiC samples, for different thermal annealing conditions

Chapter 3

Schottky Diode Characterization

3.1 Metal-Semiconductor Contacts Theory

A metal-semiconductor (MS) junction is one of the simplest electronic devices, but nonetheless one of substantial scientific and technical interest due to its attractive properties and abundant applications in technology.

When a metal enters in contact with a semiconductor, a barrier is formed at the interface, a barrier responsible for controlling the conduction and the capacitance behavior of the junction.

3.1.1 Ideal Metal-Semiconductor Contacts

The energy band diagram for a MS junction on a n-type semiconductor before metal and semiconductor are put in contact is shown in Fig. 3.1. ϕ_M and ϕ_S are, respectively, the metal and the semiconductor workfunctions (i.e., the energy needed to liberate an electron from the semiconductor surface to the vacuum level E_0, and is equal to the difference between the Fermi and the vacuum levels measured in eV). The energy difference between the minimum of the conduction band E_C and the vacuum level E_0 is called the semiconductor electron affinity χ_S.

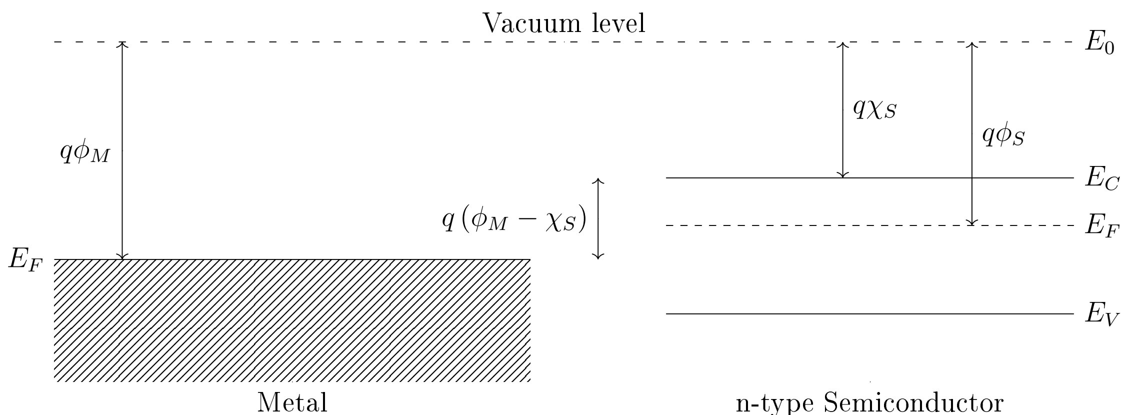

Figure 3.1: Schematic energy band diagram of a metal and a n-type semiconductor before they are put in contact

Before contact, the energies of the semiconductor electrons are higher than those of the metal electrons, due to the difference in Fermi levels [151, 152]. When the metal is in contact with the semiconductor (Fig. 3.2), electrons flow from the semiconductor to the metal, resulting in a positively-charged depletion region in the semiconductor. The flow of electrons last until the difference between semiconductor and metal Fermi levels is compensated by the resulting potential. Due to the accumulation of electrons on the metal surface, a potential barrier is formed, known as the built-in voltage (V_{bi}). In the same way, electron on the metal side also experience a potential barrier known as the Schottky barrier (ϕ_B). The built-in potential and the Schottky barrier height are given, respectively, from Eq. 3.1 and Eq. 3.2:

$$V_{bi} = \phi_M - \phi_S \tag{3.1}$$

$$\phi_B = \phi_M - \chi_S \tag{3.2}$$

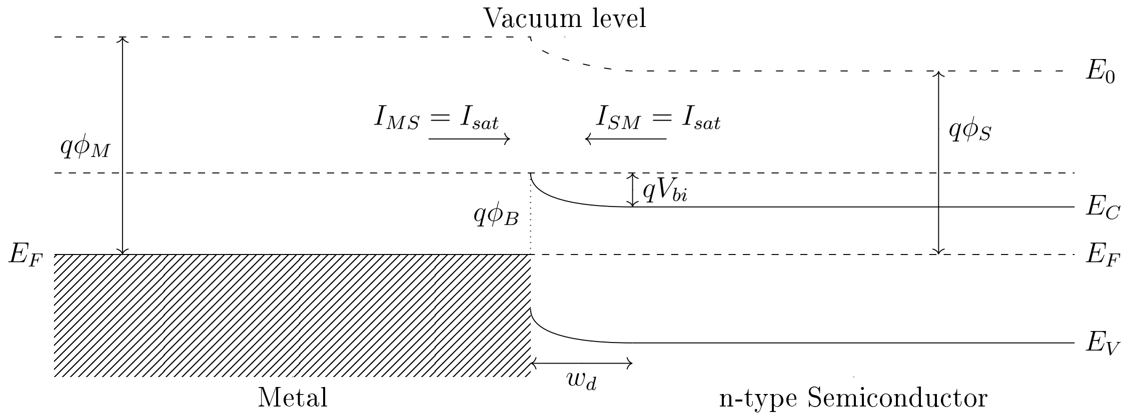

Figure 3.2: Schematic energy band diagram of a metal and a n-type semiconductor after they are put in contact

At thermal equilibrium, the net current passing through the contact is zero ($I_{SM} = -I_{MS}$, where I_{SM} is the current flowing from semiconductor to metal, and I_{MS} is the current flowing from metal to semiconductor). The MS contact becomes forward biased when a negative voltage is applied to the n-type semiconductor with respect to the metal. In this condition, the width of the depletion region is decreased and the built-in potential decreases from its value at thermal equilibrium qV_{bi} to $q\,(V_{bi} - V)$. Due to this barrier reduction, more electrons can flow easier from the semiconductor into the metal. I_{SM} increases exponentially above its value at thermal equilibrium (I_{sat}) according to the relation:

$$I_{SM} = I_{sat} \exp\left(\frac{V}{V_T}\right) \tag{3.3}$$

where the term V_T represents the thermal voltage k_BT/q. The Schottky barrier height ϕ_B remains constant with bias, and I_{MS} remains the same as its thermal

equilibrium value I_{sat}- Therefore, the net current flow across the contact in forward bias is:

$$I = I_{SM} - I_{MS} = I_{sat} \exp\left(\frac{V}{V_T}\right) - I_{sat} = I_{sat}\left[\exp\left(\frac{V}{V_T}\right) - 1\right] \tag{3.4}$$

The MS contact is under reverse bias when a positive voltage is applied to the n-type semiconductor with respect to the metal. Under reverse bias conditions, the width of the depletion region is increased and the value of the built-in potential increases from its thermal equilibrium value qV_{bi} to $q\left(V_{bi} + V\right)$. Thus, the electron moving from the semiconductor to the metal face an increased potential barrier. A bias of few hundreds mV would be enough to stop electron transport from the semiconductor to the metal. Therefore, the current I_{SM} becomes zero. However, I_{MS} remains unchanged from the I_{sat} value, as the Schottky barrier height remains constant.

3.1.2 Current Mechanism in Schottky Diodes

In forward bias, current transport in a Schottky diode is typically divided in some basic conduction mechanism: thermionic emission (TE) of electrons over the barrier, quantum-mechanical tunneling of electrons through the barrier, and generation-recombination in the depletion region. In the ideal Schottky diode, the current is assumed to be purely thermionic emission current (I_{th}). The contribution of other current mechanism is considered a departure from the ideal behavior of the diode [151, 152].

For moderately doped semiconductors, thermionic emission is the dominant mechanism at room temperature, while tunneling is dominating at low temperatures or at room temperature in the case of heavily doped semiconductors. In any given Schottky diode, the current is composed of a combination of all these mechanisms, but typically only one of them is the dominant current conduction mechanism.

Thermionic Emission

For lightly doped semiconductors, thermionic emission is supposed to be the dominant current conduction mechanism for Schottky contacts. According to TE theory, only charge carriers with energies higher than the potential barrier can overcome it and generate the diode current. The ideal I-V characteristics of a Schottky diode can be described by Eq. 3.5:

$$I = I_{sat}\left[\exp\left(\frac{qV}{k_B T}\right) - 1\right] \tag{3.5}$$

where I_{sat} is the saturation current

$$I_{sat} = AA^{*}T^{2} \exp\left(\frac{-\phi_B}{k_B T}\right) \tag{3.6}$$

The symbol A^* is referred to as the Richardson's constant and is defined by Eq. 3.7:

$$A^* = \frac{4\pi q k_B^2}{h^3} \frac{m_n^*}{m_0} \tag{3.7}$$

where h is Planck's constant ($6.626 \cdot 10^{-34}\,\mathrm{m^2\,kg/s}$), m_0 is the rest electron mass in vacuum ($9.11 \cdot 10^{-31}\,\mathrm{kg}$), and m_n^* is the electron effective mass. By substituting each constant in Eq. 3.7 with their respective values, one obtains:

$$A^* = 120\frac{m_n^*}{m_0} \longrightarrow \left[\frac{\mathrm{A}}{\mathrm{cm^2\,K^2}}\right] \tag{3.8}$$

Therefore, Richardson constant is a function of the semiconductor, since its value depend on the ratio of the electron effective mass to the rest electron mass in vacuum. The effective electron mass for wurtzite GaN is (at 300 K) $0.22m_0$ [153]. Consequently, the Richardson constant for wurtzite GaN at room temperature is, from Eq. 3.8, $26.4\,\mathrm{A\,cm^{-2}\,K^{-2}}$.

Tunneling Mechanism

Electrons with energies lower than the barrier height can overcome it by quantum-mechanical tunneling. Tunneling is the dominant transport mechanism for heavily doped semiconductors and/or for operations at very low temperatures [60], as well as in the case of a metal contact on a degenerate semiconductor.

At low temperatures, the Schottky diode forward current is due predominantly to tunneling of electrons with energies at the Fermi level. This mechanism is known as *Field Emission* (FE). If the temperature increases, a non-negligible number of electrons can gain energies above the Fermi level, and the tunneling probability increases as the electrons encounter a thinner barrier. Such a tunneling mechanism, due to thermally excited electrons, is called *Thermionic Field Emission* (TFE). Due to the rapid decrease in density of electrons above the Fermi level and the decrease in barrier thickness, the tunneling probability increases with increasing temperature until it reaches a maximum value at a certain energy level. Ulterior increase in temperature brings about a gradual degradation of TFE until it becomes negligible, whereas TE begins to become the dominating transport mechanism as a result of the increased number of thermally excited electrons capable of crossing the barrier [151, 152].

The mathematical expression of the tunneling current has been derived by Crowell et al. [154], by extending the thermionic model given by Eq. 3.5:

$$I_{tun} = I_{tun0} \exp\left(\frac{qV}{E_0}\right) \tag{3.9}$$

where the tunneling probability E_0 is dependent on barrier transparency [155] and

is given by

$$E_0 = E_{00} \coth\left(\frac{E_{00}}{k_B T}\right) \tag{3.10}$$

The tunneling parameter E_{00} is an energy constant directly related to the material [155], calculated from the expression

$$E_{00} = \frac{qh}{4\pi}\left(\frac{N_d}{m^* \varepsilon_S}\right)^{\frac{1}{2}} \tag{3.11}$$

where N_d is the donor concentration and ε_S is the semiconductor permittivity. The value of the saturation current I_{tun0} depends mainly on the barrier height, the temperature, the semiconductor properties and on the applied voltage. The energy constant E_{00} can be used to determine the contribution of thermionic emission and tunneling: at low temperatures, E_{00} has a high value, thus $k_B T/qE_{00} \ll 1$, and $E_0 \cong E_{00}$, and the slope of the semi-log plot of the current against voltage is independent of temperature; this is the case of FE mechanism. At high temperature, E_{00} is relatively low, therefore $k_b T/qE_{00} \gg 1$ and $E_0 = k_B T$. Hence, the slope of the semi-log I-V plot is equal to $q/k_B T$. This case refers to TE. At intermediate temperatures, $E_{00} \cong k_B T$ and $k_b T/qE_{00} \cong 1$, and the slope of the semi-log plot can be written as $\frac{E_{00}}{k_B T} \coth\left(\frac{E_{00}}{k_B T}\right)$. In this case, the main current transport mechanism is thermionic field emission (TFE).

Generation/Recombination Mechanism

Generation and recombination of an electron-hole pair in the depletion region can contribute to the main current component of a Schottky diode. At thermal equilibrium, the rate of the generated electron-hole pairs is equal to the rate of their recombination, thus the net current is zero, whereas the number of generated electron-hole pairs is equal to n_i^2. The rate of generation departs from this value when a voltage is applied to the barrier. A net generation or recombination current will take place, depending on the applied bias direction. Assuming an n-type semiconductor, if a reverse bias is applied to the Schottky diode, the rate of electron-hole pair generation increases in the depletion region. These pairs will cross the barrier under the effect of the electric field, thus producing the reverse current component. When the diode is forward biased, the electrons will flow out from the neutral bulk semiconductor to the depletion region and the holes will flow out from the metal. Electrons will recombine with holes because of their accumulation in the depletion region forming a forward recombination current component. Recombination also occurs by localized centers such as deep trap centers that have energies comparable to the mid-gap.

The generation-recombination current I_{gr} is given by:

$$I_{gr} = Igr0\left[\exp\left(\frac{qV}{2k_B T}\right) - 1\right] \tag{3.12}$$

where

$$I_{gr0} = \frac{qn_i w_d}{2\tau_0} \tag{3.13}$$

and w_d is the depletion region width and τ_0 is the carrier lifetime in the depletion region. In some Schottky diodes, the recombination current is responsible for the non-ideality in forward bias, where $n > 1$. The generation current is a common cause of the unsaturated current in reverse bias. The ratio between the generation/recombination saturation current I_{gr0} and the thermionic emission saturation current is given by

$$\frac{I_{gr0}}{I_{th0}} = \frac{qn_i}{A^*T^2}\left(\frac{w_d}{2\tau_0}\right)\exp\left(\frac{\phi_B}{k_BT}\right) \tag{3.14}$$

According to Eq. 3.14, the generation/recombination current is more critical in diodes with high barriers on lightly doped semiconductors (i.e, large values of w_d), and it is more evident at low temperatures due to its lower activation energy compared to thermionic emission.

3.1.3 Non-Ideal Characteristics of Schottky Diodes

Virtually almost all of the experimental I-V characteristics of Schottky diodes deviate from the ideal behavior of the TE model, in both forward and reverse bias condition. Thus, the thermionic emission I-V model must be modified in order to fit experimental observations [60]. A dimensionless factor, known as the *ideality factor* n has been introduced to the exponential term in the ideal Schottky diode equation (Eq. 3.5) to obtain the following expression:

$$I = I_{sat}\left[\exp\left(\frac{qV}{nk_BT}\right) - 1\right] \tag{3.15}$$

A typical Schottky diode characteristics can be seen in Fig. 3.3.

For an ideal metal-semiconductor contact, which assume pure thermionic emission current, the ideality factor takes a value of unity, $n = 1$. Any deviation from this ideal behavior can increase the ideality factor beyond unity. Tunneling current and generation/recombination current are among these non-ideal contributions. Other behaviors that contribute to the overall non-ideality of the Schottky contact I-V characteristics, and thus to the increase of the value of the ideality factor, are attributed to the bias dependence of the barrier height and image-force lowering, or even to the presence of an interfacial insulating layer at the metal-semiconductor interface.

Image-Force Lowering

In a metal/semiconductor contact, the injection of an electron from metal to the semiconductor induces an equal positive image charge inside the metal. The induced

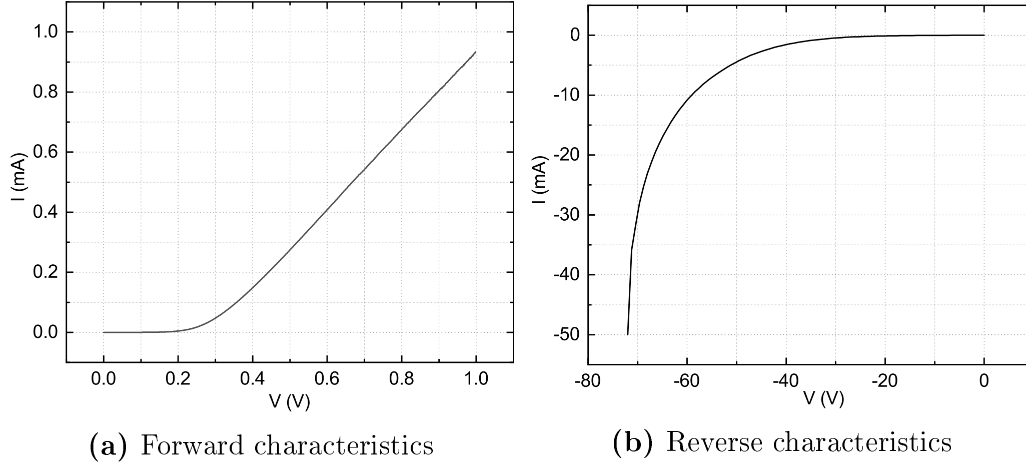

(a) Forward characteristics **(b)** Reverse characteristics

Figure 3.3: Experimental DC characteristics for a 70 µm diode (GaN on SiC)

positive image charge (called *image force*) tends to pull back the electron into the metal with a Coulomb attraction force equal to

$$F = \frac{q^2}{4\pi\varepsilon_S\left(2x\right)^2} = \frac{q^2}{16\pi\varepsilon_S x^2} \tag{3.16}$$

where x is the distance between the electron and the surface, and with corresponding electrical field ξ_{IF}:

$$\xi_{IF}\left(x\right) = -\frac{F(x)}{q} = -\frac{q}{16\pi\varepsilon_S x^2} \tag{3.17}$$

The equivalent potential energy of the electric field is equal to:

$$V_{IF} = -\int_x^{\infty} \xi_{IF}(x)dx = -\frac{q}{16\pi\varepsilon_S x} \tag{3.18}$$

The resultant image potential energy must be combined with the potential energy of the Schottky barrier, the potential inside the depletion region, and is assumed to be constant near the surface with a maximum value:

$$\xi_{max} = \sqrt{\frac{2qN_d\left(\phi_B - E_{CF} + V_a\right)}{\varepsilon_S}} \tag{3.19}$$

Thus, in the presence of an external electric field, the electrostatic potential is given by:

$$\Phi\left(x\right) = -q\xi_{max} - \frac{q^2}{16\pi\varepsilon_S x} \tag{3.20}$$

The maximum barrier height occurs at the distance from the metal/semiconductor interface where the electrostatic field of the image charge force and the depletion region are equal and opposite:

$$x_m = \sqrt{\frac{q}{16\pi\varepsilon_S\,|\xi_{max}|}} \tag{3.21}$$

Therefore, the maximum barrier potential reduction is given by:

$$\Delta\phi_B = \sqrt{\frac{q\xi_{max}}{4\pi\varepsilon_S}} = 2x_m\,|\xi_{max}| \tag{3.22}$$

And the barrier height would be given by:

$$\phi_B = \phi_{B0} - \Delta\phi_B \tag{3.23}$$

The barrier reduction due to image-force lowering depends mainly on the applied voltage V_a, the semiconductor dielectric constant ε_S, the doping concentration N_d, and the difference between the Fermi level and the maximum of the conduction band of the semiconductor. Because of this, the saturation current becomes bias dependent and the reverse bias current will not saturate [152].

Interfacial Layers

Most of the semiconductors used for Schottky diodes have an interfacial native oxide layer a few Angstrom thick (typically around 10 Å). This layer develops when the semiconductor is exposed to air and thus will be sandwiched between semiconductor and metal. This interfacial oxide layer acts as an insulator layer in a metal/semiconductor contact and this can alter the diode performance. Both the barrier height and the ideality factor are affected by this. In the presence of an insulating layer, when an electric field is applied, there is a voltage drop on the insulator, and the barrier height at zero bias is in turn lower than it would be in an ideal system without the insulator layer.

The barrier reduction in terms of the maximum electric field (ξ_{max}) in the semiconductor can be written as:

$$\phi_B = \phi_B^0 - \alpha\xi_{max} \tag{3.24}$$

where ϕ_B^{ZB} is the zero-bias barrier height and

$$\alpha = \frac{\delta\varepsilon_S}{\varepsilon_i + q\delta D_S} \tag{3.25}$$

where δ is the insulator layer thickness. Therefore, the barrier height reduction depends on the maximum electric field ξ_{max} in the semiconductor and Eq. 3.24 is valid for any applied voltage if the density of interface states D_S remains constant

over the entire energy. The barrier reduction is higher for interfacial layers with a lower dielectric constant (ε_i).

The higher ideality factor (compared to the ideal case) is due to the fact that the interfacial layer acts as a tunnel barrier that is thin enough so that at low forward voltages it does not restrict the current flow. With an applied forward bias, the depletion zone begins to decrease and consequently both the electric field and voltage drop across the insulator decrease causing a variation of the barrier height with the applied voltage. This variation is expressed in terms of the ideality factor:

$$n^{-1} = \left(1 - \frac{\partial \phi_B}{q \partial V}\right) \tag{3.26}$$

Thus, the ideality factor is bias independent only when the oxides energy states at the semiconductor/oxide interface are uniformly distributed.

Surface States

As stated in section 2.2.3, experimental values of the barrier height ϕ_B are less sensitive to the value of the metal workfunction ϕ_M than what is expected from Eq. 3.2. Bardeen [156] attributed this discrepancy to the presence of a high density of surface states at the semiconductor surface. For metal/semiconductor contacts possessing a high density of surface states, the Fermi level position is "pinned" within the bandgap and becomes independent of ϕ_M. Non-ideal surface termination (i.e., interruption of the crystal lattice periodicity) causes dangling bonds in the semiconductor surface which are responsible for the presence of surface states. These states can be occupied or empty, depending on their position with respect to the Fermi level.

Ideality Factor

The ideality factor is an empirical rule of thumb to indicate the grade of deviation of a Schottky diode I-V characteristics from pure thermionic emission. For an ideal diode (i.e., pure TE) the ideality factor n is unity. However, in real-life Schottky diodes, many factors contribute to non-idealities that cause other current mechanisms other than TE, which in turn increase the ideality factor. Tunneling and/or generation/recombination current, image-force lowering, interface states, are all elements that contribute to the increase of the ideality factor.

The ideality factor n is expected to be independent of the temperature. However, many instances in the literature [127, 157–160] report a non-negligible dependence on the temperature. In reality, the ideality factor does not depend directly on the temperature. Being an indication of how much a Schottky diode forward characteristics is close to pure thermionic emission theory, the ideality factor is bound to increase when other non-ideal current transport mechanisms, such as tunneling or generation/recombination, become more predominant. Thus, the ideality factor "dependence" on temperature should be interpreted as a consequence of the fact that tunneling, generation/recombination, or more general leakage current are not anymore negligible with respect to thermionic emission current. Indeed, in some cases, the ideality factor results to be a rather crude measure of what is happening,

from a physical point of view, inside a Schottky diode. Suzue et al. [161], for instance, decoupled the main Schottky diode current into its four main components, thus eliminating altogether the need for the ideality factor.

Nonetheless, it has been proposed [162] that the I-V measurements at different temperatures can be used to identify (in first instance) the main current transport mechanism of the analyzed Schottky diode by observing the variation of n with temperature. From each I-V measurement performed at the different temperatures, the ideality factor can be evaluated. Then, a plot of nk_BT/q vs k_BT/q can be constructed (Fig. 3.4). If field emission is dominant (i.e., tunneling), nk_BT/q will be a straight line, while for thermionic field emission it has a weak temperature dependency at low temperature, increasing with temperature. When thermionic emission is dominant, nk_BT/q has a strong temperature dependence, in both the ideal case ($n = 1$) and the real-life case ($n \geq 1$).

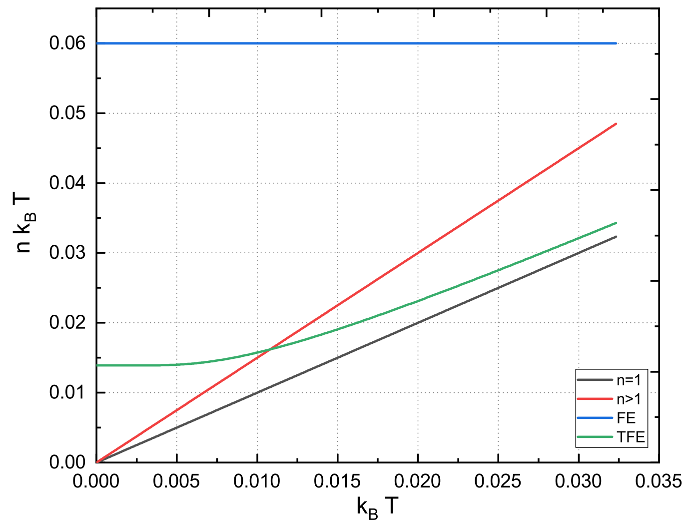

Figure 3.4: Theoretical nk_BT vs k_BT plot, detailing the case of ideal thermionic emission ($n = 1$), non-ideal thermionic emission ($n > 1$), FE and TFE

3.2 DC Characterizations

The DC characteristics of all the diodes in this work were measured with an Agilent E5263A 2 Channel IV Analyzer / Source Monitor Unit.

3.2.1 TE Fit

For moderately doped semiconductors, the I-V characteristics in forward bias, with $V > 3k_BT/q$, is given by [60]:

$$J = J_0 \exp\left(\frac{qV}{nk_BT}\right) \tag{3.27}$$

$$J_0 = A^*T^2 \exp\left(-\frac{q\phi_{B0}}{k_BT}\right) \tag{3.28}$$

The barrier height and the ideality factor can be extracted by plotting the current density on a semi-logarithmic scale, i.e., $\ln(J)$ versus V. This plot yields a straight line whose slope can be used to extract the ideality factor:

$$n = \frac{q}{k_B T} \frac{dV}{d\,(\ln J)} \tag{3.29}$$

while the intercept on the y-axis yields the value of $\ln(J_0)$ at zero voltage. The extrapolated value of current density at zero voltage is the saturation current J_0, and the barrier height can be obtained from the equation:

$$\phi_{Bn} = \frac{k_B T}{q} \ln\left(\frac{A^* T^2}{J_0}\right) \tag{3.30}$$

An example of the application of this method can be seen in Fig. 3.5 .

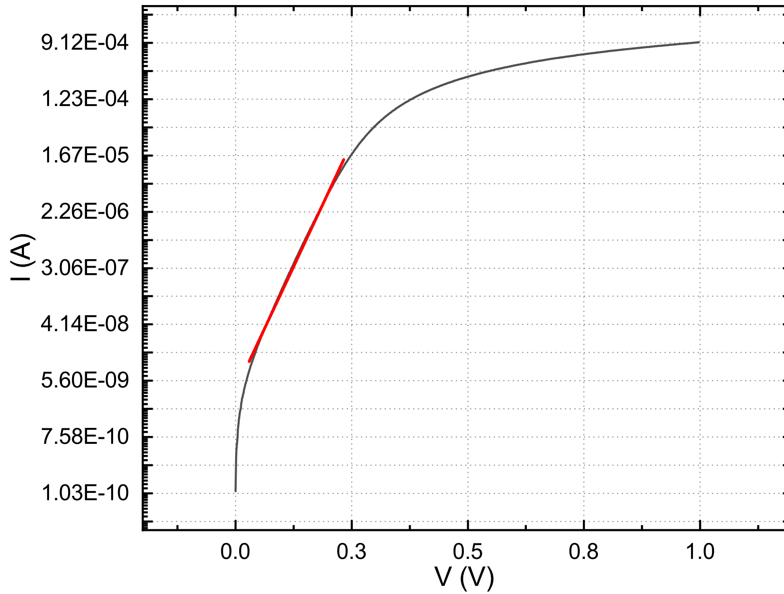

Figure 3.5: Forward characteristics of a 70 µm diode (GaN on SiC) with its linear fit (in red). The barrier height and ideality factor extracted with this fit are, respectively, 0.615 eV and 1.098

The value of ϕ_{Bn} is not, in general, very sensitive to the value of Richardson constant A^*. In fact, at room temperature, an increase of about 100% in the value of A^* will cause an increase of just 0.018 eV in ϕ_{Bn}.

This methodology does not take into consideration the presence of a series resistance R_S, which, in real, practical Schottky diode, is always present. Eq. 3.27 thus becomes (by taking into account the presence of a series resistance R_S):

$$J = J_0 \left[\exp\left(\frac{q\,(V - IR_S)}{n k_B T}\right) - 1\right] \tag{3.31}$$

The series resistance R_S is extracted from the slope of the $I(dV/dI)$ vs I curve (Fig. 3.6) just before the onset of current saturation, based on the following equation [161]:

$$I\left(\frac{dV}{dI}\right) = IR_S + \frac{k_B T}{q} \tag{3.32}$$

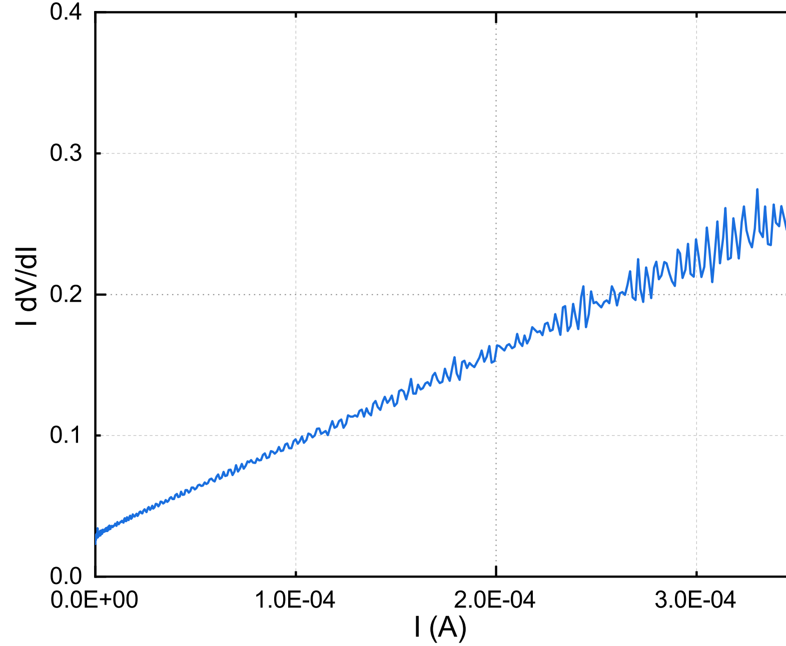

Figure 3.6: Series resistance extraction for the 70 µm diode, following Eq. 3.32. In this case $R_S \approx 640.57\,\Omega$

3.2.2 Norde's Method

The method proposed by Norde [163] consists in estimating the barrier height of a diode with a high series resistance even in the absence of a straight region in the semi-log plot of I versus V. It makes use of an auxiliary function $F(V)$ to represent the I-V measurements of the Schottky diode. This method assumes also that the diode is in its ideal case, i.e., $n = 1$ and that the semiconductor is characterized by a known constant Richardson constant A^*, for simplicity. The barrier height dependence on the applied bias is not taken into consideration. The empirical Norde's function is defined as:

$$F(V) = \frac{V}{2} - \frac{k_B T}{q} \ln\left(\frac{1}{AA^*T^2}\right) \tag{3.33}$$

With the help of Eq. 3.31, Norde's function (Eq. 3.33) can be expressed in terms of ϕ_B and R_S, for voltages larger than a few k_BT/q (typically $V \geq 3k_BT/q$):

$$F(V) = \phi_B + IR_S - \frac{V}{2} \tag{3.34}$$

A plot of Norde's function results in a curve which will have a minimum point, as it can be seen from Fig. 3.7. This point of interest will yield the voltage corresponding to the minimum value of the function, V_0, and the corresponding current, I_0. Then, the barrier height and series resistance can be extrapolated:

$$\phi_B = F\left(V_0\right) + \frac{V_0}{2} - \frac{k_B T}{q} \tag{3.35}$$

$$R_S = \frac{k_B T}{q I_0} \tag{3.36}$$

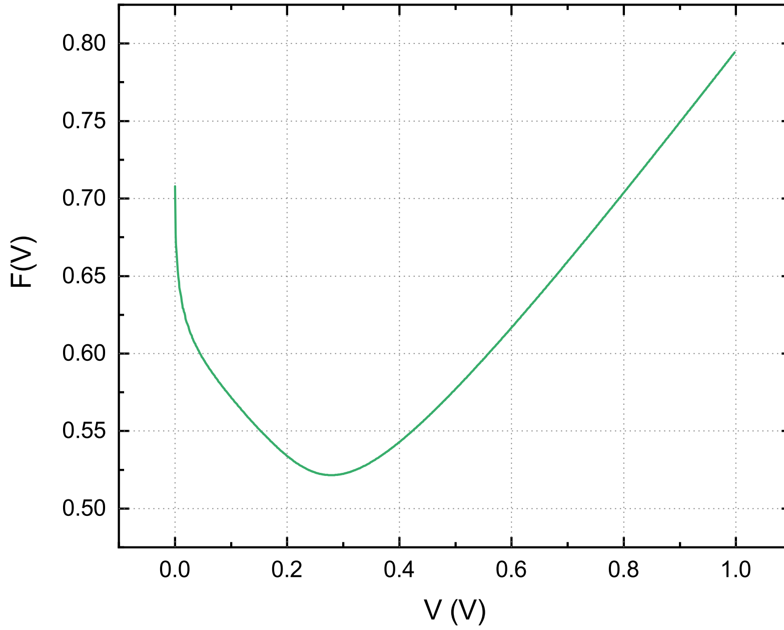

Figure 3.7: Norde's auxiliary function extracted for the 70 µm diode. In this case, the minimum is found at $V_0 = 0.278\,\text{V}$. Therefore, the extracted parameters are $\phi_B = 0.635\,\text{eV}$ and $R_S \approx 807.72\,\Omega$

Norde's method is successful in tackling the effect of the series resistance but it has serious limitations in term of ignoring other important factors. The first and most prominent limitation is the fact that it considers the ideal diode case, which implies a Schottky diode with pure thermionic emission (i.e., $n = 1$), thus ignoring the eventual effect of other mechanisms, such as tunneling or generation/recombination. For instance, a substantial contribution of recombination current results in an underestimation of ϕ_B, while a bias-dependent barrier will yield an overestimation of the barrier height [164]. However, the crucial limitation of this method is that all the diode parameters are extrapolated from a single point of the I-V characteristics, which constitute an enormous source of error.

The efforts to improve Norde's method and minimize the errors and its drawbacks have been numerous [165–169]; some researchers have introduced the ideality factor in order to account for the non-idealities in a diode I-V characteristics, while others have employed the use of several minima points, instead of only one. Sato et al. [166] integrated the ideality factor n in Norde's function and expanded the methodology

in order to determine the values of n, ϕ_B, R_S from two sets of I-V measurements performed at different temperatures. This is a method that can be applied to any diode with ideality factor $1 < n < 2$ using the following expression:

$$F(V) = \left(\frac{1}{2} - \frac{1}{n}\right) V + \phi_B + \frac{IR_S}{n} \tag{3.37}$$

Lien et al. [167] introduced an arbitrary parameter γ to Norde's equation to generate several Norde-like functions $G_\gamma(V, I)$, where γ is an integer number larger than the ideality factor. The resulting function is given by:

$$G_\gamma(V, I) = \frac{V}{\gamma} - \frac{k_B T}{q} \ln\left(\frac{1}{AA^* T^2}\right) \tag{3.38}$$

The values of the barrier height and diode's series resistance can be determined from the following equations:

$$\phi_B = F(V_0) + \frac{V_0}{\gamma} - \frac{k_B T}{q} \tag{3.39}$$

$$R_S = \frac{k_B T(\gamma - n)}{qI} \tag{3.40}$$

where γ is an arbitrary number larger than the ideality factor. A plot of $G_\gamma(V, I)$ versus I for several γ values results in several Norde-like curves. Hence, several values of $I_{0\gamma}$ can be obtained from the minimum value of each $G_\gamma(V, I)$ curve. A plot of $I_{0\gamma}$ versus γ results in a straight line defined by Eq. 3.41:

$$I_{0\gamma} = \frac{1}{R_S \beta}\gamma - \frac{n}{R_S \beta} \tag{3.41}$$

with $\beta = \frac{q}{k_B T}$.

3.2.3 Cheung's Method

Cheung et al [170] presented a different approach that has the benefit of being able to extrapolate the ideality factor, the barrier height and the series resistance of a Schottky diode from a single forward I-V measurement. From Thermionic Emission theory:

$$I = I_0 \left[\exp\left(\frac{qV - IR_S}{nk_B T}\right) - 1\right] \tag{3.42}$$

$$I_0 = A^* T^2 \exp\left(\frac{-q\phi_B}{nk_B T}\right) \tag{3.43}$$

By rewriting Eq. 3.42 in terms of the current density $J = I/A_{eff}$, one obtains:

$$V = R_S A_{eff} J + n\phi_B + \left(\frac{n}{\beta}\right) \ln\left(\frac{J}{A^{**}T^2}\right) \tag{3.44}$$

where

$$\beta = \frac{q}{k_B T} \tag{3.45}$$

Differentiating Eq. 3.44 with respect to J, the first of Cheung's equations is obtained:

$$\frac{dV}{d(\ln J)} = R_S A_{eff} J + \frac{n}{\beta} \tag{3.46}$$

According to Eq. 3.46, a plot of $\frac{dV}{d(\ln J)}$ versus J should yield a straight line (Fig. 3.8), whose slope is n/β and whose intercept with the y-axis is $R_S A_{eff}$.

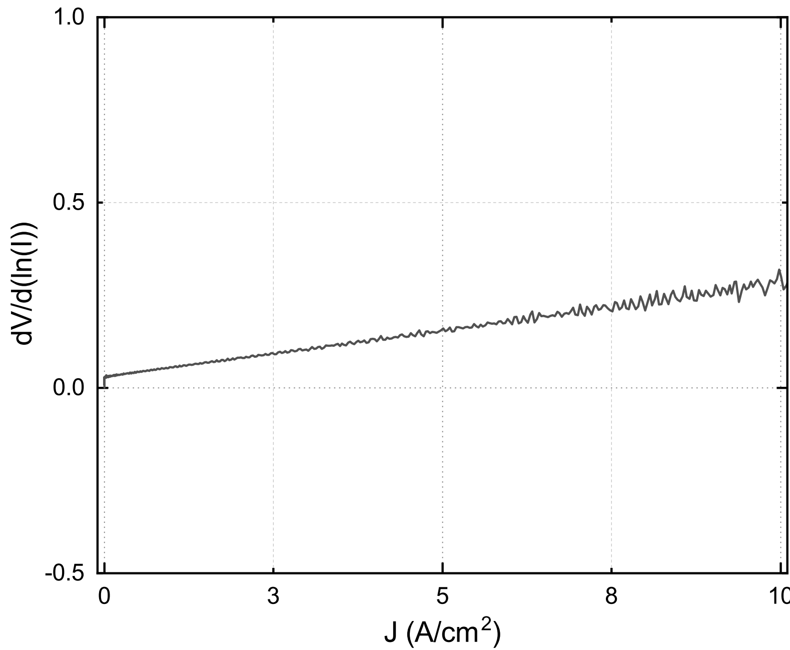

Figure 3.8: Plot of $dV/d(\ln J)$ versus J for the 70 µm diode. From the linear fit, $n = 1.2$ and $R_S^1 = 639.74\,\Omega$

In order to extract also the barrier height ϕ_B, an auxiliary function (the second Cheung's equation) is needed:

$$H(J) \equiv V - \left(\frac{n}{\beta}\right) \ln\left(\frac{J}{A^{**}T^2}\right) \tag{3.47}$$

With the help of Eq. 3.46, Eq. 3.47 can be rewritten as:

$$H(J) = R_S A_{eff} J + n\phi_B \tag{3.48}$$

Using the n value obtained from Eq. 3.46, a plot of $H(J)$ versus J will also give a straight line (Fig. 3.9), whose y-axis intercept and slope are, respectively, $n\phi_B$ and $R_S A_{eff}$. The two values of the series resistance R_S obtained from the two linear fits can be used as a measure of the accuracy of these two fit and the overall method (as the two R_S values should give the same result).

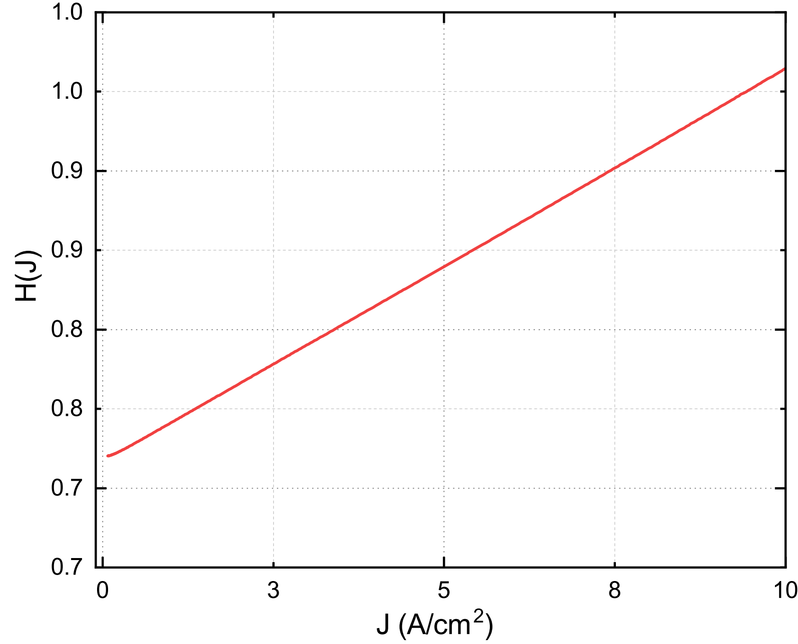

Figure 3.9: Plot of $H(J)$ versus J for the 70 µm diode using the ideality factor extracted previously. From the linear fit, $\phi_B = 0.593\,\text{eV}$ and $R_S^2 = 658.45\,\Omega$, in good agreement with the value of R_S^1

3.2.4 Comparison of methods

The very short list presented above does not include the plethora of method existing in the literature. These go from analytical methods [165, 171–174], to numerical methods [175] and evolutionary algorithms [176, 177].

Among the methods used in this work, it is necessary to take note of the fact that a linear fit of the semi-logarithmic plot of the forward characteristics will be always subjected to human error. In some cases, identifying the linear region before current saturation with absolute accurateness can be ambiguous. Norde method main drawback depends on the fact that a single point is used to extract the relevant parameters and also that it starts with the assumption that the current mechanism of the diode is pure thermionic emission (i.e., $n = 1$). Meanwhile, the modified Norde methods can tackle some of the original method limitations, but may results too convoluted when having to deal with a large number of characteristics. Cheung method is successful in yielding all relevant parameters with just two auxiliary functions. Moreover, the series resistance obtained with this method is in very good agreement with the one obtained from Eq. 3.32.

3.3 IV-T Characterizations

In order to fully comprehend the physical behavior of a Schottky junction, it is absolutely fundamental studying its electrical behavior at different temperatures. The DC characteristics of a real-life Schottky diode is typically composed of contributions from the different current components (such as thermionic emission, tunneling, generation/recombination, leakage due to process defects). The fact that, at different temperatures, the contributions of the different current components may change is a reasonable assumption.

The I-V-T characteristics were measured with an Agilent E5263 2 Channel IV Analyzer / Source Monitor Unit. The temperature was regulated with a Lake Shore Model 332 Temperature Controller.

Fig. 3.10 shows the forward and reverse characteristics measured for the 70 µm GaN on SiC diode between 77–375 K. The extracted values of the barrier height and ideality factor are shown in Fig. 3.11. The barrier height is found to increase with temperature, something that can be attributed to an increase in current due to the increase of temperature. The ideality factor, instead, decreases with temperature. As stated before, since the ideality factor is an empirical measure of how much a Schottky diode forward characteristics represent a thermionic emission characteristics, the reason of the increase of the ideality factor with decreasing temperature may be found in the fact that, at these lower temperatures, other current transport mechanisms, such as tunneling current, may become dominant compared to thermionic emission current [178]. For thermionic emission, the electrons in the metal must have an energy sufficient to overcome the metal/semiconductor barrier. Unlike tunneling current, thermionic emission is extremely sensitive to temperature variations. Eq. 3.15 shows that thermionic emission current varies with the square of temperature. Thus, at high temperatures, electrons in the metal will be very energetic. A reasonable assumption would be that, at low temperatures, thermionic emission current is negligibly small [161] and tunneling is dominant.

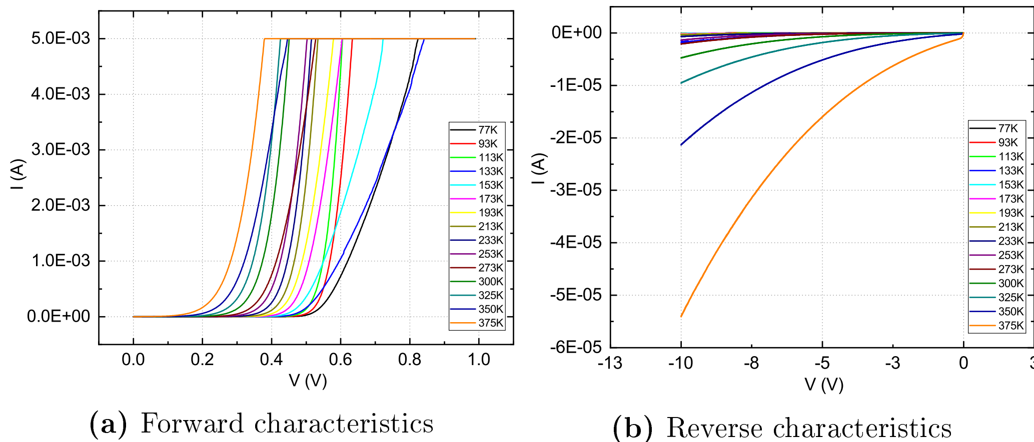

(a) Forward characteristics

(b) Reverse characteristics

Figure 3.10: Experimental DC characteristics for the 70 µm diode taken at temperatures ranging between 77–375 K. A current compliance of 5 mA was used during the measurements in order to avoid premature breakdown

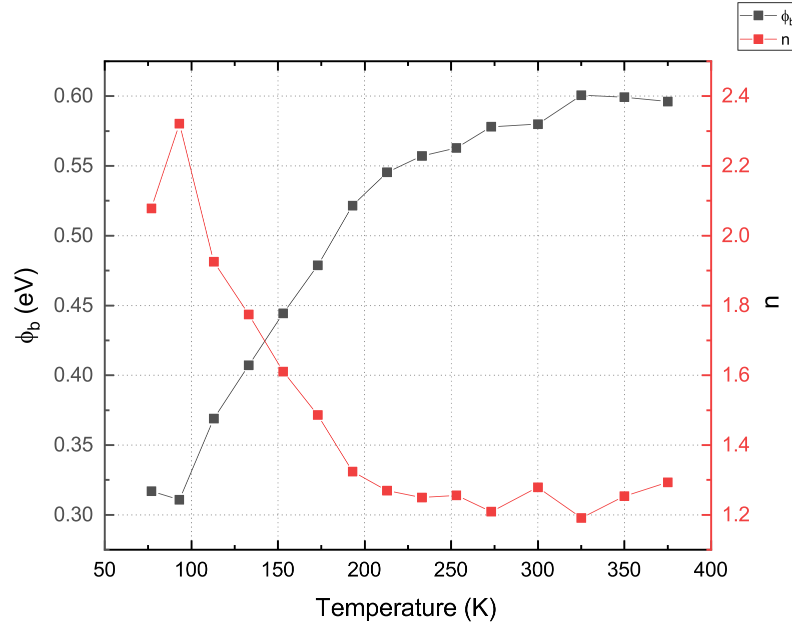

Figure 3.11: Extracted values of ϕ_B and n for the 70 µm diode at different temperatures

By extracting the saturation current at each temperature, it is possible to extract the value of both the effective Richardson constant A^{**} and the barrier height.

The Richardson constant A^* can be counted among the most important parameters in thermionic emission theory fro Schottky diode conduction. Without it, it would be impossible to calculate the barrier height. The usual practice is to assume that the Richardson constant, for a given semiconductor, can be obtained through Eq. 3.8. Therefore, the Richardson constant would be 26.4 A cm^{-2} K^{-2}, given that the effective electron mass for wurtzite GaN is $0.22m_0$ [153]. However, very often the experimentally obtained value for GaN [127, 157, 160, 161, 179–181] differs from the theoretical one. This may be because the theoretical value must be multiplied by factors lower than unity in order to account for the effect of optical phonon scattering and quantum mechanical reflection [182]. Moreover, the heterogeneity of epitaxies, surface conditions prior to metallization, process employed, general interface quality, must be also taken into account when considering this diversity of results

The effective Richardson constant and the barrier height can be extracted from the so-called Richardson plot through the following equation:

$$\ln\left(\frac{J_S}{T^2}\right) = \ln A^{**} - \frac{q\phi_B}{k_B T} \tag{3.49}$$

A typical result can be seen in Fig. 3.12.

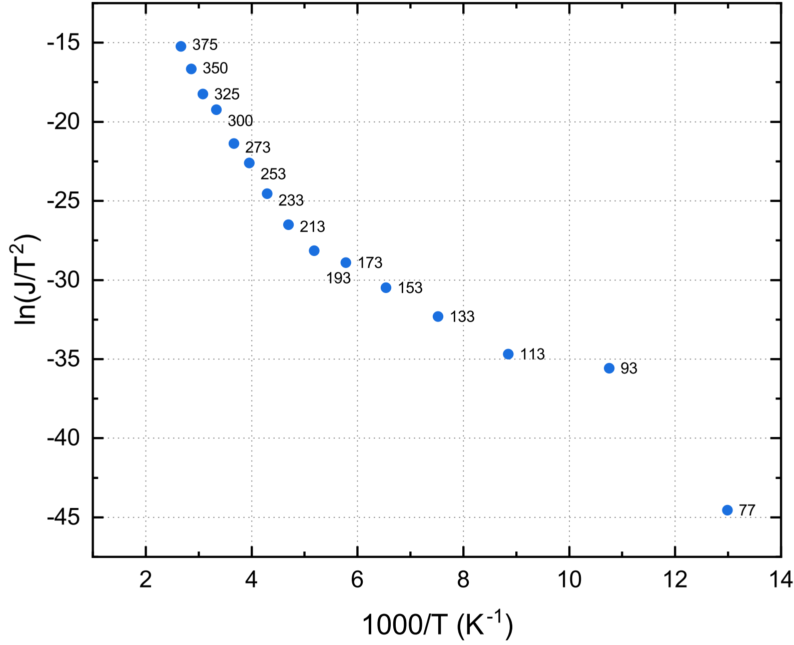

Figure 3.12: Richardson plot for the 70 µm diode. The extracted values are $A^{**} = 0.342\,\mathrm{A\,cm^{-2}\,K^{-2}}$ and $\phi_B = 0.471\,\mathrm{eV}$

3.4 CV Characterizations

An 4294A Precision Impedance Analyzer (40 Hz to 110 MHz) was used to obtain the impedance and phase characteristics of the diode, which were then converted in capacitance and resistance characteristics by considering the implicit diode model of capacitor and resistor in parallel.

The capacitance of a metal-semiconductor junction as a function of voltage is described by [60]:

$$\frac{A^2}{C^2} = \frac{2\left(V_{bi} - V - \frac{k_B T}{q}\right)}{q \varepsilon_S \varepsilon_0 N_d} \tag{3.50}$$

where A is the contact area, V_{bi} is the built-in voltage, V is the applied voltage, N_d is the donor concentration, and ε_0 is the dielectric vacuum constant ($8.854 \cdot 10^{-14}\,\mathrm{F\,cm^{-1}}$).

A plot of C^{-2} vs V should yield a straight line (Fig. 3.13). The carrier concentration can be extracted from the slope of this curve:

$$N_d = \frac{2}{q \varepsilon_0 \varepsilon_S A^2 \frac{dC^{-2}}{dV}} \tag{3.51}$$

From the intercept on the x-axis, the barrier height can be extrapolated:

$$\phi_B = V_x + \frac{k_B T}{q} + \frac{k_B T}{q} \ln\left(\frac{N_c}{N_d}\right) \tag{3.52}$$

where V_x is the x-axis intercept, and N_c is the density of states in the conduction band edge, which for GaN is given by the relation $N_c = 4.3 \cdot 10^{14} \cdot T^{3/2}$.

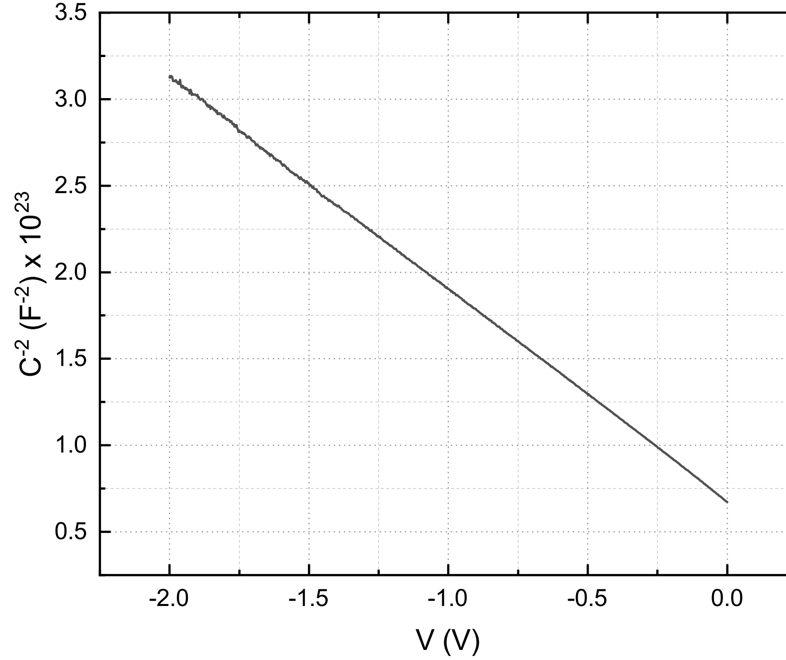

Figure 3.13: Plot of C^{-2} vs V for the 70 µm diode for barrier height extraction. The resulting flat-band barrier height is equal to 0.675 eV, and $N_d = 8.83 \cdot 10^{16}\,\text{cm}^{-3}$

Compared to the Schottky barrier height extracted through DC measurements, the barrier height extracted through the method described in Eq. 3.52 is slightly higher. This is because DC measurements are affected by non-idealities effects (e.g., image-force lowering), that have little if not any effect on CV measurements. In practice, the barrier height extracted through CV measurements is called the flat-band barrier height ϕ_B^{FB}, while the one extracted from DC measurements is called zero-bias barrier height ϕ_B^{ZB}.

CV measurements are typically carried out at a high enough frequency (usually 1 MHz) in order to avoid contributions from traps and/or interface states. In fact, at these frequencies the trap states are unable to respond to the AC signal.

3.5 Small-signal High Frequency Characteristics

The high frequency characteristics of the diodes were obtained with a Vector Network Analyzer (VNA). The measured quantities are S-parameters, which are power ratio of incident, reflected and transmitted signals. The diodes are placed in series between the signal ports. So, S_{12} and S_{21} are expected to provide information about the diode, while S_{11} and S_{22} are affected by parasitic elements at port 1 and port 2, respectively.

An Agilent E8361A PNA network analyzer was used in this work. It has a measurement frequency range that goes from 10 MHz to 67 GHz. The applied bias was controlled with an HP 4142B modular DC source. The devices were measured

between 250 MHz and 67 GHz. A conventional Short, Open, Load, and Through (SOLT) calibration procedure was applied before each measurement.

3.5.1 De-embedding

Devices high frequency measurements are possible through the use of coplanar waveguides in order to access the active region. In order to study the obtained characteristics, it is necessary to remove the effects of the coplanar waveguides, i.e., the parasitic elements associated to them. This process is called de-embedding, and makes use of apposite structures. The de-embedding structures are designed with the same dimension as the device, in order to avoid any discrepancy. The open circuit structure is realized by simply removing from the diode layout every element except the metallic pads. The short circuit structure shorts the signal pad to the ground through bridge fingers.

By measuring these two structures, two set of Y-parameters are obtained: Y_{open} and Y_{short}, respectively for the open and short structure [183]. The actual device under test (DUT) Y-parameters are obtained (after some corrections to the open and short parameters) through:

$$Y_{DUT}^{de-embedded} = \left((Y_{DUT} - Y_{open})^{-1} - (Y_{short} - Y_{open})^{-1}\right)^{-1} \tag{3.53}$$

where Y_{DUT} are the as-measured Y-parameters of the DUT (device and parasitics), and $Y_{DUT}^{de-embedded}$ are the actual DUT Y-parameters.

3.5.2 Junction Capacitance

The junction capacitance is extracted from the imaginary part of Y_{ij} at relatively low frequencies (i.e., < 100 GHz), following a model detailed in [184]. For a high-frequency diode, the capacitances are typically between some tenths and tens of fF. Therefore, in the low frequency range, the diode capacitances are dominant compared to the inductances. Since the inductances in the equivalent circuit can be neglected, the circuit has a π-network topology (Fig. 3.14).

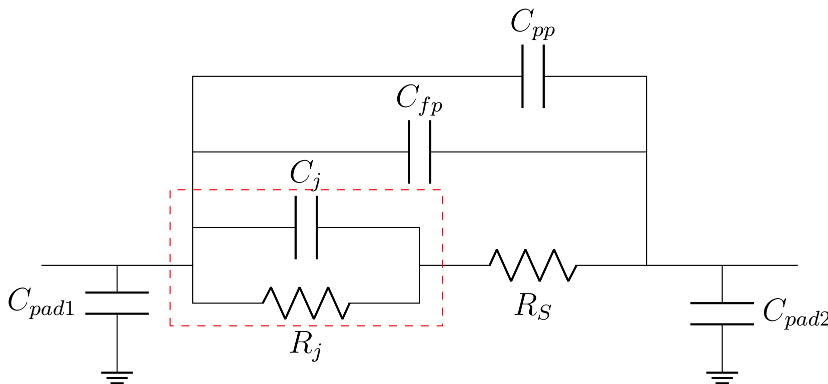

Figure 3.14: Schottky diode equivalent circuit. Highlited in red, the basic Schottky diode model

Since the equivalent circuit is reciprocal, the Y_{12} parameter is sufficient to extract the total capacitance following the equation:

$$C_{tot12}(V) = \frac{Im(-Y_{12}(V))}{\omega} \tag{3.54}$$

An example of the obtained characteristics can be seen in Fig. 3.15.

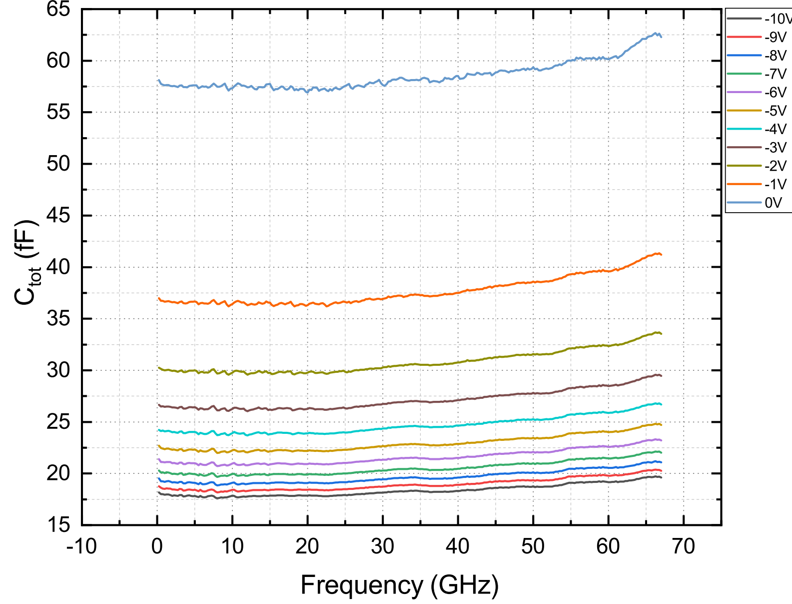

Figure 3.15: Capacitance measurements obtained from S-parameters for an 8 µm diode (GaN on SiC)

By using multiple bias-point in the reverse bias range, the junction capacitance C_j and the parasitic capacitance C_{par} are obtained by fitting the experimentally obtained values of the total capacitance for each bias point (Fig. 3.16) with:

$$C_{tot12}(V) = C_{j0}\left(1 - \frac{V}{V_{bi}}\right)^{-M} + C_{par} \tag{3.55}$$

where C_{j0} is the zero-bias junction capacitance, and M is a parameter representing the doping profile of the semiconductor (for uniformly doped semiconductors, $M = 0.5$). In this work, rather than choosing a single frequency from which to extract the capacitance values at the different bias points from the curves in Fig. 3.15, it was chosen to perform an average on a frequency range were the characteristic were more or less constant. This was done in order to avoid any unwanted deltas at a specific frequency point that could have had a negative influence on the final result. The frequency range chosen was 10–30 GHz.

The parasitic capacitance C_{par} is the sum of the finger-to-pad capacitance C_{fp} and the pad-to-pad capacitance C_{pp}. The diode C_{pp} is estimated from the de-embedding structure with Eq. 3.54 and $C_{tot12}^{de-embed} = C_{pp}^{de-embed}$. The diode finger-to-pad capacitance is then extracted by:

$$C_{fp} = C_{par} - C_{pp}^{de-embed} \tag{3.56}$$

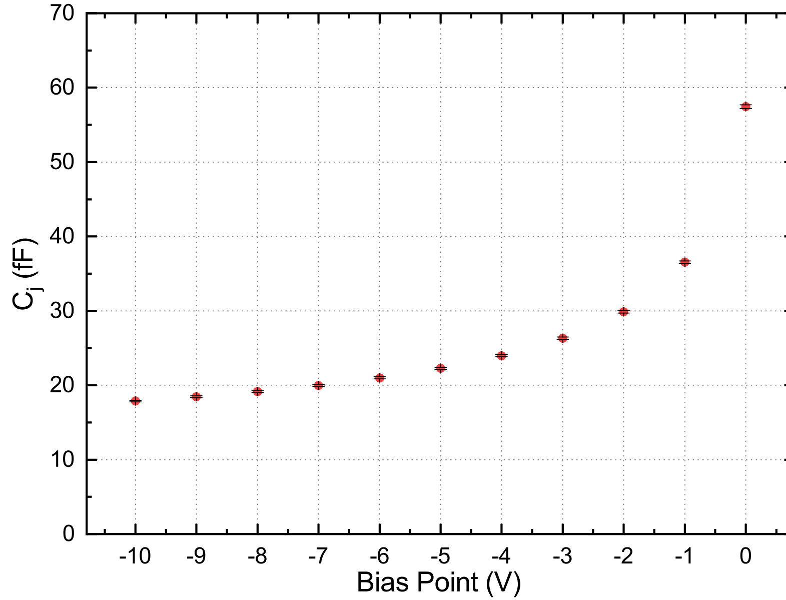

Figure 3.16: Experimentally obtained values of the junction capacitance for the 8 µm diode. By fitting to Eq. 3.55, $C_{j0} = 5.11 \cdot 10^{-14}\,\mathrm{F}$, $C_{par} = 6.3 \cdot 10^{-15}\,\mathrm{F}$, and $V_{bi} = 0.54\,\mathrm{eV}$

In an analogous way, the diode resistance can be calculated in the same low frequency range. The total resistance R_{tot} is extracted keeping mind two fundamental assumptions: R_j is dominating R_S when the diode is reverse-biased, and C_j is negligible when the diode is forward-biased. The total resistance is obtained with:

$$R_{tot}\left(V\right) \approx \frac{1}{Re\left(-Y_{12}\left(V\right)\right)} = R_S + R_j\left(V\right) \tag{3.57}$$

Following Eq. 3.57 and as well the two assumptions, the series resistance is estimated with at least one forward bias point different from the flat band, when the junction resistance is assumed to be zero. The junction resistance is obtained in the reverse bias case.

In this work it was not possible to extract the parasitic inductances, which, by following the same model [184], are extracted at high frequency, i.e. hundreds of gigahertz.

3.6 Results and Discussion

The diodes in this work were fabricated on all three epitaxies using the same E-Beam mask. This mask can be divided in two main parts: the first encompass diodes with diameters ranging between 1400–44.28 µm, having as well the circular TLM patterns; the second part contains smaller diodes, with diameter in the range of 40–0.6 µm, fabricated with air-bridge contact. The first part was used to establish first-order diode characteristics, such as the barrier height and ideality factor, the I-V-T characteristics, and the CV characteristics. The second part was also used for high frequency characterizations, given that these diodes were isolated (as described in Section 2.2.4).

As shown in Fig. 2.1, each of the three epitaxies have different structure. The epitaxies of GaN on sapphire and on silicon are commercial epitaxies, while the epitaxy of GaN on SiC was manufactured by CRHEA laboratory. The process was applied in the same exact way on all three structures except in the case of sapphire: in order to isolate the devices, the sample must be etched down to the semi-insulating layer. Given the important thickness in the case of sapphire, it was not possible to adapt the process of air-bridges to the devices fabricated on GaN on sapphire. Thus, the high frequency characterization will only concern the diodes fabricated on GaN on Si and GaN on SiC.

The protocol of characterization employed was the same for all diodes: for the first part of the mask, the state of the surface was to be considered. This translated in the fact that diodes with large diameter (between 221.3 µm and 1400 µm) yielded, in most cases, sub-par characteristics, not fit to the extraction of relevant parameters. The reason of this behavior may be attributed to the fact that GaN hetero-epitaxial technology suffers of many drawbacks in terms of dislocation defects, misfit and threading dislocations (Section 2.1.2). Therefore, the protocol employed was to measure three representative diodes with diameter of 140 µm, 70 µm, and 44.28 µm. The DC, I-V-T, and CV characterizations were performed. Moreover, the characterizations carried out on these three diodes were the evaluation method used to decided the best surface chemical treatment among the four used (No treatment, HCl, HF, KOH). The best annealing temperature for the Schottky contact was selected by choosing the temperature that corresponded to the highest breakdown voltage in reverse bias. The fundamental Schottky diode parameters, such as barrier height and ideality factor, were extracted through thermionic emission theory and Cheung's method.

For what concerns S-parameters measurements, diodes in two-port configuration were characterized. On the mask, there are such diode with diameters ranging between 40–0.6 µm. However, it was not possible to characterize all of them on each epitaxy. This entirely depends on the fabrication process of air-bridge, in that it was not possible to obtain neither a 100% yield of devices on each sample, neither a constant yield of devices throughout samples. The causes of this behavior may be attributed partly on the specific characteristics of each substrate used in this work.

3.7 Discussion on current conditions

The design and fabrication of a frequency multiplier circuit operating in varactor mode, i.e. using the non-linear capacitance of a Schottky diode, starts with the fundamental parameters of the Schottky diode. The waveguides, loads and matching filtering circuits are all tailored according to the Schottky diode performances. In first instance, the fundamental physical parameters of the diode are the barrier height (ϕ_B), the ideality factor (n), the series resistance (R_S), and the saturation current (I_{sat}). These parameters were extracted from DC forward characteristics using thermionic emission theory (as described in Section 3.1.3):

$$I = I_{sat}\left[\exp\left(\frac{qV}{nk_BT}\right) - 1\right] \tag{3.58}$$

$$I_{sat} = AA^*T^2\exp\left(-\frac{q\phi_B}{k_BT}\right) \tag{3.59}$$

Most practical diodes are also characterized by a non-negligible series resistance. In order to accurately characterize the effect of the series resistance, Cheung's method (Section 3.2.3) was used, because it takes advantage of a modified thermionic emission model to extract the Schottky diode parameters. Typical DC forward characteristics can be seen in Fig 3.17.

It is apparent from Fig 3.17 that all curves exhibit non-linear behavior at low voltages. In the case of GaN on sapphire (Fig. 3.17a) and GaN on SiC (Fig. 3.17c), it can be seen that there is a small leakage component (typically associated to defect states in the bulk or on the surface [161]) of the current that dominates at the early stages. This is represented by the very small knee present at the beginning of the curves. Instead, in the case of GaN on Si (Fig. 3.17b), this knee is much more pronounced: a plausible reason for this behavior may be the contribution (at room temperature) of other types of current components, such as tunneling, which have a lower magnitude on the diodes fabricated on the other two substrates. This, in turn, causes a higher leakage current before the electrons gain enough energy to surmount the barrier and start thermionic emission. The extracted parameters can be seen in Table 3.1 and Table 3.2, respectively representing the parameters extracted through thermionic emission theory and Cheung's method.

Thermionic emission theory fails to consider the effect of series resistance, which is present in virtually all practical diodes. The diode series resistance dominates the current at high voltages and thus affects the linearity of the semi-logarithmic plot of the current versus voltage [185]. In practical terms, the linear part of the plot that is used to extract the parameters will be reduced to a voltage range $3k_BT/q \leq V \ll IR_S$, where the effect of the series resistance can be neglected. The linear range will be even smaller if the diode is characterized by a low barrier height.

The approach of Cheung [170] allows, with a single I-V measurement, to evaluate the Schottky barrier height, the ideality factor, and the series resistance, through the use of two auxiliary functions (as detailed in Section 3.2.3). In particular, the two auxiliary functions yield two values of the series resistance that can be used to evaluate the goodness of the two linear fit performed to extract the parameters. These two

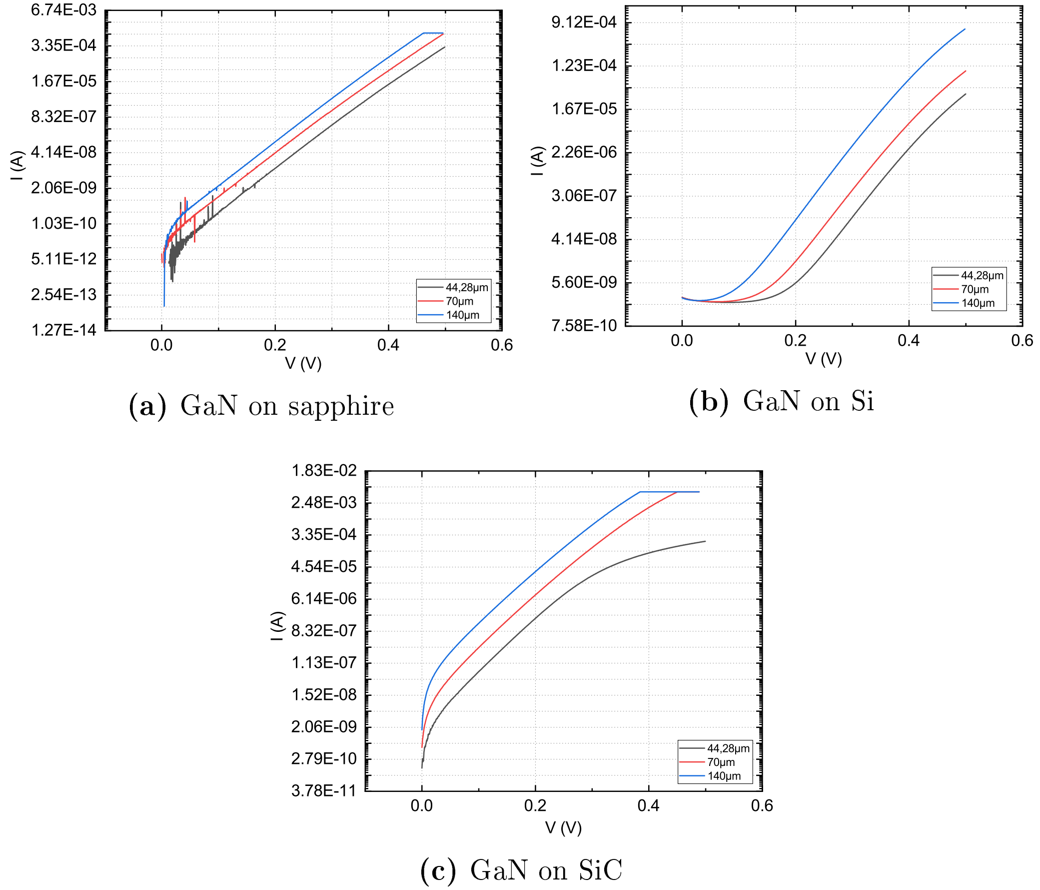

(a) GaN on sapphire

(b) GaN on Si

(c) GaN on SiC

Figure 3.17: Typical DC characteristics for the three diode measured (140 µm, 70 µm, 44.28 µm in diameter) on each substrate. The characteristics were measured between 0 V and 0.5 V with a current compliance of 1 mA

Substrate	d (µm)	ϕ_B (eV)	n	R_S (Ω)	I_{sat} (A)
Sapphire	140	0.749	1.092	2.67	$9.14 \cdot 10^{-11}$
Sapphire	70	0.724	1.152	1.17	$6.01 \cdot 10^{-11}$
Sapphire	44.28	0.727	1.161	7.88	$2.03 \cdot 10^{-11}$
Si	140	0.743	1.144	27.73	$1.15 \cdot 10^{-10}$
Si	70	0.742	1.227	67.12	$2.90 \cdot 10^{-11}$
Si	44.28	0.752	1.219	491.76	$8.12 \cdot 10^{-12}$
SiC	140	0.580	1.233	2.51	$6.27 \cdot 10^{-8}$
SiC	70	0.580	1.279	4.31	$1.55 \cdot 10^{-8}$
SiC	44.28	0.385	3.167	2.36	$1.17 \cdot 10^{-5}$

Table 3.1: Schottky diode extracted parameters with thermionic emission theory

Substrate	d (µm)	ϕ_B (eV)	n	R_S^1 (Ω)	R_S^2 (Ω)
Sapphire	140	0.729	1.154	1.85	1.08
Sapphire	70	0.715	1.178	3.06	3.04
Sapphire	44.28	0.706	1.226	3.53	3.64
Si	140	0.692	1.358	28.19	28.19
Si	70	0.658	1.613	86.01	85.49
Si	44.28	0.582	2.154	132.47	129.87
SiC	140	0.559	1.370	2.61	2.68
SiC	70	0.555	1.410	4.82	4.76
SiC	44.28	0.420	2.375	2.52	2.53

Table 3.2: Schottky diode extracted parameters with Cheung's method

linear functions give less uncertainty than the linear fit used in thermionic emission theory to extract the diode parameters. This translates in more trustworthy results when the linearity of the $ln\,(I)$ vs V curve is dubious. For instance, in the case of the Schottky diodes fabricated on GaN on Si, the values of the barrier height and ideality factor extracted with thermionic emission theory range, respectively, between 0.743–0.752 eV and 1.144–1.227. The diodes are also characterized by a relatively high series resistance that increase with decreasing contact area. An ideality factor greater than unity and a high series resistance are both elements that suggest a significant non-ideal behavior of the I-V curve. However, by using Cheung's method, the barrier height for the same diodes is evaluated ranging between 0.582–0.692 eV and the ideality factor between 1.358–2.154. Furthermore, the results for series resistance deviate for the diodes with diameter of 70 µm and 44.28 µm. It is safe to say at this point that, in the case of highly non-ideal Schottky diode, the extraction of parameters operated with thermionic emission theory may induce unwanted errors, in this case an overestimation of the barrier height and the series resistance, with an underestimation of the ideality factor. This depends predominantly on the chosen range of linearity of the $ln\,(I)$ vs V plot used to extract the parameters. By comparing the extracted parameters for the Schottky diodes fabricated on GaN on sapphire instead, it seems that the two sets of data have a good degree of agreement. This can be a clear indicator that these diodes have a near-ideal behavior, i.e. the main current conduction mechanism is indeed thermionic emission. Moreover, their series resistance is extremely low when compared to other GaN on sapphire Schottky diodes in the literature [158, 161, 186, 187]. The same could be said for the Schottky diodes fabricated on GaN on SiC, although they demonstrated a lower homogeneity in terms of extracted parameters compared to those of GaN on sapphire.

The results presented in Table 3.1 and Table 3.2 are representative of each epitaxy used in this work. GaN on sapphire epitaxy yielded the highest degree of results reproducibility in terms of Schottky diode parameters, followed by GaN on SiC. GaN on Si yielded the highest degree of heterogeneity of results from device to

device compared to the other two epitaxies. The reason of this behavior may be found in the peculiar characteristics of each heteroepitaxy and in the structure of the epitaxies used in this work. Sapphire has a large lattice constant mismatch with GaN ($\sim 15\%$) and a high dislocation density ($10^{10}\,\mathrm{cm}^{-2}$) [93]. The active layer used for the Schottky contact has a relatively low thickness (650 nm) when compared to other examples in the literature [158, 179, 188]. However, the semiconductor surface was characterized by a very low surface roughness. This translated in the good reproducibility from diode to diode of the extracted parameters. Silicon carbide has the smallest lattice constant mismatch ($\sim 3.1\%$) [94], although a relatively large density of defects may still be present. This fact becomes clear when looking at the parameters extracted for the GaN on SiC diode with diameter of 44.28 µm. Its barrier height and ideality factor are, respectively, much lower and much higher than the ones extracted from the other two diodes. Nonetheless, the series resistance is in good agreement with the other two values. A possible reason for this discrepancy is the presence of dislocation defects on the semiconductor surface that induce more leakage current causing other current conduction mechanisms, such as trap-assisted tunneling, to be comparable to thermionic emission. Therefore, for the SiC substrate used in this work, the presence of outliers such as the one described may have several causes, among which probably the presence of defects on the semiconductor surface. Lastly, the fact that silicon is, by far, the poorest substrate for GaN in terms of lattice constant mismatch (-16.9% [189]), considered alongside the relatively low thickness of the active layer used in this work (500 nm), is reflected in the extracted Schottky diode parameters, which are below par compared to the other extracted results especially in terms of series resistance.

The above qualitatively comparison of the results obtained from the Schottky diodes fabricated in this work must not be considered absolute but relative. In fact, a direct comparison between results obtained from different epitaxies may assume scientific value when these epitaxies are fabricated from a single supplier and share common characteristics, such as method of growth, precursors, geometry and doping. The epitaxies used in this work have different suppliers and, moreover, have completely different structures, as detailed above. Thus, the peculiar differences proper of each type of substrate used in this work are further increased.

In Section 3.8, it was shown that the chemical surface treatments used in this work influenced the breakdown voltage of the Schottky diodes. In the case of GaN on sapphire the breakdown voltage was greatly reduced, perhaps because of the presence of contaminant and/or an increased surface roughness. In the case of GaN on Si and GaN on SiC, the same treatments produced different effects, such as a mild improvement (HCl treatment on GaN on Si) and a lower worsening of the breakdown voltage. However, thermal annealing of the Schottky contact was responsible for the dramatic improvement of the breakdown voltage. In order to obtain a more complete picture of the effects produced by the chemical surface treatments and the Schottky contact annealing (at the best conditions), a study of the Schottky contact parameters was performed. Meaningful insights can be gained by analyzing the parameters of the GaN on SiC Schottky diode with diameter of 140 µm. The extracted diode parameters before Schottky contact annealing can be seen in Table 3.3.

As it can be seen from the data in Table 3.3, the chemical surface treatments do not seem to have a significant impact on the diode characteristics, safe for a significant

Treatment	ϕ_B (eV)	n	R_S (Ω)	I_{sat} (A)
No treatment	0.392	1.165	15.72	$8.92 \cdot 10^{-5}$
HCl	0.391	1.942	63.91	$9.28 \cdot 10^{-5}$
HF	0.384	1.536	25.81	$1.20 \cdot 10^{-4}$
KOH	0.453	1.750	67.48	$8.49 \cdot 10^{-6}$

Table 3.3: Extracted Schottky diode parameters for a GaN on SiC diode with diameter of 140 µm for all chemical surface treatments used in this work before Schottky contact annealing

increase in series resistance for HCl and KOH treatment and a slight increase for HF treatment. An increase in series resistance may mean that the semiconductor surface became more resistive. Such a behavior can be explained by looking at the data obtained through XPS survey spectra, more specifically to the quantitative analysis of the intensities of the chemical species present on the semiconductor surface (Table 2.4 in Section 2.3.1). KOH surface treatment effectively increased the N_{1s}/Ga_{3d} ratio, when compared to the other surface treatment and the untreated samples. In fact, KOH treatment may result in an increase of the N surface content and a decrease of the Ga surface content [145]. Instead, HF chemical treatment may cause a shift of the Ga_3d peaks toward lower binding energy more close to the valence band maximum which, in turn, may result in an increased Schottky contact resistance [143]. However, this type of shift was not observed for the Ga_3d peaks obtained from the XPS analysis in this work, except for the HF-treated GaN on SiC sample, which exhibited a shift an all peaks of the spectrum, attributable to charging effects of the surface.

Schottky contact annealing was then performed at 400 °C for 5 min (with a rate of temperature increase between room temperature and annealing temperature of 5 °C/s). The extracted diode parameters after Schottky contact annealing (for the same diodes of Table 3.3) can be seen in Table 3.4.

Treatment	ϕ_B (eV)	n	R_S (Ω)	I_{sat} (A)
No treatment	0.769	1.058	5.48	$4.15 \cdot 10^{-11}$
HCl	0.592	1.113	17.16	$3.82 \cdot 10^{-8}$
HF	0.615	1.140	17.78	$1.62 \cdot 10^{-8}$
KOH	0.594	1.175	14.79	$3.63 \cdot 10^{-8}$

Table 3.4: Extracted Schottky diode parameters for a GaN on SiC diode with diameter of 140 µm for all chemical surface treatments used in this work after Schottky contact annealing at 400 °C for 5 min with a rate of temperature increase between room and annealing temperature of 5 °C/s

The thermal annealing operated improved the barrier height for all chemical treat-

ments. The ideality factor underwent a general improvement and this can suggest that the thermal annealing acted directly on the metal/semiconductor interface in terms of structural reorganization. This might also be an explanation to the reduction of the series resistance for the untreated sample and for all the treated sample, although the latter have a higher series resistance compared to the untreated sample. A possible explanation for this behavior might be the formation of intermetallic compounds between the Schottky contact metal, GaN, and any eventual contaminant species present on the semiconductor surface [146]. In Section 2.3 it was said that HF is effective in removing C contaminants, but leaves F contamination [138]. Cl and K contaminants are as well present, respectively for HCl and KOH treatments. This might have promoted the formation of an intermetallic compound characterized by a lower enthalpy of formation and with higher resistivity.

The room temperature analysis of the Schottky diodes and relative extraction of parameters discussed above gives important and fundamental information. However, it does not provide detailed knowledge about the current mechanisms. Temperature dependent current voltage measurements is an effective tool in terms of characterization of the transport mechanism at the metal/semiconductor junction. Experimentally, by using I-V-T measurements, the effective Schottky barrier height and the effective Richardson constant can be extracted with the so-called Richardson plot. In the ideal case, a Schottky diode is governed by pure thermionic emission. Thus, the Richardson plot, generated by plotting $ln\left(\frac{I_{sat}}{AT^2}\right)$ versus T^{-1} should exhibit total linearity on the entire temperature range. However, for many real Schottky diodes, several deviations from the ideal behavior have been reported [127, 155, 186, 190]. These deviations concern the Richardson constant too. In fact, the experimental Richardson constant, extracted through Richardson plot, is found to be far lower than its theoretical value in many instances (especially for GaN: [129, 157, 160, 161, 179, 191, 192]).

Experimental I-V-T curves for a Schottky diode fabricated on GaN on Si with a diameter of 70 µm can be seen in Fig. 3.18. The extracted Schottky diode parameters can be seen in Table 3.5 and in Fig. 3.19.

From the curves in Fig. 3.18 it is evident that, starting from the curves measured at 325 K and 300 K, there is a small shoulder at low voltages, just before the linear part of the curve. The voltage range of this shoulder gradually increases as the temperature decrease. The presence of this shoulder is plausibly explained by the fact that, at lower voltage, leakage dominates the current. This leakage current originates from defect states in the bulk and/or at the semiconductor surface. Thus, epitaxial defects may enhance the leakage and recombination in real Schottky diodes; all diodes may have a thin insulating interfacial layer, unless they are fabricated in vacuum, although the argon etching used before Schottky contact metallization should have minimized this possibility. After the low voltage shoulder, the slope of the curves differ from temperature to temperature, as it is characteristic for thermionic emission. However, it must be noted that the value of the ideality factor extracted from the DC measurements is already moderately high at 300 K; such ideality factor (1.644 with Cheung's method) may indicate a high degree of non-ideality which may find its reason in the presence of defects on the semiconductor surface (since the heteroepitaxy of GaN on Si is characterized by the highest lattice mismatch among the three used in this work) that cause an increased leakage

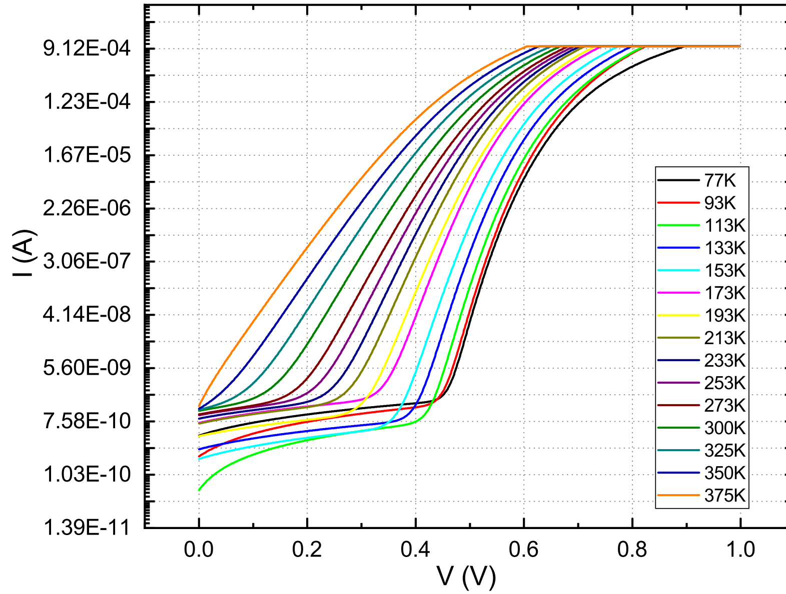

Figure 3.18: Forward characteristics for a GaN on Si Schottky diode with a diameter of 70 µm, taken at temperatures ranging between 77–375 K. A current compliance of 1 mA was used

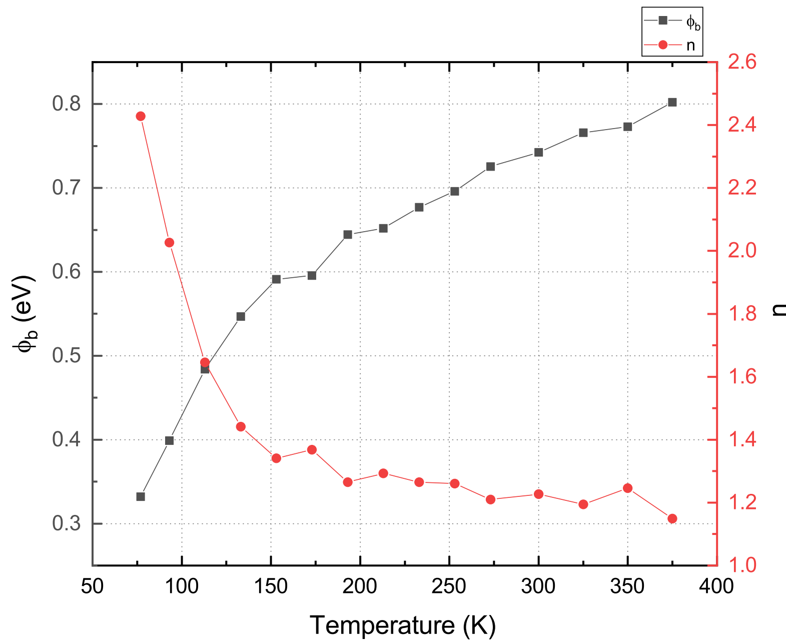

Figure 3.19: Schottky diode parameters for the 70 µm GaN on Si diode for temperatures between 77–375 K

current. Nevertheless, it must also be considered that the ideality factor increase with decreasing temperature, which is also proof that at all temperatures there is at least one other conduction mechanism which is non-negligible [161]. The high density of defect states are most likely the responsible of the initiation of these mechanism. Above the low voltage shoulder, current conduction is dominated by other conduction mechanisms different from leakage. At low temperatures, tunneling current component plausibly is the dominating transport mechanism [155]. Instead, at higher temperatures, thermionic emission and generation-recombination compo-

	TE Fit			Cheung			
T (K)	ϕ_B (eV)	n	R_S (Ω)	ϕ_B (eV)	n	R_S^1 (Ω)	R_S^2 (Ω)
375	0.802	1.149	98.26	0.735	1.497	85.23	81.85
350	0.773	1.246	64.56	0.698	1.603	76.39	75.87
325	0.766	1.195	67.06	0.672	1.644	80.81	80.29
300	0.742	1.227	67.12	0.658	1.613	86.01	85.49
273	0.725	1.210	62.67	0.594	1.852	69.90	69.64
253	0.696	1.261	67.05	0.560	1.956	68.34	68.86
233	0.677	1.265	64.10	0.538	1.982	72.24	71.98
213	0.652	1.293	62.25	0.500	2.127	68.34	68.60
193	0.644	1.265	64.33	0.476	2.190	75.10	75.10
173	0.596	1.368	63.44	0.407	2.663	68.08	68.86
153	0.591	1.341	62.62	0.382	2.808	79.51	78.21
133	0.547	1.442	61.17	0.323	3.436	77.43	75.61
113	0.484	1.646	56.61	0.253	4.750	57.95	57.95
93	0.399	2.027	64.12	0.228	4.892	66.78	67.04
77	0.332	2.428	134.22	0.197	5.454	141.88	141.10

Table 3.5: Extracted parameters for the 70 µm diode of Fig. 3.18

nents dominate the current conduction. Thermionic emission is highly sensitive to temperature. For electrical conduction by thermionic emission, the electrons in the metal must have sufficient energy to overcome the barrier [60]. At higher temperatures, the electrons in the metal become highly energetic. This is clear by looking at Eq. 3.59, which indicates that thermionic emission current is proportional to the square of temperature. At higher temperatures, electrons are more energetic. Electrons with higher energy have higher probability to overcome the Schottky barrier and thus generate current. Generation/recombination in the space-charge region depends more strongly on the intrinsic carrier concentration n_i (Eq 3.13) which has an exponential dependence on temperature:

$$n_i = (N_v N_c)^{\frac{1}{2}} \exp\left(-\frac{E_g}{2k_B T}\right) \tag{3.60}$$

where N_v is the density of states in the valence band, N_c is the density of states in the conduction band, and E_g is the semiconductor bandgap. The exponential term in Eq. 3.60 suggests that the intrinsic carrier concentration, and thus, generation/recombination current, increases rapidly with increasing temperature

3.7.1 Richardson constant

By obtaining the value of the saturation current at each temperature, it is possible to construct Richardson plot by plotting $ln\left(\frac{I_{sat}}{AT^2}\right)$ versus T^{-1}. This plot should exhibit linearity over a range of at least 100 K [60]. Therefore, both the Schottky barrier height ϕ_B and the effective Richardson constant A^{**} can be extracted with the following expression:

$$\ln\left(\frac{I_{sat}}{AT^2}\right) = \ln A^{**} - \frac{q\phi_B}{k_B T} \tag{3.61}$$

A fit performed over the linear temperature range will yield the effective Richardson constant and the barrier height respectively from its slope and intercept. A few examples of experimental Richardson plot for each substrates used in this work can be seen in Fig. 3.20.

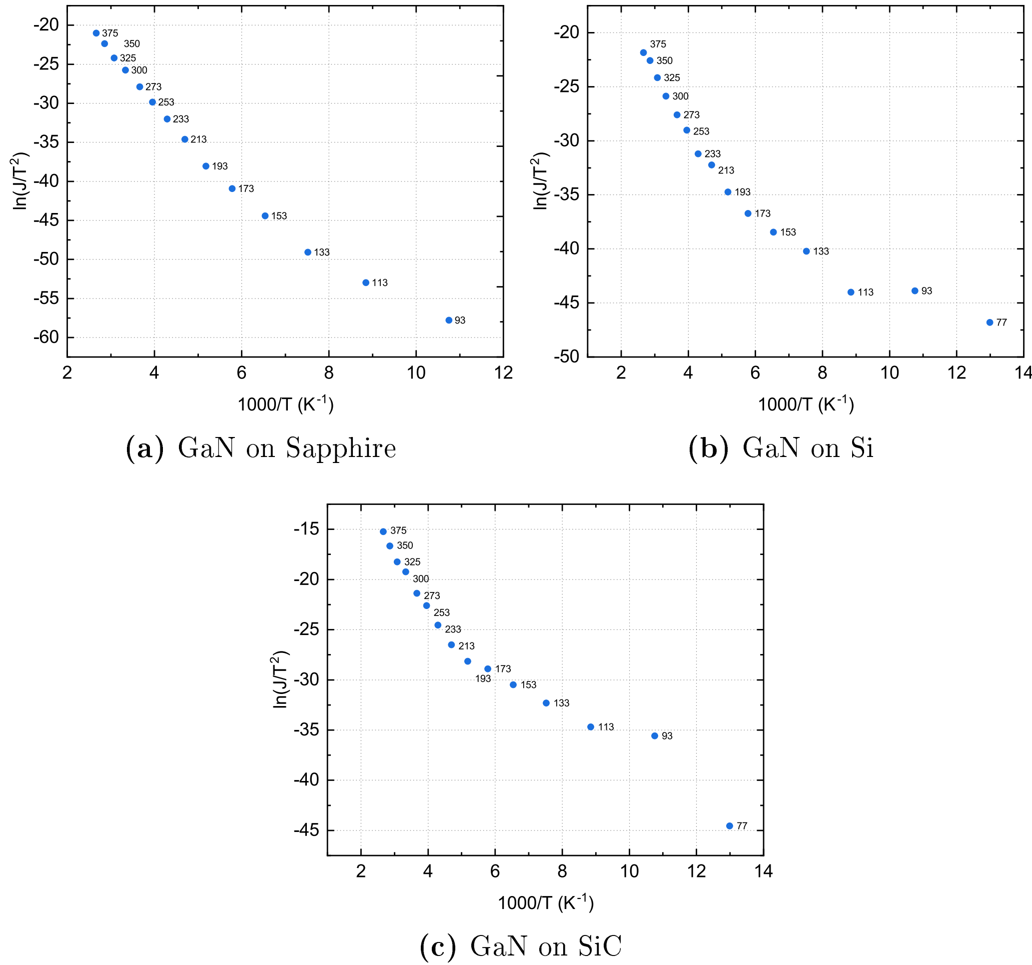

(a) GaN on Sapphire

(b) GaN on Si

(c) GaN on SiC

Figure 3.20: Richardson plot for three selected diodes with diameters of 140 µm (GaN on sapphire), 44.28 µm (GaN on Si), and 70 µm (GaN on SiC)

The extracted effective Richardson constant and barrier height for all the diodes measured between 77 K and 375 K are shown in Table 3.6.

Substrate	d (µm)	A^{**} ($\mathrm{A\,cm^{-2}\,K^{-2}}$)	ϕ_B (eV)
Sapphire	140	0.0347	0.577
Sapphire	70	0.0059	0.518
Sapphire	44.28	0.0065	0.515
Si	140	0.0002	0.434
Si	70	0.0004	0.456
Si	44.28	0.0022	0.505
SiC	140	0.0251	0.393
SiC	70	0.3419	0.471

Table 3.6: Extracted values of the effective Richardson constant and barrier height for the diodes measured between 77–375 K

The diversity of results in the values of the effective Richardson constant extracted from diodes of this work reflect the same diversity present in the literature: Suzue et al. [161] reported a value of $1.094\,\mathrm{A\,cm^{-2}\,K^{-2}}$; Hacke et al. [179] a value of $0.006\,\mathrm{A\,cm^{-2}\,K^{-2}}$, and Khan et al. [193] a value of $0.0092\,\mathrm{A\,cm^{-2}\,K^{-2}}$ (these values are relative to Schottky diodes fabricated on heteroepitaxial GaN on sapphire). This underestimation of the Richardson constant is often associated to the effect of optical phonon and quantum mechanical reflections. Moreover, it must be considered that the choice of the temperature range used to obtain the effective Richardson constant wit Eq. 3.61 directly influences the end result. As stated before, the $ln\left(\frac{I_{sat}}{AT^2}\right)$ versus T^{-1} plot should be linear over at least a range of 100 K [60]. In the case of highly non-ideal Schottky diodes, the linearity range may be reduced or a linear fit might not even be possible (such as for the GaN on SiC Schottky diode with a diameter of 44.28 µm measured in this work). In some other instances, the use of a different model for the extraction of parameters [157, 160, 180, 181, 194] may yield an overestimation of the effective Richardson constant.

In conclusion, the values of the Richardson constant calculated in this work is probably due to tunneling near the semiconductor surface enhanced by defects present at the metal/semiconductor interface [195].

3.8 Breakdown voltage

The power handling of a frequency multiplier is directly related to the maximum voltage amplitude that can be applied across the diode capacitance. The maximum voltage amplitude is defined, in first instance, by the breakdown voltage of the Schottky diode. The breakdown voltage of GaAs is one of the physical factor that represents the bottleneck reached by GaAs-based frequency multiplier technology [74]. Of course, as stated before, GaN presents some disadvantages compared to GaAs (in the context of varactor frequency multiplier technology), such as lower electron mobility and increased series resistance. However, the high breakdown field

represents the main advantage of GaN Schottky diodes.

The theoretical breakdown electric field of GaN is around 3.5 MV/cm. Needless to say, in practice, the value of the breakdown electric field is much lower, because the growth of GaN and its final epitaxial layer is characterized by defects that impact negatively the maximum theoretical value of the breakdown electric field.

In this work, a Schottky contact thermal annealing and chemical surface treatment study was carried out. In first instance, the breakdown voltage was the discriminant, alongside the Schottky diode parameters, used to select the best combination of treatments. The strategy employed differs slightly for each epitaxy used in this work. GaN on sapphire was the first sample studied. The Schottky diodes demonstrated (before any treatment) a breakdown voltage of about 60–70 V, corresponding to a breakdown electric field of circa 1 MV/cm.
Then, the chemical surface treatments were performed before Schottky contact metallization:

- HCl (37%) for 2 min;
- HF (1%) for 30 s;
- KOH at 80 °C for 1 min.

Subsequently, the thermal annealing was performed at 300 °C, 400 °C, 500 °C for 5 min (with a rate of temperature increase between room temperature and annealing temperature of 10 °C/s). The obtained results can be seen in Table 3.7.

	No treatment	HCl	HF	KOH
No annealing	70	22	11	30
300 °C	NA	41.8	17.5	36.8
400 °C	79.2	NA	NA	56.4
500 °C	74.4	49.5	53.9	54

Table 3.7: Absolute value of the breakdown voltage (in V) at the destruction of the GaN on sapphire Schottky diodes for different chemical surface treatments and different annealing temperatures

The breakdown voltage of the treated Schottky diode was much lower than its untreated value. An explanation might be given by the physical characterizations performed to evaluate the effect of surface treatments, namely XPS analysis and AFM scans. XPS analysis did not show any sensible change compared to the untreated sample. However, the AFM scans yielded a significant different root mean squared (rms) surface roughness for HCl and HF treatments, respectively 1.810 nm and 3.423 nm, as compared to the surface roughness of the untreated sample, which was 0.373 nm. This might be one of the reason to the drastic negative change of the breakdown voltage. In some cases it was not even possible to measure a functioning diode. The effect of KOH treatment, instead, might be connected to the increased N_{1s}/Ga_{3d} ratio. Given these considerations on sapphire substrate, another

experiment was devised for Si and SiC substrates. By using the extracted values of the Schottky barrier height and ideality factor of all the treated diodes, it was evident that the major contribution to the improvement of these parameters (with respect to the "non-treated" value) was due to the thermal annealing of the Schottky contact, and that the best values were obtained at 400 °C and 500 °C. Therefore, these two annealing temperatures were applied to samples without surface chemical treatment. The obtained breakdown voltage is, in both cases, around 70–80 V (corresponding to 1.2 MV/cm), however, the sample annealed at 500 °C presents values of the Schottky barrier height and ideality factor that are, respectively, lower and higher compared to the sample annealed at 400 °C.

Based on the experience with the diodes fabricated on GaN on sapphire, the strategy adopted for GaN on Si and GaN on SiC consisted in verifying first the best annealing temperature for the Schottky contact without chemical surface treatment, and then apply that same temperature to all chemical surface treatments. GaN on Si Schottky contact annealing experiments showed that 400 °C was the best annealing temperature in terms of improvement of the breakdown voltage and extracted parameters. In the case of GaN on SiC, the Schottky contact annealing was performed, as usual, at 300 °C, 400 °C, and 500 °C, with a rate of temperature increase of 10 °C/s. However, after careful analysis of the parameters extracted from the characteristics of these diodes, an additional experiment was performed: from the data it was clear that 400 °C was the best annealing temperature among the three employed (with a breakdown voltage for the untreated sample between 60–70 V). Consequently, a sample was annealed at 400 °C but, differently from before, a rate of temperature increase of 5 °C/s was employed. This yielded a more homogeneous sample in terms of breakdown voltage and extracted parameters. The results are listed in Table 3.8.

	GaN on Si		GaN on SiC	
Annealing	Before	After	Before	After
No treatment	27	48.5	32.6	69.5
HCl	29.4	47	32.2	61.6
HF	24.5	48	28.2	66.5
KOH	16.8	45.5	23.8	53.4

Table 3.8: Absolute value of the breakdown voltage (in V) at the destruction of GaN on Si and GaN on SiC Schottky diode, for each chemical surface treatment before and after Schottky contact annealing at 400 °C (10 °C/s for GaN on Si and 5 °C/s for GaN on SiC)

Among the factors that play a role in determining the breakdown voltage of a given Schottky diode, one of the most important is the reverse leakage current. A simple method in determining the origin of the leakage current is to normalize the diodes reverse current over surface and over perimeter. For instance, by analyzing Fig. 3.21, it is clear that the leakage current normalized versus surface is about the same for all

the diodes (with a surface variation factor of about 400, i.e., a variation of current density by a factor ~ 4), while the normalization with respect to the perimeter (variation factor of about 20, i.e., variation of current density by a factor $\sim 1e2$) shows that non-idealities which could stem from the edge of the diodes do not contribute in a relevant way to the reverse current.

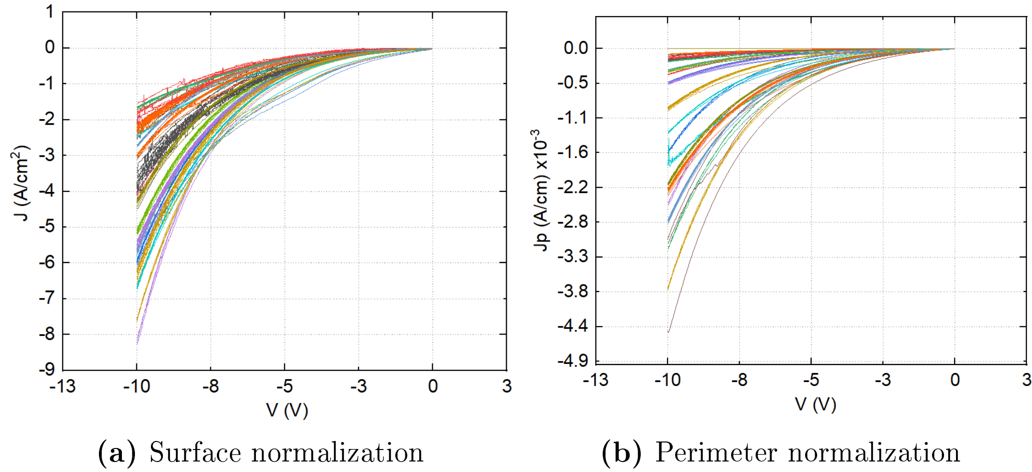

(a) Surface normalization

(b) Perimeter normalization

Figure 3.21: Normalization of the current with respect to surface and perimeter in order to investigate the nature of leakage current. In this case, 23 GaN on Si Schottky diodes with diameters between 2–40 µm were analyzed

In order to limit the reverse leakage current, the surface of the semiconductor must be in its optimum conditions. This means choosing an adequate surface treatment (wet chemical etching, dry etching, or a combination of both). However the calibration of the surface treatment is a difficult and lengthy process, which in practice may be valid for the epitaxy on which it is tested.

Thermal annealing of the Schottky contact plays as well a role in improving the breakdown voltage. The RTA conditions employed in this work (annealing at 400 °C for 5 min, with a rate of temperature increase between room temperature and annealing temperature of 10 °C/s for GaN on sapphire and GaN on Si and 5 °C/s for GaN on SiC) produced a decrease in reverse leakage current and a consequent improvement of the breakdown voltage (Fig. 3.22). This may be attributed to a readjustment process of the metal and semiconductor atoms in its most stable configuration under thermodynamic equilibrium [117, 146].

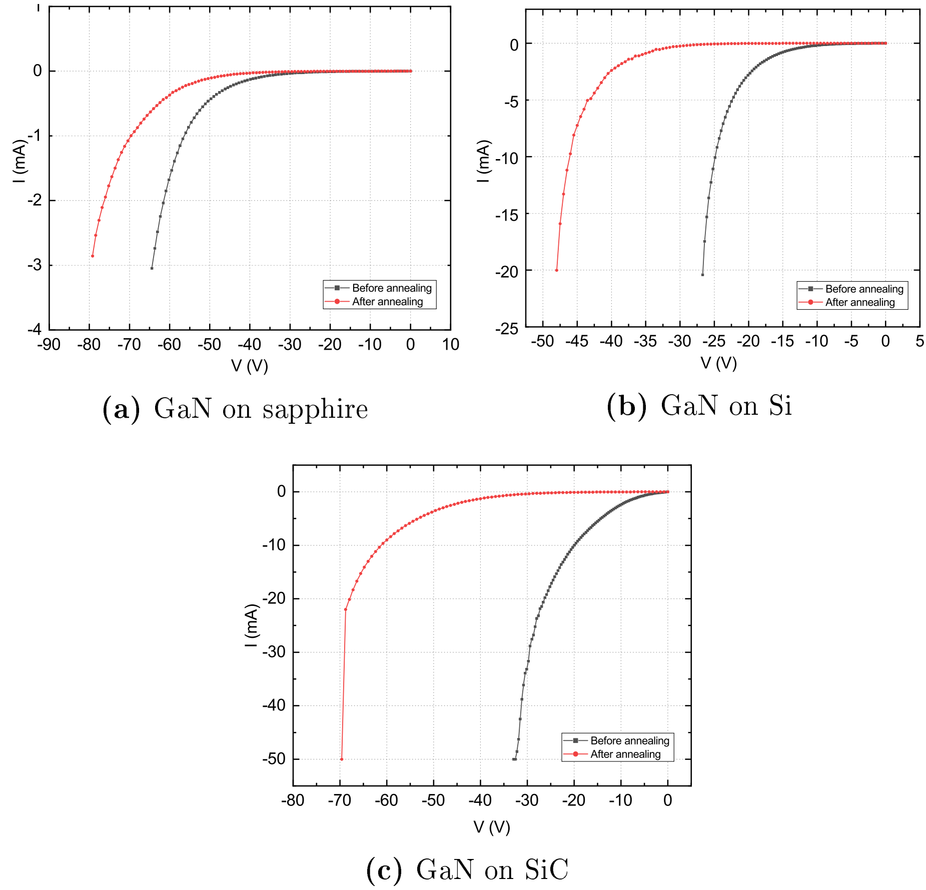

(a) GaN on sapphire

(b) GaN on Si

(c) GaN on SiC

Figure 3.22: Comparison of breakdown voltage of the Schottky diodes fabricated on all three epitaxies used in this work before and after annealing

3.9 Capacitance-voltage behavior

Capacitance voltage measurements are used to study the nature of the depletion region. For a Schottky diode, Eq. 3.50 should be linear if the semiconductor is uniformly doped, and from its slope, the carrier concentration N_d can be extracted.

It must be noted that, sometime, the depletion region of a Schottky diode may contain traps due to crystal defects, or impurities other than the donors. These traps are characterized with energy levels close to the middle of the bandgap and may capture or emit electrons. If an external bias is applied, a change in the occupation of these traps occur. This, in turn, results in a change in the space-charge density and in the depletion width, which translates as a change in capacitance [151]. The capture and emission of electrons from these trap states is characterized by a time constant. A common strategy employed in capacitance measurements is to use a frequency high enough (typically 1 MHz) in order to avoid unwanted contributions of eventual trap states to the diode capacitance. At such frequencies, the trap states are unable to respond to the AC signal.

In this work, the Schottky diodes fabricated on GaN on sapphire and GaN on SiC demonstrated a linear behavior in the C^{-2} vs V plot (Fig. 3.23).

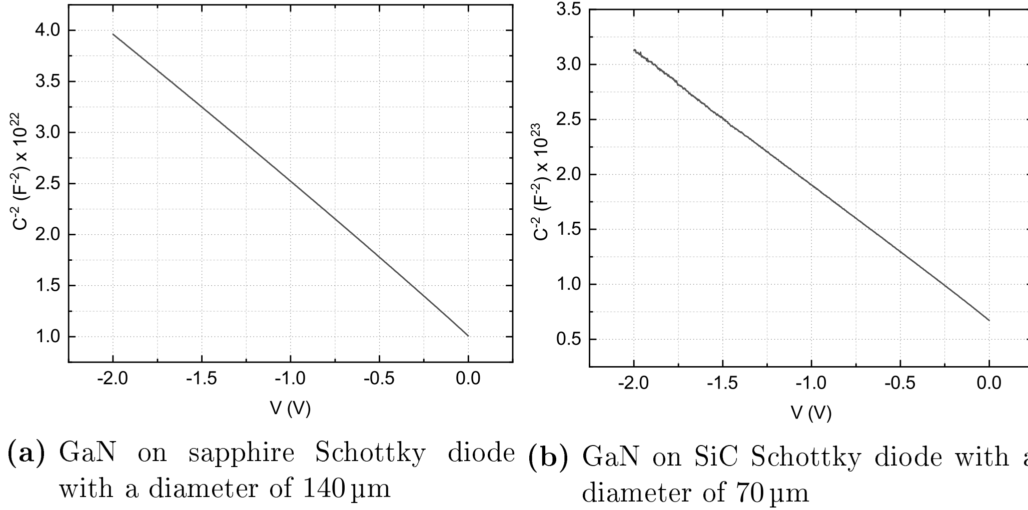

(a) GaN on sapphire Schottky diode with a diameter of 140 µm

(b) GaN on SiC Schottky diode with a diameter of 70 µm

Figure 3.23: C^{-2} vs V plot of Schottky diodes fabricated on GaN on sapphire and on GaN on SiC

By using Eq. 3.51 and Eq. 3.52, the effective doping density and the flat-band barrier height ϕ_B^{FB} were extracted. The results are reported in Table 3.9.

Substrate	d (µm)	ϕ_B (eV)	N_d^{eff} (cm^{-3})	N_d^{theory} (cm^{-3})
Sapphire	140	0.778	$4.42 \cdot 10^{16}$	$5 \cdot 10^{16}$
Sapphire	70	0.861	$4.80 \cdot 10^{16}$	$5 \cdot 10^{16}$
Sapphire	44.28	0.929	$6.77 \cdot 10^{16}$	$5 \cdot 10^{16}$
SiC	140	0.643	$8.40 \cdot 10^{16}$	$6.6 \cdot 10^{16}$
SiC	70	0.673	$8.82 \cdot 10^{16}$	$6.6 \cdot 10^{16}$
SiC	44.28	0.670	$9.62 \cdot 10^{16}$	$6.6 \cdot 10^{16}$

Table 3.9: Schottky diode parameters extracted from CV measurements from selected diodes (after Schottky contact annealing) on sapphire and SiC substrates

The first information that results from the values of the barrier height listed in Table 3.9 is that they seem to be higher compared to the barrier height extracted from DC measurements (the zero bias barrier height ϕ_B^{ZB}) (Table 3.1 and Table 3.2). As explained before, the parameter analysis and extraction from DC characteristics is affected first of all by the imprecision due to the selection of the linear range of the curve. From a physical point of view instead, the zero bias barrier height extracted from the forward characteristic is affected by the image force barrier lowering [151]. This value may ulteriorly be reduced by the effect of a thin insulating layer, charges existing at the metal/semiconductor interface or the effects of possible unoccupied states [196]. The capacitance characterization depends on the nature of the depletion region; thus, the flat-band barrier height is not affected by image-force lowering and

the other non-idealities that lower the value of the zero bias barrier height. It is possible to obtain the zero bias barrier height from the value of the flat-band barrier height and vice-versa from the following relation [197–199]:

$$\phi_B^{FB} = n\phi_B^{ZB} - (n-1)\,\frac{k_B T}{q}\ln\left(\frac{N_c}{N_d}\right) \tag{3.62}$$

The effective doping density extracted from C-V characterizations differs from the nominal value. In the case of GaN on sapphire Schottky diode, the effective doping density values for the diodes with diameter of 140 µm and 70 µm are in good agreement with the nominal value, while for the diode with 44.28 µm is slightly higher. For the GaN on SiC Schottky diodes, the effective doping density is higher than the nominal value. This discrepancy may arises from a possible bad calibration of the growth process, or also to the effect of traps [151, 200, 201]. The density of traps may also be not uniform on the semiconductor surface and depletion region, which explain the outlier behavior of the 44.28 µm GaN on sapphire diode.

An interesting point of view would be to see the effect of the chemical surface treatments on capacitance voltage characteristics. The experimental C^{-2} vs V curves measured on a GaN on SiC Schottky diode with diameter of 70 µm for the different surface treatments are shown in Fig. 3.24

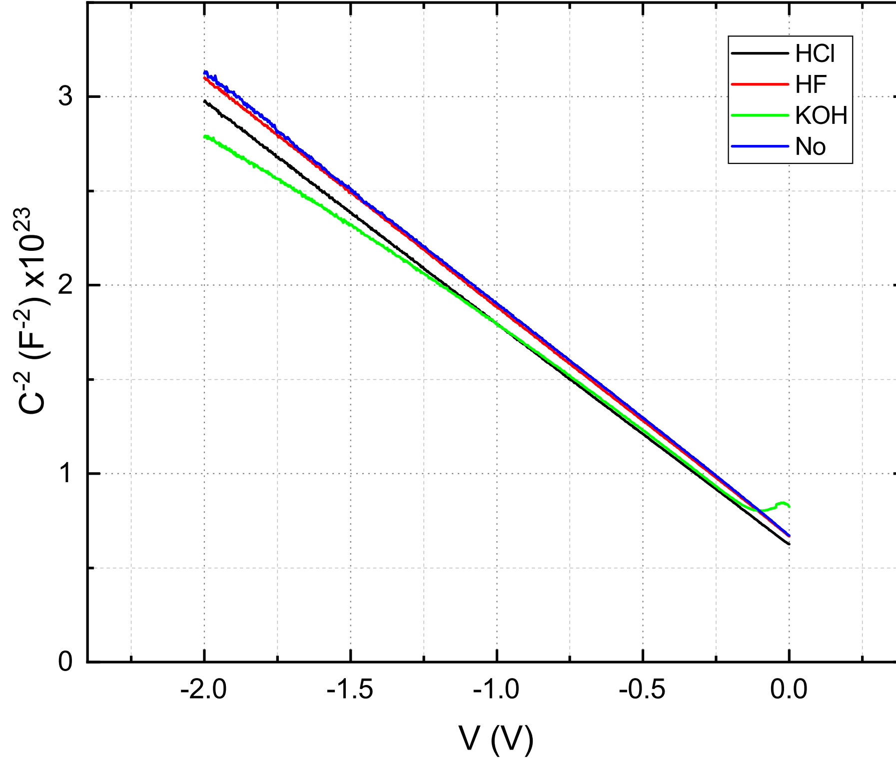

Figure 3.24: C^{-2} vs V curves measured on a GaN on SiC Schottky diode with diameter of 70 µm for the different surface treatments

The extracted parameters are ϕ_B^{FB} =0.673 eV and N_d =$8.82 \cdot 10^{16}$ cm^{-3} for the untreated sample, ϕ_B^{FB} =0.639 eV and N_d =$9.14 \cdot 10^{16}$ cm^{-3} for the HCl-treated sample, ϕ_B^{FB} =0.665 eV and N_d =$8.86 \cdot 10^{16}$ cm^{-3} for the HF-treated sample, and

ϕ_B^{FB} =0.653 eV and N_d =9.17 · 10^{16} cm^{-3} for the KOH-treated sample. Although no visible modification of the surface resulted from XPS analysis and AFM scans, the chemical surface treatments yielded a slight modification of the effective doping density as extracted from C^{-2} vs V characteristics, indicating that the presence of the contaminants introduced and/or the partial removal of C contaminants and oxides had a feeble effect on the surface conditions, although not in a relevant way.

GaN on Si Schottky diodes did not yield a linear C^{-2} vs V characteristics, as it can be seen in Fig. 3.25. This is typically associated with a non-uniform doping profile [60], but there can be multiple reasons for this behavior [202]. For instance, a high density of deep traps in the bulk and/or surface states can be responsible of this non-ideality [203], or the presence of a non-negligible oxide layer at the metal/semiconductor interface [204].

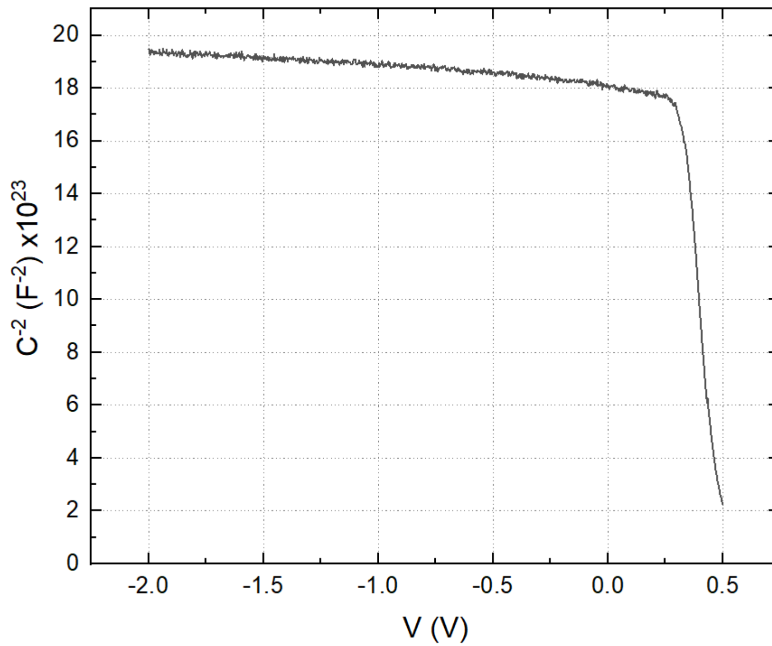

Figure 3.25: C^{-2} vs V curve measured on a GaN on Si Schottky diode with diamater of 44.28 µm

3.10 Small-signal RF Measurements

The main difficulty related to the fabrication of air-bridge Schottky diodes relies in the dry etch of the n^+ GaN layer of each epitaxy down to the RF resistive buffer layer. For the three epitaxies used in this work, the thickness to be etched amounted to around 3 µm for sapphire substrate, given that the u-GaN layer resulted to be conductive, and thus had to be etched alongside the n^+ layer, 500 nm for Si substrate, and 950 nm for SiC substrate. Air-bridge diodes were successfully fabricated on GaN on Si and on GaN on SiC samples, however it was not possible to do the same for GaN on sapphire samples.

The difference in the profile height of the Schottky diodes fabricated on the two epitaxies (GaN on Si and GaN on SiC) produced inconsistencies in terms of final yield of functional devices. For instance, owing to a higher thickness etched, some

of the air-bridges fabricated on GaN on SiC Schottky diodes were characterized by extensive cracks at the connection between bridge finger and metal pads. The same air-bridges did not survive Schottky contact thermal annealing. On the other hand, the yield of devices on the GaN on Si sample was extremely high.

Based on DC characterization results, it was chosen to characterize air-bridge Schottky diodes on the GaN on Si sample with no surface chemical treatment and Schottky contact thermal annealing at 400 °C. For GaN on SiC Schottky diodes instead, it was chosen to characterize the air-bridge Schottky diodes annealed at 400 °C, but for all surface chemical treatments, although it was not possible to measure all diodes for each sample due to the problems relative to the air-bridge fabrication cited above.

The characterization protocol consisted in evaluating the S-parameters between 250 MHz and 67 GHz at specific bias points. The bias points used were taken between −10–1 V. Subsequently, the extracted S-parameters were de-embedded following the procedure detailed in [183]. The S-parameters were then converted in Y-parameter, and the total capacitance was extracted following the model described in Section 3.5.2.

An example of extracted total capacitance can be seen in Fig. 3.26.

The de-embedded curves of the total capacitance are not, at each bias point, exactly constant over the entire frequency range, probably due to the impact of parasitic inductance. Because of this, instead of selecting a single frequency point from which to extract the capacitance values at each bias point on which to perform the non-linear fit described in Section 3.5.2, it was chosen to select a range of frequency, namely 10–30 GHz. Then, for each bias point, the mean of the total capacitance

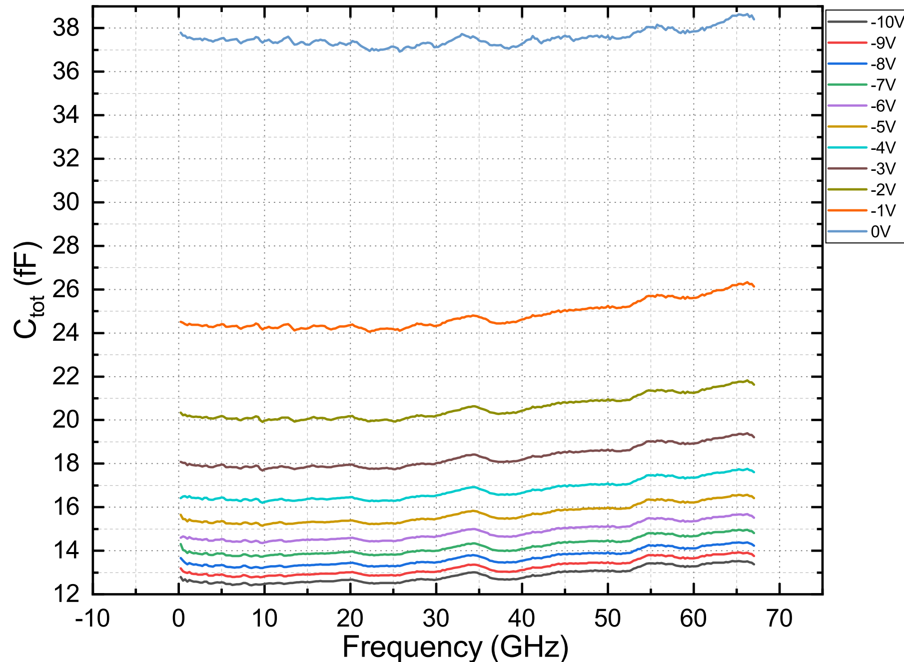

Figure 3.26: Total capacitance as extracted from de-embedded S-parameter measurements of a KOH-treated GaN on SiC diode with diameter of 6 µm

measured in this range was taken as value to use in the non-linear fit along its standard deviation over this range. The resulting curve is shown in Fig. 3.27.

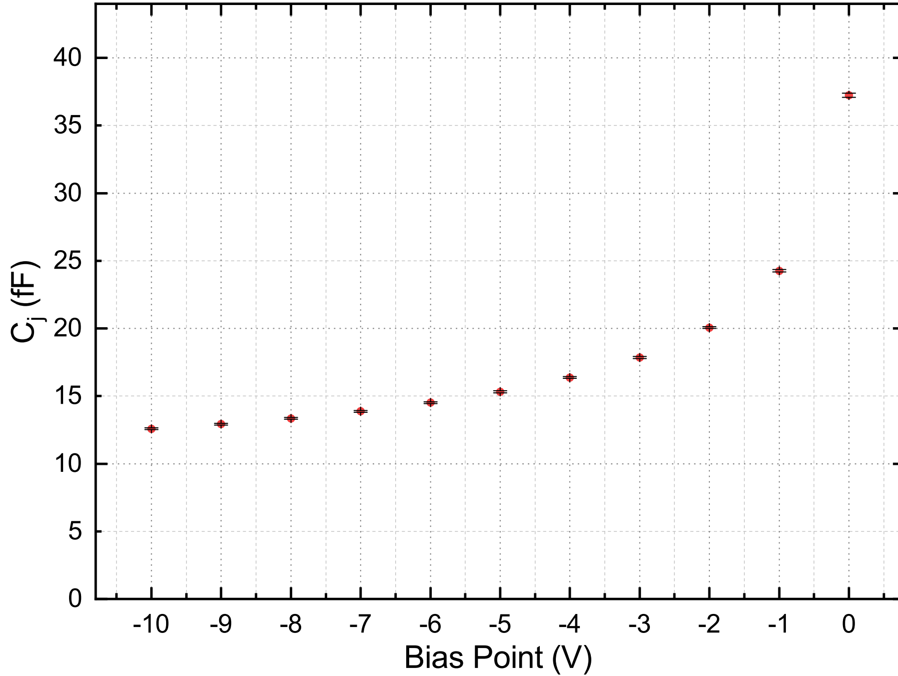

Figure 3.27: Junction capacitance for the 6 µm KOH-treated GaN on SiC diode

As described in Section 3.5.2, the obtained values of Fig. 3.27 were fitted with the following equation:

$$C_j\left(V\right) = C_{j0}\left(1 - \frac{V}{V_{bi}}\right)^{-M} + C_{par} \tag{3.63}$$

where M is a parameter representing the doping profile of the semiconductor, and for uniformly doped semiconductors it is assumed to be $M = 0.5$. The resulting extracted zero-bias junction capacitance C_{j0}, parasitic capacitance C_{par}, and built-in potential V_{bi} for selected diodes are reported in Table 3.10

It must be considered that the non-linear fit with Eq. 3.63 was operated on the entire bias point range when possible; in some instances, the range was reduced in order to reduce the error on the extracted parameters. The principle used was to obtain from the non-linear fit an error on the extracted parameters of at least two order of magnitudes lower than their values.

The parasitic capacitance C_{par} is the sum of the finger-to-pad capacitance C_{fp} and the pad-to-pad capacitance C_{pp}, which was estimated (from the de-embedding structure) to be 1.1 fF for the GaN on SiC epitaxy.

The series resistance of the Schottky diodes is extracted in an analogous way to the junction capacitance, but on forward bias points. Having evaluated the junction capacitance and the series resistance, it is now possible to obtain the Schottky diode

Treatment	d (µm)	C_{j0} (F)	C_{j0}/A (F/cm^2)	C_{par} (F)	V_{bi} (eV)
Untreated	12	$1.30 \cdot 10^{-13}$	$1.15 \cdot 10^{-7}$	$2.15 \cdot 10^{-14}$	0.386
Untreated	8	$5.11 \cdot 10^{-14}$	$1.02 \cdot 10^{-7}$	$6.30 \cdot 10^{-15}$	0.541
Untreated	6	$2.90 \cdot 10^{-14}$	$1.02 \cdot 10^{-7}$	$5.97 \cdot 10^{-15}$	0.575
HCl	12	$1.29 \cdot 10^{-13}$	$1.14 \cdot 10^{-7}$	$5.64 \cdot 10^{-14}$	0.107
HCl	1.2	$1.08 \cdot 10^{-15}$	$9.59 \cdot 10^{-8}$	$3.73 \cdot 10^{-15}$	1.088
HF	8	$5.43 \cdot 10^{-14}$	$1.08 \cdot 10^{-7}$	$6.26 \cdot 10^{-15}$	0.543
HF	6	$3.08 \cdot 10^{-14}$	$1.09 \cdot 10^{-7}$	$5.40 \cdot 10^{-15}$	0.585
HF	4.8	$2.03 \cdot 10^{-14}$	$1.12 \cdot 10^{-7}$	$5.07 \cdot 10^{-15}$	0.600
HF	4	$1.22 \cdot 10^{-14}$	$9.70 \cdot 10^{-8}$	$4.14 \cdot 10^{-15}$	0.721
KOH	12	$1.50 \cdot 10^{-13}$	$1.33 \cdot 10^{-7}$	$4.95 \cdot 10^{-14}$	0.161
KOH	8	$7.77 \cdot 10^{-14}$	$1.55 \cdot 10^{-7}$	$7.71 \cdot 10^{-15}$	0.646
KOH	6	$3.19 \cdot 10^{-14}$	$1.13 \cdot 10^{-7}$	$5.30 \cdot 10^{-15}$	0.545
KOH	4.8	$2.82 \cdot 10^{-14}$	$1.56 \cdot 10^{-7}$	$9.73 \cdot 10^{-15}$	0.446

Table 3.10: Extracted parameters from high-frequency characterization for selected GaN on SiC Schottky diodes. A normalization over Schottky diode area is presented to offer a comparison between different diodes

cutoff frequency f_c at zero bias, which is defined as:

$$f_c = \frac{1}{2\pi C_{j0} R_S} \tag{3.64}$$

The evaluated cutoff frequency is presented in Table 3.11.

Treatment	d (µm)	C_{j0} (F)	R_S (Ω)	f_c (GHz)
Untreated	12	$1.30 \cdot 10^{-13}$	9.37	130.99
Untreated	8	$5.11 \cdot 10^{-14}$	22.29	139.62
Untreated	6	$2.90 \cdot 10^{-14}$	34.65	158.64
HCl	12	$1.29 \cdot 10^{-13}$	12.57	98.47
HCl	1.2	$1.08 \cdot 10^{-15}$	1820.31	80.60
HF	8	$5.43 \cdot 10^{-14}$	21.25	137.97
HF	6	$3.08 \cdot 10^{-14}$	33.66	153.45
HF	4.8	$2.03 \cdot 10^{-14}$	49.96	157.02
HF	4	$1.22 \cdot 10^{-14}$	80.34	162.49
KOH	12	$1.50 \cdot 10^{-13}$	10.25	130.47
KOH	8	$7.77 \cdot 10^{-14}$	13.36	153.28
KOH	6	$3.19 \cdot 10^{-14}$	33.27	149.80
KOH	4.8	$2.82 \cdot 10^{-14}$	17.36	325.43

Table 3.11: Calculated cutoff frequency for selected GaN on SiC Schottky diodes

Some of the diodes presented in Table 3.11 were further analyzed. In particular, three diodes were selected: an untreated diode with anode diameter of 6 µm, a HF-treated diode with anode diameter of 4 µm, and a KOH-treated diode with anode diameter of 6 µm. Table 3.12 presents the parameters extracted from small-signal high frequency characterization and the calculated cutoff frequency at zero bias for these three diodes, while Fig. 3.28 show a plot of the cutoff frequency versus the voltage calculated, in first approximation with the capacitance value extracted at each bias point and by keeping the series resistance constant.

	d (µm)	C_{j0} (F)	R_S (Ω)	J (A/cm^2)	V_{BD} (V) @1 µA	f_c (GHz)
Untreated	6	29.0	34.7	3.5	−19.3	158.6
HF	4	12.2	80.3	7.9	−38.5	162.5
KOH	6	31.9	33.3	3.5	−27.5	149.8

Table 3.12: Parameters of selected quasi-vertical GaN on SiC diodes with high breakdown voltage @1 µA

The current state of the art for GaN on SiC Schottky diodes is represented by a breakdown voltage of −15.4 V for an anode diameter of 5 µm [82], and a breakdown voltage of −19.5 V for anode diameters of 6.5 and 4.5 µm [205].
The three diodes analyzed here demonstrated a breakdown voltage of −19.3 V for

the untreated diode with diameter of 6 µm, −27.5 V for the KOH-treated diode with diameter 6 µm, and −38.5 V for the 4 µm HF-treated diode, showing improvement compared to the most recent reported values.

At zero bias, the cutoff frequency is 158.6 GHz, 149.8 GHz, and 162.5 GHz, respectively for the untreated, KOH-treated, and HF-treated diode. The fact that these values are low compared to the literature (e.g., 459 GHz from [82, 205]) is probably due to the high value of the series resistance.

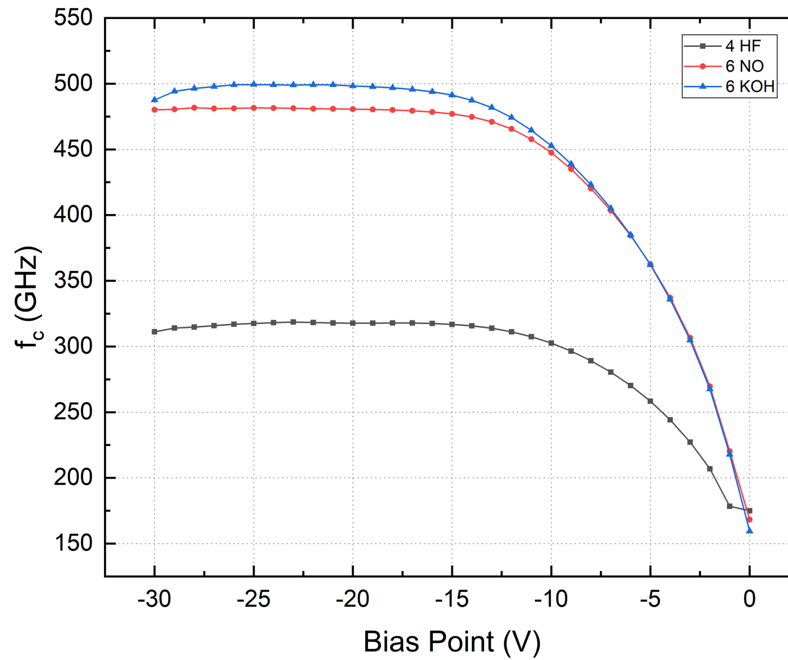

Figure 3.28: Cutoff frequency versus voltage for selected quasi-vertical GaN on SiC diodes

In principle, higher operation frequency is possible for diodes with smaller diameter, and, consequently, smaller area. One of the bottleneck of GaN frequency multiplier technology compared to the GaAs frequency multiplier state of the art is in fact the higher value of the series resistance, which directly impact the power handling capabilities of the frequency multiplier and, overall, its efficiency. Previously reported works in the literature demonstrated a cutoff frequency (at zero bias) of 902 GHz for an anode diameter of 2 µm [81], and 655 GHz for an anode diameter of 5 µm [80], but for GaN on sapphire Schottky diodes. The values of the cutoff frequency presented in this work are lower than the current state of the art, which is probably due to the high series resistance of the diodes. However, there is still room for improvement, by optimizing the fabrication process, the chemical surface treatment, the Schottky contact annealing conditions in order to decrease the value of the series resistance. The optimization of the series resistance is more critical than the junction capacitance, because to a smaller junction capacitance corresponds, in practice, lower power handling capabilities.

Chapter 4

Conclusions and Future Outlook

4.1 Conclusions

A comprehensive study was carried out in order to evaluate quasi-vertical GaN Schottky diode characteristics and performances for frequency multiplier applications, as the next technological step in order to overcome the current state of the art represented by GaAs Schottky diode frequency multipliers. The GaN Schottky diodes were fabricated with the same technological process on three different heteroepitaxies: GaN on sapphire (Al_2O_3), GaN on silicon (Si), and GaN on silicon carbide (SiC).

A short summary of the current state of the art on THz technology was given, with particular attention to THz sources. GaAs Schottky diode frequency multiplier state of the art was presented, along with the reasons and motivations on why GaN is being researched as technological alternative for frequency multiplier applications.

The fabrication process used in this work was detailed in each of its steps. The differences with GaAs Schottky diode fabrication process were described, as well as a brief overview of GaN heteroepitaxy state of the art to highlight the inherent differences between the different substrates used. The explanation was comprehensive of the challenges represented by the fabrication of ohmic and Schottky contacts to GaN. Furthermore, a study of chemical surface treatment before Schottky contact metallization and a Schottky contact thermal annealing study was performed. The investigation of the effects on the Schottky diode parameters consisted in physical characterizations, by means of XPS analysis and AFM scans, and, in the subsequent chapters, in a comparison of the extracted parameters.

The GaN Schottky diodes were evaluated in terms of breakdown voltage, DC characteristics, CV characteristics and small signal equivalent circuit high frequency behavior. Particular attention was dedicated to the analytical methods used to extract Schottky diode parameters. Room temperature DC characterization was used to extract the Schottky diode barrier height, ideality factor and series resistance. I-V-T characterization was useful in understanding how current conditions changed in the diode with respect to temperature. CV characterization was employed to investigate the nature of the depletion region of the semiconductor. Lastly, with S-parameters measurements it was possible to obtain the cut-off frequency of the

diodes.

GaN on sapphire Schottky diode presented the highest breakdown voltage among the diodes analyzed. Moreover, they were characterized by the lowest series resistance, fundamental to the conversion efficiency and to the power handling capabilities of frequency multipliers. However, the epitaxy used in this work was characterized by a large thickness of the n^+ layer, thus the height of the device rendered impossible the fabrication of the air-bridge structures for high frequency studies.

GaN on Si Schottky diodes were characterized by a high degree of heterogeneity in results, the lowest breakdown voltage among the three epitaxies used, and the highest value of the series resistance. The reasons for such a behavior might be brought back to the inherent problematic that hetero-epitaxy of GaN on Si has, such as a high lattice constant mismatch and high thermal expansion coefficient difference.

GaN on SiC Schottky diodes yielded a good breakdown voltage, almost comparable to that of GaN on sapphire. The extracted Schottky diode parameters demonstrated a good degree of homogeneity. The extracted values of the cut-off frequency from air-bridge diode were lower than the current state of the art but, nonetheless, justify future interest in this type of technology

4.2 Future outlook and perspective

The final goal is to produce the next technological step in frequency multipliers for THz generation, and this can be done by finding a candidate to replace GaAs Schottky diodes. GaN has all the necessary characteristics to overcome the physical limitations of GaAs. In theory, one GaN Schottky diode should be equivalent, in terms of input power handling, to eight GaAs diodes of similar area [74]. However, some challenges must be addressed.

One critical point is the state of the art of hetero-epitaxial growth of GaN on a foreign substrate, which heavily affects GaN electrical properties. The inherent limitations given by the chosen substrate transmit to the critical parameters of the Schottky diodes for frequency multiplication. Moreover, the relationship between donor doping concentration and epitaxial layer thickness is still not clear, specifically in the ways it might impact the Schottky diode parameters. Homo-epitaxial GaN should be investigated as well, although, as of now, its prohibitive cost and availability limit the investigation in this direction. And above all, the reproducibility of a given hetero-epitaxial process is not guaranteed.

Another key point concerns the fabrication process, more specifically the optimization of surface conditions. An accurate, systematic, and comprehensive study of the effect of chemical surface treatment should be carried out in order to intimately understand the effect on the Schottky diode performances. The fact that the epitaxial growth of GaN is not a standard process effectively hinders this direction, since any kind of study of this type would be valid only for the epitaxy on which it is conducted, although it might yield some relative information applicable in other cases. Always from the point of view of the fabrication process, a study of different metals as Schottky contact could reveal to be interesting.

The above critical points impact directly the Schottky diode series resistance. In fact, this is a crucial parameter that influences the diode cutoff frequency and, ultimately, its power handling capabilities and the frequency multiplier efficiency. In theory, higher frequency operations are possible for diodes with smaller area, but the series resistance increase as the active area of the diode decreases.
This is one of the main detraction to GaN Schottky diode for frequency multiplication. Future research should be focused on global strategy to minimize the series resistance.

Future work will include large-signal on-wafer characterization. This step is necessary to optimize the epi-structure design and device geometry. This will be accompanied by frequency multiplier design simulation based on the experimental Schottky diode parameters.

Bibliography

[1] D. Dragoman and M. Dragoman. "Terahertz fields and applications". In: *Progress in Quantum Electronics* 28.1 (2004), pp. 1–66. DOI: 10.1016/S0079-6727(03)00058-2.

[2] Yun-Shik Lee. *Principles of Terahertz Science and Technology*. Springer Science, 2009.

[3] P.H. Siegel. "Terahertz technology". In: *IEEE Transactions on Microwave Theory and Techniques* 50.3 (2002), pp. 910–928. DOI: 10.1109/22.989974.

[4] David T. Leisawitz et al. "Scientific motivation and technology requirements for the SPIRIT and SPECS far-infrared/submillimeter space interferometers". In: *UV, Optical, and IR Space Telescopes and Instruments*. Ed. by James B. Breckinridge and Peter Jakobsen. Vol. 4013. July 2000. 2000, pp. 36–46. DOI: 10.1117/12.393957.

[5] T.G. Phillips and J. Keene. "Submillimeter astronomy (heterodyne spectroscopy)". In: *Proceedings of the IEEE* 80.11 (1992), pp. 1662–1678. DOI: 10.1109/5.175248.

[6] Peter H. Siegel. "THz Instruments for Space". In: *IEEE Transactions on Antennas and Propagation* 55.11 (2007), pp. 2957–2965. DOI: 10.1109/TAP.2007.908557.

[7] Gary J Melnick et al. "The Submillimeter Wave Astronomy Satellite: Science Objectives and Instrument Description". In: *The Astrophysical Journal* 539.2 (2000), pp. L77–L85. DOI: 10.1086/312856.

[8] G. L. Pilbratt et al. "Herschel Space Observatory". In: *Astronomy and Astrophysics* 518.7-8 (2010). DOI: 10.1051/0004-6361/201014759.

[9] David T. Leisawitz et al. "SPECS: the kilometer-baseline far-IR interferometer in NASA's space science roadmap". In: *Optical, Infrared, and Millimeter Space Telescopes* 5487.October (2004), p. 1527. DOI: 10.1117/12.552150.

[10] Samuel Gulkis et al. "Remote sensing of a comet at millimeter and submillimeter wavelengths from an orbiting spacecraft". In: *Planetary and Space Science* 55.9 (2007), pp. 1050–1057. DOI: 10.1016/j.pss.2006.11.011.

[11] Ho Jin Song and Tadao Nagatsuma. "Present and future of terahertz communications". In: *IEEE Transactions on Terahertz Science and Technology* 1.1 (2011), pp. 256–263. DOI: 10.1109/TTHZ.2011.2159552.

[12] Steven Cherry. "Edholm's law of bandwidth". In: *IEEE Spectrum* 41.7 (2003), pp. 58–60. DOI: 10.1109/MSPEC.2004.1309810.

[13] Thomas Kleine-Ostmann and Tadao Nagatsuma. "A review on terahertz communications research". In: *Journal of Infrared, Millimeter, and Terahertz Waves* 32.2 (2011), pp. 143–171. DOI: 10.1007/s10762-010-9758-1.

[14] Guillaume Ducournau et al. "THz Communications using Photonics and Electronic Devices: the Race to Data-Rate". In: *Journal of Infrared, Millimeter, and Terahertz Waves* 36.2 (2015), pp. 198–220. DOI: 10.1007/s10762-014-0112-x.

[15] John Federici and Lothar Moeller. "Review of terahertz and subterahertz wireless communications". In: *Journal of Applied Physics* 107.11 (2010). DOI: 10.1063/1.3386413.

[16] Hai Bo Liu et al. "Terahertz spectroscopy and imaging for defense and security applications". In: *Proceedings of the IEEE* 95.8 (2007), pp. 1514–1527. DOI: 10.1109/JPROC.2007.898903.

[17] Dwight L Woolard et al. "Terahertz Frequency Sensing and Imaging : A Time of Reckoning Future Applications ?" In: 93.10 (2005).

[18] John F. Federici et al. "THz imaging and sensing for security applications - Explosives, weapons and drugs". In: *Semiconductor Science and Technology* 20.7 (2005). DOI: 10.1088/0268-1242/20/7/018.

[19] Michael C. Kemp et al. "Security applications of terahertz technology". In: *Terahertz for Military and Security Applications* 5070.August (2003), p. 44. DOI: 10.1117/12.500491.

[20] William R. Tribe et al. "Hidden object detection: security applications of terahertz technology". In: *Terahertz and Gigahertz Electronics and Photonics III* 5354.April 2004 (2004), p. 168. DOI: 10.1117/12.543049.

[21] Roger Appleby and H Bruce Wallace. "Standoff Detection of Weapons and Contraband in the 100 GHz to 1 THz Region". In: 55.11 (2007), pp. 2944–2956.

[22] X. C. Zhang and Jingzhou Xu. *Introduction to THz wave photonics*. 2010, pp. 1–246. DOI: 10.1007/978-1-4419-0978-7.

[23] Hua Zhong et al. "Terahertz wave imaging for landmine detection". In: *Terahertz for Military and Security Applications II* 5411.September 2004 (2004), p. 33. DOI: 10.1117/12.540502.

[24] Carter M. Armstrong. "The truth about terahertz". In: *IEEE Spectrum* 49.9 (2012), pp. 36–41. DOI: 10.1109/MSPEC.2012.6281131.

[25] Peter H Siegel. "Terahertz Technology in Biology and Medicine". In: 52.10 (2004), pp. 2438–2447.

[26] Samuel P. Mickan et al. "Label-free bioaffinity detection using terahertz technology". In: (2002), pp. 3789–3795. DOI: 10.1088/0031-9155/47/21/317.

[27] P. Haring Bolivar et al. "Label-free probing of genes by time-domain terahertz sensing". In: (2002), pp. 3815–3821. DOI: 10.1088/0031-9155/47/21/320.

[28] Goutam Chattopadhyay. "Technology, Capabilities, and Performance of Low Power Terahertz Sources". In: *IEEE Transactions on Terahertz Science and Technology* 1.1 (2011), pp. 33–53. DOI: 10.1109/TTHZ.2011.2159561.

[29] Tadao Nagatsuma and Hiroshi Ito. "High-Power RF Uni-Traveling-Carrier Photodiodes (UTC-PDs) and Their Applications". In: *Advances in Photodiodes*. Ed. by Gian Franco Dalla Betta. Rijeka: IntechOpen, 2011. Chap. 14. DOI: 10.5772/14800.

[30] Tadao Nagatsuma et al. "High-power RF photodiodes and their applications". In: *Laser and Photonics Reviews* 3.1-2 (2009), pp. 123–137. DOI: 10.1002/lpor.200810024.

[31] G. Ducournau et al. "Coherent THz communication at 200 GHz using a frequency comb, UTC-PD and electronic detection". In: *Electronics Letters* 50.5 (2014), pp. 386–388. DOI: 10.1049/el.2014.0056.

[32] Serge Luryi. "Frequency limit of double-barrier resonant-tunneling oscillators". In: *Applied Physics Letters* 47.5 (1985), pp. 490–492.

[33] Masahiro Asada et al. "Resonant tunneling diodes for sub-terahertz and terahertz oscillators". In: *Japanese Journal of Applied Physics* 47.6R (2008), p. 4375.

[34] Safumi Suzuki et al. "Fundamental oscillation of resonant tunneling diodes above 1 THz at room temperature". In: *Applied Physics Letters* 97.24 (2010), p. 242102.

[35] Michael Feiginov et al. "Resonant-tunnelling-diode oscillators operating at frequencies above 1.1 THz". In: *Applied Physics Letters* 99.23 (2011). DOI: 10.1063/1.3667191.

[36] Takeru Maekawa et al. "Oscillation up to 1.92 THz in resonant tunneling diode by reduced conduction loss". In: *Applied Physics Express* 9.2 (2016). DOI: 10.7567/APEX.9.024101.

[37] Federico Capasso et al. "Quantum cascade lasers". In: *Physics Today* 55.5 (2002), pp. 34–39. DOI: 10.1063/1.1485582.

[38] Jerome Faist et al. "Quantum Cascade Laser". In: *Science* 264.5158 (1994), pp. 553–556. DOI: 10.1126/science.264.5158.553.

[39] Rudeger Kohler et al. "Terahertz semiconductor-heterostructure laser". In: *Nature* 417.6885 (2002), pp. 156–159.

[40] Benjamin S Williams et al. "Terahertz quantum-cascade laser at $\lambda = 100\ \mu$ m using metal waveguide for mode confinement". In: *Applied Physics Letters* 83.11 (2003), pp. 2124–2126.

[41] Benjamin S Williams. "Terahertz quantum cascade lasers". In: *Asia Optical Fiber Communication and Optoelectronic Exposition and Conference*. Optical Society of America. 2008, SuG3.

[42] P Khosropanah et al. "3.4 THz heterodyne receiver using a hot electron bolometer and a distributed feedback quantum cascade laser". In: *Journal of Applied Physics* 104.11 (2008), p. 113106.

[43] Juraj Darmo et al. "Imaging with a Terahertz quantum cascade laser". In: *Optics express* 12.9 (2004), pp. 1879–1884.

[44] Alain Maestrini. "Frequency multipliers for local oscillators at THz frequencies". In: *4th ESA Workshop on Millimetre Wave Technology and Applications* (2006), pp. 1–6.

[45] Alain Maestrini et al. "Schottky diode-based terahertz frequency multipliers and mixers". In: *Comptes Rendus Physique* 11.7-8 (2010), pp. 480–495. DOI: 10.1016/j.crhy.2010.05.002.

[46] Imran Mehdi et al. "THz Diode Technology: Status, Prospects, and Applications". In: *Proceedings of the IEEE* 105.6 (2017), pp. 990–1007. DOI: 10.1109/JPROC.2017.2650235.

[47] E. Schlecht et al. "200, 400 and 800 GHz Schottky diode "substrateless" multipliers: design and results". In: *2001 IEEE MTT-S International Microwave Sympsoium Digest (Cat. No.01CH37157)*. Vol. 3. IEEE, 2001, pp. 1649–1652. DOI: 10.1109/MWSYM.2001.967221.

[48] M.T. Faber et al. *Microwave and Millimeter-wave Diode Frequency Multipliers.* Artech House, 1995.

[49] Alain Maestrini et al. "A 1.7-1.9 THz local oscillator source". In: *IEEE Microwave and Wireless Components Letters* 14.6 (2004), pp. 253–255. DOI: 10.1109/LMWC.2004.828027.

[50] Goutam Chattopadhyay et al. "An all-solid-state broad-band frequency multiplier chain at 1500 GHz". In: *IEEE Transactions on Microwave Theory and Techniques* 52.5 (2004), pp. 1538–1547. DOI: 10.1109/TMTT.2004.827042.

[51] Alain Maestrini et al. "Local oscillator chain for 1.55 to 1.75 THz with 100-μW peak power". In: *IEEE Microwave and Wireless Components Letters* 15.12 (2005), pp. 871–873. DOI: 10.1109/LMWC.2005.859989.

[52] Frank Maiwald et al. "Terahertz frequency multiplier chains based on planar Schottky diodes". In: *Millimeter and Submillimeter Detectors for Astronomy* 4855.February 2003 (2003), p. 447. DOI: 10.1117/12.459355.

[53] J.T. Louhi et al. "Cooled Schottky varactor frequency multipliers at submillimeter wavelengths". In: *IEEE Transactions on Microwave Theory and Techniques* 41.4 (1993), pp. 565–571. DOI: 10.1109/22.231647.

[54] Alain Maestrini et al. "Design and characterization of a room temperature all-solid-state electronic source tunable from 2.48 to 2.75 THz". In: *IEEE Transactions on Terahertz Science and Technology* 2.2 (2012), pp. 177–185. DOI: 10.1109/TTHZ.2012.2183740.

[55] Neal R. Erickson. "Diode frequency multipliers for terahertz local-oscillator applications". In: *Advanced Technology MMW, Radio, and Terahertz Telescopes.* Ed. by Thomas G. Phillips. Vol. 3357. July 1998. 1998, pp. 75–84. DOI: 10.1117/12.317407.

[56] L. Liu and J. H. Edgar. "Substrates for gallium nitride epitaxy". In: *Materials Science and Engineering: R: Reports* 37.3 (2002), pp. 61–128. DOI: 10.1016/S0927-796X(02)00008-6.

[57] S. J. Pearton et al. "Fabrication and performance of GaN electronic devices". In: *Materials Science and Engineering R: Reports* 30.3-6 (2000), pp. 55–212. DOI: 10.1016/S0927-796X(00)00028-0.

[58] S. J. Pearton et al. "GaN: Processing, defects, and devices". In: *Journal of Applied Physics* 86.1 (1999), pp. 1–78. DOI: 10.1063/1.371145.

[59] Shuji Nakamura and Gerhard Fasol. *The Blue Laser Diode.* Berlin, Heidelberg: Springer Berlin Heidelberg, 1997. DOI: 10.1007/978-3-662-03462-0.

[60] S.M. Sze and Kwok K. Ng. *Physics of Semiconductor Devices.* Hoboken, NJ, USA: John Wiley & Sons, Inc., 2006. DOI: 10.1002/0470068329.

[61] Hiroshi Amano et al. "P-Type Conduction in Mg-Doped GaN Treated with Low-Energy Electron Beam Irradiation (LEEBI)". In: *Japanese Journal of Applied Physics* 28.Part 2, No. 12 (1989), pp. L2112–L2114. DOI: 10.1143/JJAP.28.L2112.

[62] S. Bloom. "Band structures of GaN and AIN". In: *Journal of Physics and Chemistry of Solids* 32.9 (1971), pp. 2027–2032. DOI: 10.1016/S0022-3697(71)80379-7.

[63] WC Johnson. "JB Parsons, and MC Crew". In: *J. Phys. Chem* 36 (1932), p. 2561.

[64] Ahmad Hassan et al. "A GaN-Based Wireless Monitoring System for High-Temperature Applications". In: *Sensors* 19.8 (2019), p. 1785. DOI: 10.3390/s19081785.

[65] Bejoy N. Pushpakaran et al. "Commercial GaN-Based Power Electronic Systems: A Review". In: *Journal of Electronic Materials* 49.11 (2020), pp. 6247–6262. DOI: 10.1007/s11664-020-08397-z.

[66] Ahmad Hassan et al. "GaN Integration Technology, an Ideal Candidate for High-Temperature Applications: A Review". In: *IEEE Access* 6 (2018), pp. 78790–78802. DOI: 10.1109/ACCESS.2018.2885285.

[67] Matthias Ralf Werner and Wolfgang R. Fahrner. "Review on materials, microsensors, systems, and devices for high-temperature and harsh-environment applications". In: *IEEE Transactions on Industrial Electronics* 48.2 (2001), pp. 249–257. DOI: 10.1109/41.915402.

[68] John A. Edmond et al. "Blue LEDs, UV photodiodes and high-temperature rectifiers in 6H-SiC". In: *Physica B: Physics of Condensed Matter* 185.1-4 (1993), pp. 453–460. DOI: 10.1016/0921-4526(93)90277-D.

[69] Shuji Nakamura et al. "P-GaN/N-InGaN/N-GaN Double-Heterostructure Blue-Light-Emitting Diodes". In: *Japanese Journal of Applied Physics* 32.Part 2, No.1A/B (1993), pp. L8–L11. DOI: 10.1143/JJAP.32.L8.

[70] Wayne Johnson and Edwin L. Piner. "GaN HEMT Technology". In: *GaN and ZnO-based Materials and Devices*. Ed. by Stephen Pearton. Vol. 156. Springer Series in Materials Science. Berlin, Heidelberg: Springer Berlin Heidelberg, 2012, pp. 209–237. DOI: 10.1007/978-3-642-23521-4.

[71] Miroslaw Kwasny and Zygmunt Mierczyk. "Devices for medical diagnosis with GaN lasers". In: *Laser Technology VII: Applications of Lasers* 5229.October 2003 (2003), p. 104. DOI: 10.1117/12.520614.

[72] José V. Siles and Jesús Grajal. "Physics-based design and optimization of Schottky diode frequency multipliers for terahertz applications". In: *IEEE Transactions on Microwave Theory and Techniques* 58.7 PART 2 (2010), pp. 1933–1942. DOI: 10.1109/TMTT.2010.2050103.

[73] John S. Ward et al. "Tunable broadband frequency-multiplied terahertz sources". In: *33rd International Conference on Infrared and Millimeter Waves and the 16th International Conference on Terahertz Electronics, 2008, IRMMW-THz 2008* (2008), pp. 6–8. DOI: 10.1109/ICIMW.2008.4665437.

[74] José V. Siles and Jesús Grajal. "Capabilities of GaN Schottky Multipliers for LO Power Generation at Millimeter-Wave Bands". In: *Proceedings of the 19th International Symposium on Space Terahertz Technology* April (2008), pp. 28–30.

[75] W.A. Harrison. *Electronic Structure and the Properties of Solids: The Physics of the Chemical Bond*. Dover Book. Dover Publications, 1980.

[76] Jasprit Singh. *Physics of semiconductors and their heterostructures*. New York: McGraw-Hill, 1993, p. 851.

[77] H. Morkoç et al. "Large-band-gap SiC, III-V nitride, and II-VI ZnSe-based semiconductor device technologies". In: *Journal of Applied Physics* 76.3 (1994), pp. 1363–1398. DOI: 10.1063/1.358463.

[78] Shixiong Liang et al. "Terahertz Schottky barrier diodes based on homoepitaxial GaN materials". In: *IRMMW-THz 2015 - 40th International Confer-*

ence on Infrared, Millimeter, and Terahertz Waves (2015). DOI: 10.1109/IRMMW-THz.2015.7327726.

[79] Chong Jin et al. "E-beam fabricated GaN schottky diode: High-frequency and non-linear properties". In: *IEEE MTT-S International Microwave Symposium Digest* (2013). DOI: 10.1109/MWSYM.2013.6697734.

[80] Z H Feng et al. "High-frequency multiplier based on GaN planar Schottky barrier diodes". In: *2016 IEEE MTT-S International Microwave Workshop Series on Advanced Materials and Processes for RF and THz Applications (IMWS-AMP)* 1 (2016), pp. 1–3. DOI: 10.1109/IMWS-AMP.2016.7588336.

[81] Shixiong Liang et al. "GaN planar Schottky barrier diode with cut-off frequency of 902 GHz". In: *Electronics Letters* 52.16 (2016), pp. 1408–1410. DOI: 10.1049/el.2016.1937.

[82] Shixiong Liang et al. "A 177–183 GHz High-Power GaN-Based Frequency Doubler With Over 200 mW Output Power". In: *IEEE Electron Device Letters* 41.5 (2020), pp. 669–672. DOI: 10.1109/LED.2020.2981939.

[83] Walter A Harrison. "Electronic structure and the properties of solids: the physics of the chemical bond". In: *Journal of Molecular Structure* 71 (Feb. 1981), p. 355. DOI: 10.1016/0022-2860(81)85136-8.

[84] I. Adesida et al. "Reactive ion etching of gallium nitride in silicon tetrachloride plasmasa)". In: *Applied Physics Letters* 63.20 (1993), pp. 2777–2779. DOI: 10.1063/1.110331.

[85] I. Adesida et al. "Characteristics of chemically assisted ion beam etching of gallium nitride". In: *Applied Physics Letters* 65.7 (1994), pp. 889–891. DOI: 10.1063/1.112191.

[86] H P Gillis et al. "Low energy electron-enhanced etching of Si(100) in hydrogen/helium direct-current plasma". In: *Applied Physics Letters* 66.19 (1995), pp. 2475–2477. DOI: 10.1063/1.114000.

[87] Y. F. Wu et al. "Bias dependent microwave performance of AlGaN/GaN MODFET's up to 100 V". In: *IEEE Electron Device Letters* 18.6 (1997), pp. 290–292. DOI: 10.1109/55.585362.

[88] Ozgur Aktas et al. "High temperature characteristics of AlGaN/GaN modulation doped field-effect transistors". In: *Applied Physics Letters* 69.25 (1996), pp. 3872–3874. DOI: 10.1063/1.117133.

[89] M. Asif Khan et al. "Temperature activated conductance in GaN/AlGaN heterostructure field effect transistors operating at temperatures up to 300C". In: *Applied Physics Letters* 1083.October 1994 (1995), p. 1083. DOI: 10.1063/1.113579.

[90] J Kumar and C Subramanian. "Liquid Encapsulated Czochralski Growth of Large size Gallium Arsenide and Indium Phosphide Single Crystals and their Characterisation—A Review". In: *IETE Journal of Research* 43.2-3 (1997), pp. 125–130. DOI: 10.1080/03772063.1997.11415971.

[91] Shin'ichi Akai. *Bulk crystal growth technology*. Gordon \& Breach Science Pub, 1989, p. 189.

[92] James W. Garland et al. "Arsenic p-Doping of HgCdTe Grown by Molecular Beam Epitaxy (MBE): A Solved Problem?" In: *Journal of Electronic Materials* 42.11 (2013), pp. 3331–3336. DOI: 10.1007/s11664-013-2739-0.

[93] F. A. Ponce. *Group III Nitride Semiconductor Compounds*. Ed. by Bernard Gil. Clarendon Press, 1998, p.123.

[94] J.H. Edgar et al. *Properties, Processing and Applications of Gallium Nitride and Related Semiconductors*. EMIS datareviews series. INSPEC, 1999.

[95] T. Suski et al. "Optical activation and diffusivity of ion-implanted Zn acceptors in GaN under high-pressure, high-temperature annealing". In: *Journal of Applied Physics* 84.2 (1998), pp. 1155–1157. DOI: 10.1063/1.368118.

[96] S. J. Rosner et al. "Correlation of cathodoluminescence inhomogeneity with microstructural defects in epitaxial GaN grown by metalorganic chemical-vapor deposition". In: *Applied Physics Letters* 70.4 (1997), pp. 420–422. DOI: 10.1063/1.118322.

[97] H P Maruska and J. J. Tietjen. "The preparation and properties of vapor-deposited single-crystalline GaN". In: *Applied Physics Letters* 15.10 (1969), pp. 327–329. DOI: 10.1063/1.1652845.

[98] D. Kotchetkov et al. "Effect of dislocations on thermal conductivity of GaN layers". In: *Applied Physics Letters* 79.26 (2001), pp. 4316–4318. DOI: 10.1063/1.1427153.

[99] Leonid Chernyak et al. "Minority carrier transport in GaN and related materials". In: *Solid-State Electronics* 45.9 (2001), pp. 1687–1702. DOI: 10.1016/S0038-1101(01)00161-7.

[100] Z. Z. Bandić et al. "Minority carrier diffusion length and lifetime in GaN". In: *Applied Physics Letters* 72.24 (1998), pp. 3166–3168. DOI: 10.1063/1.121581.

[101] E. V. Etzkorn and D. R. Clarke. "Cracking of GaN films". In: *Journal of Applied Physics* 89.2 (2001), pp. 1025–1034. DOI: 10.1063/1.1330243.

[102] P. R. Willmott and F. Antoni. "Growth of GaN(0001) thin films on Si(001) by pulsed reactive crossed-beam laser ablation using liquid Ga and N2". In: *Applied Physics Letters* 73.10 (1998), pp. 1394–1396. DOI: 10.1063/1.121955.

[103] U. Rössner et al. "How to induce the epitaxial growth of gallium nitride on Si(001)". In: *Materials Science and Engineering B* 29.1-3 (1995), pp. 74–77. DOI: 10.1016/0921-5107(94)04003-M.

[104] P. Kung et al. "High quality AIN and GaN epilayers grown on (001) sapphire, (100), and (111) silicon substrates". In: *Applied Physics Letters* 66.May (1995), p. 2958. DOI: 10.1063/1.114242.

[105] Lianshan Wang et al. "Wurtzite GaN epitaxial growth on a Si(001) substrate using γ-Al2O3 as an intermediate layer". In: *Applied Physics Letters* 72.1 (1998), pp. 109–111. DOI: 10.1063/1.120660.

[106] S. T. Kim et al. "Relationship between crystallographic orientation and 3.42 eV emission bands in GaN grown by HVPE on Si substrate". In: *Semiconductor Science and Technology* 14.2 (1999), pp. 156–160. DOI: 10.1088/0268-1242/14/2/009.

[107] H. Lahrèche et al. "Buffer free direct growth of GaN on 6H-SiC by metalorganic vapor phase epitaxy". In: *Journal of Applied Physics* 87.1 (2000), pp. 577–583. DOI: 10.1063/1.371902.

[108] Q. Wahab et al. "Influence of epitaxial growth and substrate-induced defects on the breakdown of 4H-SiC Schottky diodes". In: *Applied Physics Letters* 76.19 (2000), pp. 2725–2727. DOI: 10.1063/1.126456.

[109] Zhifang Fan et al. "Very low resistance multilayer Ohmic contact to n-GaN". In: *Applied Physics Letters* 68.12 (1996), pp. 1672–1674. DOI: 10.1063/1.115901.

[110] N. A. Papanicolaou et al. “Reliable Ti/Al and Ti/Al/Ni/Au ohmic contacts to n-type GaN formed by vacuum annealing”. In: *Journal of Vacuum Science and Technology B: Microelectronics and Nanometer Structures* 19.1 (2001), pp. 261–267. DOI: 10.1116/1.1331291.

[111] Abhishek Motayed et al. “Electrical, thermal, and microstructural characteristics of Ti/Al/Ti/Au multilayer Ohmic contacts to n-type GaN”. In: *Journal of Applied Physics* 93.2 (2003), pp. 1087–1094. DOI: 10.1063/1.1528294.

[112] E. F. Chor et al. “Electrical characterization and metallurgical analysis of Pd-containing multilayer contacts on GaN”. In: *Journal of Applied Physics* 90.3 (2001), pp. 1242–1249. DOI: 10.1063/1.1383977.

[113] Z. M. Zhao et al. “Ti/Al/Pt/Au and Al ohmic contacts on Si-substrated GaN”. In: *Applied Physics Letters* 79.2 (2001), pp. 218–220. DOI: 10.1063/1.1385189.

[114] Ching-ting Lee and Hsiao-wei Kao. “Long-term thermal stability of Ti/Al/Pt/Au Ohmic contacts to n -type GaN”. In: *Applied Physics Letters* 76.17 (2000), pp. 2364–2366. DOI: 10.1063/1.126347.

[115] V. Kumar et al. “Thermally-stable low-resistance Ti/Al/Mo/Au multilayer ohmic contacts on n-GaN”. In: *Journal of Applied Physics* 92.3 (2002), pp. 1712–1714. DOI: 10.1063/1.1491584.

[116] K. O. Schweitz et al. “V/Al/Pt/Au Ohmic contact to n-AlGaN/GaN heterostructures”. In: *Applied Physics Letters* 80.11 (2002), pp. 1954–1956. DOI: 10.1063/1.1459768.

[117] Q. Z. Liu and S. S. Lau. “A review of the metal-GaN contact technology”. In: *Solid-State Electronics* 42.5 (1998), pp. 677–691. DOI: 10.1016/S0038-1101(98)00099-9.

[118] David W Jenkins and John D Dow. “Electronic structures and doping of InN, In x Ga 1- x N, and In x Al 1- x N”. In: *Physical Review B* 39.5 (1989), pp. 3317–3329. DOI: 10.1103/PhysRevB.39.3317.

[119] Tosja K. Zywietz et al. “The adsorption of oxygen at GaN surfaces”. In: *Applied Physics Letters* 74.12 (1999), pp. 1695–1697. DOI: 10.1063/1.123658.

[120] O. Weidemann et al. “Influence of thermal oxidation on the electronic properties of Pt Schottky contacts on GaN grown by molecular-beam epitaxy”. In: *Applied Physics Letters* 86.8 (2005), pp. 1–3. DOI: 10.1063/1.1868863.

[121] M. E. Lin et al. “Low resistance ohmic contacts on wide band-gap GaN”. In: *Applied Physics Letters* 64.8 (1994), pp. 1003–1005. DOI: 10.1063/1.111961.

[122] Yuji Koyama et al. “Formation processes and properties of Schottky and ohmic contacts on n-type GaN for field effect transistor applications”. In: *Solid-State Electronics* 43.8 (1999), pp. 1483–1488. DOI: 10.1016/S0038-1101(99)00093-3.

[123] V. Reddy et al. “Electrical and structural properties of low-resistance Ti/Al/Re/Au ohmic contacts to n-type GaN”. In: *Journal of Electronic Materials* 33.5 (2004), pp. 395–399. DOI: 10.1007/s11664-004-0190-y.

[124] S. Fernández et al. “Performance enhancement of ohmic contact on n-GaN using Ti-W as metal barrier”. In: *Materials Science and Engineering B: Solid-State Materials for Advanced Technology* 143.1-3 (2007), pp. 55–59. DOI: 10.1016/j.mseb.2007.07.004.

[125] S. Kurtin et al. "Fundamental transition in the electronic nature of solids". In: *Physical Review Letters* 22.26 (1969), pp. 1433–1436. DOI: 10.1103/PhysRevLett.22.1433.

[126] J. S. Foresi and T. D. Moustakas. "Metal contacts to gallium nitride". In: *Applied Physics Letters* 62.22 (1993), pp. 2859–2861. DOI: 10.1063/1.109207.

[127] Ferdinando Iucolano et al. "Barrier inhomogeneity and electrical properties of PtGaN Schottky contacts". In: *Journal of Applied Physics* 102.11 (2007), pp. 1–8. DOI: 10.1063/1.2817647.

[128] E. Monroy et al. "Thermal stability of Pt- and Ni-based Schottky contacts on GaN and Al0.31Ga0.69N". In: *Semiconductor Science and Technology* 17.9 (2002). DOI: 10.1088/0268-1242/17/9/103.

[129] M. Ravinandan et al. "Analysis of the current-voltage characteristics of the Pd/Au Schottky structure on n-type GaN in a wide temperature range". In: *Semiconductor Science and Technology* 24.3 (2009). DOI: 10.1088/0268-1242/24/3/035004.

[130] V. Rajagopal Reddy et al. "Electrical and structural properties of rapidly annealed Pd/Mo Schottky contacts on n-type GaN". In: *Semiconductor Science and Technology* 23.9 (2008). DOI: 10.1088/0268-1242/23/9/095026.

[131] V. Rajagopal Reddy and N. Ramesha Reddy. "Influence of thermal annealing temperature on electrical properties of Rh and Rh/Au Schottky contacts to n-type GaN". In: *Journal of Optoelectronics and Advanced Materials* 9.12 (2007), pp. 3871–3876.

[132] N. Miura et al. "Thermal annealing effects on Ni/Au based Schottky contacts on n-GaN and AlGaN/GaN with insertion of high work function metal". In: *Solid-State Electronics* 48.5 (2004), pp. 689–695. DOI: 10.1016/j.sse.2003.07.006.

[133] Thorsten U. Kampen and Winfried Mönch. "Barrier heights of GaN Schottky contacts". In: *Applied Surface Science* 117-118.97 (1997), pp. 388–393. DOI: 10.1016/S0169-4332(97)80112-2.

[134] E.V. Kalinina et al. "Structural and electrical properties of Schottky barriers on n-GaN". In: *Diamond and Related Materials* 6.10 (1997), pp. 1528–1531. DOI: 10.1016/S0925-9635(97)00115-5.

[135] Abhishek Motayed et al. "Two-step surface treatment technique: Realization of nonalloyed low-resistance Ti/Al/Ti/Au ohmic contact to n-GaN". In: *Journal of Vacuum Science & Technology B: Microelectronics and Nanometer Structures* 22.2 (2004), p. 663. DOI: 10.1116/1.1667506.

[136] Jong Kyu Kim et al. "Effect of surface treatment by (NH 4) 2 S x solution on the reduction of ohmic contact resistivity of p-type GaN". In: *Journal of Vacuum Science & Technology B: Microelectronics and Nanometer Structures* 17.2 (1999), p. 497. DOI: 10.1116/1.590584.

[137] R. J. Shul et al. "Comparison of plasma etch techniques for III-V nitrides". In: *Solid-State Electronics* 42.12 (1998), pp. 2259–2267. DOI: 10.1016/S0038-1101(98)00223-8.

[138] L L Smith et al. "Cleaning of GaN surfaces". In: *Journal of Electronic Materials* 25.5 (1996), pp. 805–810. DOI: 10.1007/BF02666640.

[139] S. W. King et al. "Cleaning of AlN and GaN surfaces". In: *Journal of Applied Physics* 84.9 (1998), pp. 5248–5260. DOI: 10.1063/1.368814.

[140] K N Lee et al. "Surface Chemical Treatment for the Cleaning of AlN and GaN Surfaces". In: *Journal of The Electrochemical Society* 147.8 (2000), pp. 3087–3090. DOI: 10.1149/1.1393860.

[141] M. Diale and F. D. Auret. "Effects of chemical treatment on barrier height and ideality factors of Au/GaN Schottky diodes". In: *Physica B: Condensed Matter* 404.22 (2009), pp. 4415–4418. DOI: 10.1016/j.physb.2009.09.039.

[142] G. Moldovan et al. "Effects of KOH etching on the properties of Ga-polar n-GaN surfaces". In: *Philosophical Magazine* 86.16 (2006), pp. 2315–2327. DOI: 10.1080/14786430500522628.

[143] K. A. Rickert et al. "N-GaN surface treatments for metal contacts studied via x-ray photoemission spectroscopy". In: *Applied Physics Letters* 80.2 (2002), pp. 204–206. DOI: 10.1063/1.1430024.

[144] G. Landgren et al. "The oxidation of GaAs(110): A reevaluation". In: *Journal of Vacuum Science and Technology B: Microelectronics and Nanometer Structures* 2.3 (1984), pp. 351–358. DOI: 10.1116/1.582823.

[145] J. L. Weyher et al. "Chemical polishing of bulk and epitaxial GaN". In: *Journal of Crystal Growth* 182.1-2 (1997), pp. 17–22. DOI: 10.1016/S0022-0248(97)00320-5.

[146] S. Noor Mohammad. "Contact mechanisms and design principles for Schottky contacts to group-III nitrides". In: *Journal of Applied Physics* 97.6 (2005). DOI: 10.1063/1.1856226.

[147] Jun Wang et al. "Thermal annealing behaviour of Pt on n-GaN Schottky contacts". In: *Journal of Physics D: Applied Physics* 36.8 (2003), pp. 1018–1022. DOI: 10.1088/0022-3727/36/8/312.

[148] R. H. Williams et al. "Chemical effects in Schottky barrier formation". In: *Journal of Physics C: Solid State Physics* 11.17 (1978), pp. L735–L738. DOI: 10.1088/0022-3719/11/17/006.

[149] W. E. Spicer et al. "Unified Mechanism for Schottky-Barrier Formation and III-V Oxide Interface States". In: *Physical Review Letters* 44.6 (1980), pp. 420–423. DOI: 10.1103/PhysRevLett.44.420.

[150] Yuanping Sun et al. "Thermal annealing behaviour of Ni/Au on n-GaN Schottky contacts". In: *Journal of Physics D: Applied Physics* 35.20 (2002), pp. 2648–2651. DOI: 10.1088/0022-3727/35/20/326.

[151] E. H. Rhoderick. "Metal-semiconductor contacts". In: *Physics in Technology* 5.4 (1974), p. 223. DOI: 10.1088/0305-4624/5/4/405. arXiv: arXiv:1011.1669v3.

[152] B. L. Sharma, ed. *Metal-Semiconductor Schottky Barrier Junctions and Their Applications*. Boston, MA: Springer US, 1984. DOI: 10.1007/978-1-4684-4655-5.

[153] V. Bougrov et al. "Gallium Nitride (GaN)". In: *Properties of Advanced Semiconductor Materials: GaN, AIN, InN, BN, SiC, SiGe*. John Wiley \& Sons, 2001. Chap. 1, pp. 1–30.

[154] C. R. Crowell and V. L. Rideout. "Normalized thermionic-field (T-F) emission in metal-semiconductor (Schottky) barriers". In: *Solid State Electronics* 12.2 (1969), pp. 89–105. DOI: 10.1016/0038-1101(69)90117-8.

[155] F. A. Padovani and R. Stratton. "Field and thermionic-field emission in Schottky barriers". In: *Solid State Electronics* 9.7 (1966), pp. 695–707. DOI: 10.1016/0038-1101(66)90097-9.

[156] John Bardeen. “Surface States and Rectification at a Metal Semi-Conductor Contact”. In: *Physical Review* 71.10 (1947), pp. 717–727. DOI: 10.1103/PhysRev.71.717. arXiv: arXiv:1011.1669v3.

[157] Yi Zhou et al. “Temperature-dependent electrical characteristics of bulk GaN Schottky rectifier”. In: *Journal of Applied Physics* 101.2 (2007). DOI: 10.1063/1.2425004.

[158] B. Akkal et al. “Electrical characterization of Au/n-GaN Schottky diodes”. In: *Materials Chemistry and Physics* 85.1 (2004), pp. 27–31. DOI: 10.1016/j.matchemphys.2003.11.007.

[159] E. Özavcı et al. “A detailed study on current–voltage characteristics of Au/n-GaAs in wide temperature range”. In: *Sensors and Actuators A: Physical* 194 (2013). Ed. by B. L. Sharma, pp. 259–268. DOI: 10.1016/j.sna.2013.02.018.

[160] Nezir Yldrm et al. “On temperature-dependent experimental I-V and C-V data of Ni/n-GaN Schottky contacts”. In: *Journal of Applied Physics* 108.11 (2010). DOI: 10.1063/1.3517810.

[161] K. Suzue et al. “Electrical conduction in platinum-gallium nitride Schottky diodes”. In: *Journal of Applied Physics* 80.8 (1996), pp. 4467–4478. DOI: 10.1063/1.363408.

[162] E. Özavci et al. “A detailed study on current-voltage characteristics of Au/n-GaAs in wide temperature range”. In: *Sensors and Actuators, A: Physical* 194 (2013), pp. 259–268. DOI: 10.1016/j.sna.2013.02.018.

[163] H. Norde. “A modified forward I-V plot for Schottky diodes with high series resistance”. In: *Journal of Applied Physics* 50.7 (1979), pp. 5052–5053. DOI: 10.1063/1.325607.

[164] A. B. McLean. “Limitations to the Norde I-V plot”. In: *Semiconductor Science and Technology* 1.3 (1986), pp. 177–179. DOI: 10.1088/0268-1242/1/3/003.

[165] Roberto M. Cibils and Román H. Buitrago. “Forward I-V plot for nonideal Schottky diodes with high series resistance”. In: *Journal of Applied Physics* 58.2 (1985), pp. 1075–1077. DOI: 10.1063/1.336222.

[166] K Sato and Y Yasumura. “Study of forward I - V plot for Schottky diodes with high series resistance”. In: *Journal of Applied Physics* 58.9 (1985), pp. 3655–3657. DOI: 10.1063/1.335750.

[167] C. D. Lien et al. “An Improved Forward I-V Method For Nonideal Schottky Diodes With High Series Resistance”. In: *IEEE Transactions on Electron Devices* 31.10 (1984), pp. 1502–1503. DOI: 10.1109/T-ED.1984.21739.

[168] K E Bohlin. “Generalized Norde plot including determination of the ideality factor”. In: *Journal of Applied Physics* 60.3 (1986), pp. 1223–1224. DOI: 10.1063/1.337372.

[169] Tran Chot. “A modified forward I-U plot for schottky diodes with high series resistance”. In: *Physica Status Solidi (a)* 66.1 (1981), K43–K45. DOI: 10.1002/pssa.2210660159.

[170] S. K. Cheung and N. W. Cheung. “Extraction of Schottky diode parameters from forward current-voltage characteristics”. In: *Applied Physics Letters* 49.2 (1986), pp. 85–87. DOI: 10.1063/1.97359.

[171] Jürgen H. Werner. “Schottky barrier and pn-junction I/V plots - Small signal evaluation”. In: *Applied Physics A Solids and Surfaces* 47.3 (1988), pp. 291–300. DOI: 10.1007/BF00615935.

[172] A. Kaminski et al. "I-V methods to extract junction parameters with special emphasis on low series resistance". In: *Solid-State Electronics* 43.4 (1999), pp. 741–745. DOI: 10.1016/S0038-1101(98)00338-4.

[173] T. C. Lee et al. "A systematic approach to the measurement of ideality factor, series resistance, and barrier height for Schottky diodes". In: *Journal of Applied Physics* 72.10 (1992), pp. 4739–4742. DOI: 10.1063/1.352082.

[174] D. Gromov and V. Pugachevich. "Modified methods for the calculation of real Schottky-diode parameters". In: *Applied Physics A Solids and Surfaces* 59.3 (1994), pp. 331–333. DOI: 10.1007/BF00348239.

[175] W. Jung and M. Guziewicz. "Schottky diode parameters extraction using Lambert W function". In: *Materials Science and Engineering B: Solid-State Materials for Advanced Technology* 165.1-2 (2009), pp. 57–59. DOI: 10.1016/j.mseb.2009.02.013.

[176] Kaier Wang and Meiying Ye. "Parameter determination of Schottky-barrier diode model using differential evolution". In: *Solid-State Electronics* 53.2 (2009), pp. 234–240. DOI: 10.1016/j.sse.2008.11.010.

[177] Meiying Ye et al. "Parameter extraction of solar cells using particle swarm optimization". In: *Journal of Applied Physics* 105.9 (2009), pp. 1–8. DOI: 10.1063/1.3122082.

[178] Yow Jon Lin. "Origins of the temperature dependence of the series resistance, ideality factor and barrier height based on the thermionic emission model for n-type GaN Schottky diodes". In: *Thin Solid Films* 519.2 (2010), pp. 829–832. DOI: 10.1016/j.tsf.2010.08.103.

[179] P. Hacke et al. "Schottky barrier on n-type GaN grown by hydride vapor phase epitaxy". In: *Applied Physics Letters* 63.19 (1993), pp. 2676–2678. DOI: 10.1063/1.110417. arXiv: arXiv:0711.1034v1.

[180] A. R. Arehart et al. "Effect of threading dislocation density on Ni/n-GaN Schottky diode I-V characteristics". In: *Journal of Applied Physics* 100.2 (2006). DOI: 10.1063/1.2219985.

[181] Hiroyasu Ishikawa et al. "Pd/GaN Schottky diode with a barrier height of 1.5 eV and a reasonably effective Richardson coefficient". In: *Japanese Journal of Applied Physics, Part 2: Letters* 37.1 PART A/B (1998), pp. 1–4. DOI: 10.1143/jjap.37.l7.

[182] C. R. Crowell and S. M. Sze. "Current transport in metal-semiconductor barriers". In: *Solid State Electronics* 9.11-12 (1966), pp. 1035–1048. DOI: 10.1016/0038-1101(66)90127-4.

[183] M. C.A.M. Koolen et al. "An improved de-embedding technique for on-wafer high-frequency characterization". In: *Proceedings of the 1991 Bipolar Circuits and Technology Meeting* (1992), pp. 188–191. DOI: 10.1109/bipol.1991.160985.

[184] Aik Yean Tang et al. "Analytical extraction of a schottky diode model from broadband S-parameters". In: *IEEE Transactions on Microwave Theory and Techniques* 61.5 (2013), pp. 1870–1878. DOI: 10.1109/TMTT.2013.2251655.

[185] V. Aubry and F. Meyer. "Schottky diodes with high series resistance: Limitations of forward I-V methods". In: *Journal of Applied Physics* 76.12 (1994), pp. 7973–7984. DOI: 10.1063/1.357909.

[186] S.N. Mohammad et al. "Near-ideal platinum-GaN Schottky diodes". In: *Electronics Letters* 32.6 (1996), p. 598. DOI: 10.1049/el:19960354.

[187] Mustapha Amine Kadaoui et al. "Electrical parameters of Au/n-GaN and Pt/n-GaN Schottky diodes". In: *Superlattices and Microstructures* 82 (2015), pp. 269–286. DOI: 10.1016/j.spmi.2015.02.007.

[188] Ferdinando Iucolano et al. "Temperature behavior of inhomogeneous Pt/GaN Schottky contacts". In: *Applied Physics Letters* 90.9 (2007), pp. 1–4. DOI: 10.1063/1.2710770.

[189] A. Krost and A. Dadgar. "GaN-based devices on Si". In: *Physica Status Solidi (A) Applied Research* 194.2 SPEC. (2002), pp. 361–375. DOI: 10.1002/1521-396X(200212)194:2<361::AID-PSSA361>3.0.CO;2-R.

[190] F. A. Padovani and G. G. Sumner. "Experimental study of gold-gallium arsenide Schottky barriers". In: *Journal of Applied Physics* 36.12 (1965), pp. 3744–3747. DOI: 10.1063/1.1713940.

[191] A. C. Schmitz et al. "Metal contacts to n-type GaN". In: *Journal of Electronic Materials* 27.4 (1998), pp. 255–260. DOI: 10.1007/s11664-998-0396-5.

[192] Ashish Kumar et al. "Micro-structural and temperature dependent electrical characterization of Ni/GaN Schottky barrier diodes". In: *Current Applied Physics* 13.6 (2013), pp. 1137–1142. DOI: 10.1016/j.cap.2013.03.009.

[193] Mohammad Rezaul Huque Khan et al. "The barrier height and interface effect of a au-n-gan schottky diode". In: *Journal of Physics D: Applied Physics* 28.6 (1995), pp. 1169–1174. DOI: 10.1088/0022-3727/28/6/021.

[194] A.S. Bhuiyan et al. "A new Richardson plot for non-ideal schottky diodes". In: *Thin Solid Films* 161 (1988), pp. 93–100. DOI: 10.1016/0040-6090(88)90239-8.

[195] L. S. Yu et al. "The role of the tunneling component in the current–voltage characteristics of metal-GaN Schottky diodes". In: *Journal of Applied Physics* 84.4 (1998), pp. 2099–2104. DOI: 10.1063/1.368270.

[196] Paul S. Ho et al. "Electronic states at silicide-silicon interfaces". In: *Physical Review Letters* 56.2 (1986), pp. 177–180. DOI: 10.1103/PhysRevLett.56.177.

[197] Y. Kribes et al. "Investigation of Au Schottky contacts on GaN grown by molecular beam epitaxy". In: *Semiconductor Science and Technology* 12.7 (1997), pp. 913–916. DOI: 10.1088/0268-1242/12/7/024.

[198] J. D. Guo et al. "Schottky contact and the thermal stability of Ni on n-type GaN". In: *Journal of Applied Physics* 80.3 (1996), pp. 1623–1627. DOI: 10.1063/1.363822.

[199] L. F. Wagner et al. "A Note on the Correlation Between the Schottky-Diode Barrier Height and the Ideality Factor as Determined from I-V Measurements". In: *IEEE Electron Device Letters* 4.9 (1983), pp. 320–322. DOI: 10.1109/EDL.1983.25748.

[200] Koteswara Rao Peta et al. "Analysis of electrical properties and deep level defects in undoped GaN Schottky barrier diode". In: *Thin Solid Films* 534 (2013), pp. 603–608. DOI: 10.1016/j.tsf.2013.01.100.

[201] Koteswara Rao Peta and Moon Deock Kim. "Leakage current transport mechanism under reverse bias in Au/Ni/GaN Schottky barrier diode". In: *Superlattices and Microstructures* 113 (2018), pp. 678–683. DOI: 10.1016/j.spmi.2017.11.056.

[202] F. J. Bryant et al. "The interpretation of non-linear Schottky barrier C-2-V characteristics". In: *Solid State Communications* 63.1 (1987), pp. 9–12. DOI: 10.1016/0038-1098(87)90055-X.

[203] Alvin M. Goodman. "Metal - Semiconductor Barrier Height Measurement by the Differential Capacitance Method - One Carrier System". In: *Journal of Applied Physics* 34.2 (1963), pp. 329–338. DOI: 10.1063/1.1702608.

[204] Prahalad K. Vasudev et al. "Excess capacitance and non-ideal Schottky barriers on GaAs". In: *Solid State Electronics* 19.7 (1976), pp. 557–559. DOI: 10.1016/0038-1101(76)90052-6.

[205] Lisen Zhang et al. "High-power 300 GHz Solid-state Source Chain Based on GaN Doublers". In: *IEEE Electron Device Letters* 3106.c (2021), pp. 1–1. DOI: 10.1109/LED.2021.3110781.

List of Figures

1.1 The electromagnetic spectrum 1
1.2 Spectrum of the Milky Way 2
1.3 Spectra of important molecules 4
1.4 Atmospheric attenuation of THz radiation 5
1.5 THz scan of concealed weapons 7
1.6 THz Sources vs Frequency 9
1.7 QCL Band diagram 10
1.8 Frequency multiplier 11
1.9 Crystal lattice of wurtzite GaN 15
1.10 Wurtzite GaN band structure 17

2.1 Epitaxies employed 24
2.2 Process flow 25
2.3 NLOF development results 26
2.4 SEM pictures of RIE results 26
2.5 n^{-} GaN mesa 27
2.6 Ti/Al/Ni/Au Ohmic contact 29
2.7 TLM pattern structure 30
2.8 Circular TLM pattern structure 30
2.9 Results of circular TLM measurements 31
2.10 Schottky contact 33
2.11 Schottky diode mesa 34
2.12 SEM pictures of ICP dry etching for isolation 35
2.13 Resist reflow 36
2.14 SEM images of Schottky diodes after the development of the final lithographic step 36
2.15 Profile SEM pictures of Schottky diodes with air-bridge 37
2.16 Top view SEM pictures of Schottky diodes with air-bridge 38
2.17 Over-development of the reflow resist on GaN on Si process 39
2.18 Technological problems encountered during the fabrication of Schottky diodes on GaN on SiC 40
2.19 XPS survey spectra for GaN on SiC samples 43
2.20 XPS survey spectra for Ga, N and other lines for GaN on SiC samples 44
2.21 AFM images from randomly selected 5 µm×5 µm areas of GaN on SiC samples for each of the surface treatments performed 45
2.22 AFM images from randomly selected 5 µm×5 µm areas of Schottky contacts on GaN on SiC 48
2.23 3D AFM images from randomly selected 5 µm×5 µm areas of Schottky contacts on GaN on SiC 49

3.1 Schematic band diagram before contact . . . 51
3.2 Schematic band diagram after contact . . . 52
3.3 DC characteristics . . . 57
3.4 Theoretical nk_BT vs k_BT plot . . . 60
3.5 TE fit of forward characteristic . . . 61
3.6 Series resistance of the 70 µm diode . . . 62
3.7 Norde's auxiliary function . . . 63
3.8 First Cheung function . . . 65
3.9 Second Cheung function . . . 66
3.10 DC-T characteristics . . . 67
3.11 ϕ_B and n at different temperatures . . . 68
3.12 Richardson plot . . . 69
3.13 Plot of of C^{-2} vs V . . . 70
3.14 Schottky diode equivalent circuit . . . 71
3.15 Capacitance measurements obtained from S-parameters . . . 72
3.16 Junction capacitance . . . 73
3.17 Typical DC characteristics . . . 76
3.18 Forward I-V-T characteristics . . . 81
3.19 Schottky diode parameters for temperatures between 77–375 K . . . 81
3.20 Richardson plot . . . 83
3.21 Current normalization . . . 87
3.22 Breakdown voltage . . . 88
3.23 C^{-2} vs V plot . . . 89
3.24 C^{-2} vs V curves measured on a GaN on SiC Schottky diode with diameter of 70 µm for the different surface treatments . . . 90
3.25 C^{-2} vs V curve measured on a GaN on Si Schottky diode with diamater of 44.28 µm . . . 91
3.26 Total capacitance as extracted from de-embedded S-parameter measurements . . . 92
3.27 Junction capacitance for the 6 µm KOH-treated GaN on SiC diode . . . 93
3.28 Cutoff frequency versus voltage for selected quasi-vertical GaN on SiC diodes . . . 96

List of Tables

1.1 Bulk GaN properties 16
1.2 Properties common semiconductors 19

2.1 TLM results of Fig. 2.9 31
2.2 Specific contact resistance of Ohmic contacts on n-GaN 31
2.3 Schottky barrier height on n-GaN 32
2.4 Quantitative analysis of elemental intensities 44
2.5 Root mean squared (rms) surface roughness (in nm) calculated from the AFM scans on all samples) 46

3.1 Schottky diode parameters 76
3.2 Schottky diode extracted parameters with Cheung's method 77
3.3 Schottky diode parameters for different surface treatment before annealing 79
3.4 Schottky diode parameters for different surface treatment after annealing 79
3.5 Parameters for the 70 µm diode for temperatures between 77–375 K . 82
3.6 Effective Richardson constant and barrier height for the measured diodes 84
3.7 Breakdown voltage of GaN on sapphire Schottky diodes 85
3.8 Breakdown voltage of GaN on Si and GaN on SiC 86
3.9 Schottky diode parameters extracted from CV measurements 89
3.10 Extracted parameters from high-frequency characterization for selected GaN on SiC Schottky diodes 94
3.11 Calculated cutoff frequency for selected GaN on SiC Schottky diodes 95
3.12 Parameters of selected quasi-vertical GaN on SiC diodes with high breakdown voltage @1 µA 95

List of Symbols

ϕ_M	Metal workfunction
ϕ_S	Semiconductor workfunction
E_0	Vacuum level
E_C	Conduction Band level
χ_S	Semiconductor electron affinity
E_V	Valence Band level
V_{bi}	Built-in potential
ϕ_B	Schottky barrier height
I_{SM}	Semiconductor-to-Metal Current
I_{MS}	Metal-to-Semiconductor Current
I_{sat}	Saturation Current
V_T	Thermal Voltage
k_B	Boltzmann's Constant
q	Elementary charge
I_{th}	Thermionic Emission Current
A^*	Richardson constant
h	Planck's Constant
m_0	Rest electron mass in vacuum
m_n^*	Electron effective mass
I_{tun}	Tunneling Current
E_0	Tunneling Probability
E_{00}	Tunneling Parameter
I_{tun0}	Tunneling Saturation Current
I_{gr}	Generation-Recombination Current

w_d	Depletion region width
τ_0	Carrier lifetime in the depletion region
n	Ideality factor
ε_S	Semiconductor dielectric constant
N_d	Doping denisty
ξ_{max}	Maximum electric field
ϕ_B^{ZB}	Zero-bias barrier height
δ	Insulator layer thickness
D_S	Density of interface states
ε_i	Insulator layer dielectric constant
R_S	Series resistance
A^{**}	Effective Richardson constant
A	Schottky contact area
ε_0	Dielectric vacuum constant
V_x	Intercept on the x-axis in a C^{-2} vs V plot
N_c	Density of states in the conduction band edge
ϕ_B^{FB}	Flat-band barrier height
Y_{open}	Y-parameters of the open circuit structure
Y_{short}	Y-parameters of the short circuit structure
Y_{DUT}	As-measured Y-parameters of the DUT
$Y_{DUT}^{de-embedded}$	De-embedded Y-parameters of the DUT
C_j	Diode junction capacitance
C_{par}	Diode parasitic capacitance
C_{j0}	Zero-bias junction capacitance
C_{fp}	Finger-to-pad capacitance
C_{pp}	Pad-to-pad capacitance
R_{tot}	Total diode resistance
R_j	Junction resistance
n_i	Semiconductor intrinsic carrier concentration
N_v	Density of states in the valence band edge
E_g	Semiconductor bandgap

f_c Cutoff frequency

Publications

Journal articles

[I] G. Di Gioia, M. Samnouni, V. Chinni, P. Mondal, J. Treuttell, M. Zegaoui, G. Ducournau, M. Zaknoune, Y. Roelens, *"GaN Schottky diode on sapphire substrate for THz frequency multiplier applications"*, Superlattices and Microstructures, `https://doi.org/10.1016/j.spmi.2021.107116`.

Conference proceedings

[II] G. Di Gioia, V. Chinni, M. Zegaoui, Y. Cordier, A. Maestrini, J.Treuttel, G. Ducournau, Y. Roelens, M. Zaknoune, *"GaN Schottky diode for high power THz generation using multiplier principle"*, 43rd Workshop on Compound Semiconductor Devices and Integrated Circuits, WOCSDICE 2019, Cabourg, France, 2019. **Full text**

[III] G. Di Gioia, M. Samnouni, H. Bouillaud, P. Mondal, J. Treutell, Y. Cordier, M. Zegaoui, G. Ducournau, Y. Roelens, M. Zaknoune, *"GaN Schottky diode on Silicon substrate for high power THz multiplier"*, 44th Workshop on Compound Semiconductor Devices and Integrated Circuits, WOCSDICE 2021, Bristol, UK, 2021. **Full text**

[IV] B. Orfao, B.G. Vasallo, D. Moro-Melgar, M. Zaknoune, G. Di Gioia, M. Samnouni, S. Pérez, T. González, J. Mateos, *"Technological Parameters and Edge Fringing Capacitance in GaN Schottky Barrier Diodes: Monte Carlo Simulations"*, 2021 13th Spanish Conference on Electron Devices (CDE). IEEE, 2021.

[V] H. Bouillaud, P. Mondal, G. Di Gioia, M. Samnouni, M. Zegaoui, G. Ducournau, Y. Roelens, J. Treuttel, M. Zaknoune, *"GaAs Schottky Diodes Development for Millimiter Wave Doubler"*, 44rd Workshop on Compound Semiconductor Devices and Integrated Circuits, WOCSDICE 2021, Bristol, UK, 2021.

Useful links